TWO-DIMENSIONAL MATERIALS-BASED PHOTOVOLTAICS

FOR HIGH SPECIFIC POWER APPLICATIONS

AN ABSTRACT

SUBMITTED ON THE 5th DAY OF MAY 2024

TO THE DEPARTMENT OF PHYSICS & ENGINEERING PHYSICS

IN PARTIAL FULFILLMENT OF THE REQUIREMENTS

OF THE SCHOOL OF SCIENCE AND ENGINEERING

OF TULANE UNIVERSITY

FOR THE DEGREE

OF

DOCTOR OF PHILOSOPHY

BY

Timothy Ismael

TIMOTHY ISMAEL

APPROVED:

Matthew D. Escarra, Ph.D.
Director

Michael Naguib
Digitally signed by Michael Naguib
DN: cn=Michael Naguib, o, ou, email=naguib@tulane.edu, c=US
Date: 2024.05.02 12:20:59 -05'00'

Michael Naguib, Ph.D.

Pedro Derosa

Pedro Derosa, Ph.D.

# ABSTRACT

The interest in two-dimensional (2D) material research has increased over the years due to their exceptional mechanical, optical, and electrical properties, with a wide range of applications from nano-electronics to corrosion resistance coatings. More applicable to this work, some 2D materials such as molybdenum disulfide ($MoS_2$), display strong light-matter interactions, highlighting their suitability for applications in optoelectronics and photovoltaics. Device concepts using exfoliated $MoS_2$ have been shown at micron-scale; however, high quality large area films at wafer (>$cm^2$) scale are required to produce next generation devices like flexible, wearable, and ultrathin electronics and photovoltaics. We report on the development of the chemical vapor deposition (CVD) process for wafer scale $MoS_2$ growth, focused on maximizing flake dimensions and film uniformity and the development of a single station setup for correlative spatial mapping of film properties at sub-micron resolution. High-quality $MoS_2$ films are then used to produce high-specific power 2D photovoltaics, which is a promising alternative to conventional solar power conversion systems in space and other flexible, high-specific power applications. Furthermore, the advantage of vertical carrier transport over lateral transport in the device architecture for 2D photovoltaics is presented. This work adds to ongoing efforts focused on improving ultrathin 2D material-based optoelectronics and photovoltaic device efficiency, by synthesis development, contact engineering, and new device architectures. The synthesis and engineering decisions are informed by multiplexed spatial mapping of device properties; device modelling based on the physics of Schottky photovoltaics, optical properties, and work function measurements; innovations in 2D materials-based device

fabrication; and advanced analysis of these devices for their implementation in space. The work aims to contribute to the realization of high efficiency, high specific power, 2D materials-based ultrathin photovoltaics.

# TWO-DIMENSIONAL MATERIALS-BASED PHOTOVOLTAICS FOR HIGH SPECIFIC POWER APPLICATIONS

A DISSERTATION

SUBMITTED ON THE 5th DAY OF MAY 2024

TO THE DEPARTMENT OF PHYSICS & ENGINEERING PHYSICS

IN PARTIAL FULFILLMENT OF THE REQUIREMENTS

OF THE SCHOOL OF SCIENCE AND ENGINEERING

OF TULANE UNIVERSITY

FOR THE DEGREE

OF

DOCTOR OF PHILOSOPHY

BY

Timothy Ismael

TIMOTHY ISMAEL

APPROVED:

Matthew D. Escarra, Ph.D.
Director

Michael Naguib
Digitally signed by Michael Naguib
DN: cn=Michael Naguib, o, ou, email=naguib@tulane.edu, c=US
Date: 2024.05.02 12:22:11 -05'00'

Michael Naguib, Ph.D.

Pedro Derosa

Pedro Derosa, Ph.D.

# ACKNOWLEDGMENTS

Firstly, many thanks to my family for all your support. I am grateful to my mom and dad for their full support throughout my academic career. Special thanks to Carla for all the support and encouragement you gave me over the duration of this work. Thanks to Rhonda and Andrez for your availability to discuss ideas and to provide both distractions and clarity when needed.

Prof. Matthew D. Escarra, thanks for your motivation and commitment to ensuring that I develop into a well-rounded researcher. Your approach has helped me to become vastly more knowledgeable in the field and for this I am grateful. Thanks Prof. Pedro Derosa for your support, from the introduction to research in Physics at Grambling State University and graduate student at Louisiana Tech to being on my PhD committee. Prof. Michael Naguib, for being on my committee and providing direction and inspiration that kept me going throughout this work.

Dr. Michael Johnson and Dr Daniel Kuncicky for hours of training, maintaining, and troubleshooting synthesis, fabrication and characterization tools and assisting with process optimizations. Dr. Jibao He, for help with TEM measurements, Dr. John Robertson, Dr. Adam Ollanik, Dr. Yaping Ji, Dr. Kazi Islam, Dr. Isaac Oguntoye, Siddharth Padmanabha, Aamir Abbas, Afeez Akanni Lukmon, Nathan Grinalds, Claire Luthy, Meghan Bush, Jeremiah McNatt, Thalia Koutsougeras, Owen Harris, George Ingrish, Josh Sasson for supporting, encouraging, and help in many aspects.

Dr. Abin Joshy, Dr. Anika Tabbasum, Dr. Kaitlyn Prenger, Prof. Kun Liang for many hours spent setting up and troubleshooting equipment.

Finally, many thanks to everyone who has cheered me on along this journey.

# TABLE OF CONTENTS

# LIST OF FIGURES

# LIST OF TABLES

# CHAPTER 1

# INTRODUCTION

With the steady expansion of industries, energy requirements continue to increase globally. At the same time, electronic devices are becoming more widely and frequently used daily. In parallel with power consumption and power conversion efficiency of these devices, features such as comfort, weight and wearability are being considered more closely in the development of modern electronics. Applications like space missions are becoming more and more complex, requiring highly optimized, application specific energy solutions to power essential systems.

To date, non-renewable resources are still being used to meet energy demands so it is therefore important to be mindful of the accompanying environmental impact. $CO_2$ emissions play a significant role in increasing global-warming, [1], [2] and has been identified as a key factor contributing to the frequency of natural disasters such as floods and tropical cyclones worldwide. [1], [3], [4] In recent years, there have been extensive urbanization in coastal areas, and as a result, more and more human lives are being impacted by flood disasters exacerbated by climate change. [5] For example, Louisiana has been experiencing more frequent tropical cyclone inflicted disasters, with hurricanes Laura and Zeta in 2020 and Ida in 2021 causing considerable damage to infrastructure. Coastal regions continue to be on the frontline of frequent assault by storms, highlighting the importance of improving renewable energy systems. As a result, the use of renewable energy resources to satisfy the energy demand is becoming more desirable.

Several energy conversion approaches utilizing renewable energy sources are continuously being developed to overcome these challenges. One of the most feasible solutions is the conversion of solar energy to electrical energy or photovoltaics. Photovoltaics not only aim to reduce the global average $CO_2$ emissions, [6] but is an ideal energy conversion option not just for wearable modern electronics, but also for space applications. With solar cells supplying most of the energy required by a spacecraft throughout its mission, there has been a growing demand for space photovoltaics optimized for the more sophisticated space missions. [7] The implementation, however, comes with its own share of challenges. Among these challenges, achieving a high-power conversion efficiency (PCE), radiation resistance and high specific power are on top of the list. William Shockley and Hans-Joachim Queisser's detailed balance analysis showed that for a single junction solar cell, the PCE limit is 33.7% for a 1.34eV bandgap semiconductor. This fundamental limit is known as the Shockley-Queisser (S-Q) limit, [8] and over the years, the development of solar cells has led to several meaningful achievements in the attempt to approach the S-Q limit, starting from the optimization of single junction silicon solar cells to multi-junction III-V semiconductor solar cells.

High crystal quality, lattice matching, and bandgap selection has played a major role in the success of solar cell designs. The record multi-junction solar cell to date is a III-V Quadruple Junction concentrated photovoltaic cell that achieved 47.6% solar power conversion efficiency, [9] beating the previous 41.1% under direct spectrum, 143 Suns and 39.2% 1-Sun global efficiency from a monolithic, series-connected, six-junction inverted metamorphic solar cell. [10] Si solar cells are currently the main power supplier in spacecrafts, due to their high efficiency and radiation resistance. While the efficiencies

continue to improve, the drive to reduce the payload for space launch and future missions seeks a reduction in the size of the photovoltaic systems. This mass reduction of the commonly used semiconductors, however, is accompanied by loss of PCE and a decrease in radiation resistance, opening the door for further development of existing materials and the discovery and utilization of new materials in photovoltaics.

2D Transition metal dichalcogenides (TMDCs), such as $WS_2$, $WSe_2$ and $MoS_2$ are ultrathin, lightweight, flexible, and possess a high light absorption to thickness ratio. These 2D semiconductors are useful for photovoltaics applications and can serve as an essential building block not just for modern day wearable electronics but are also ideal for high specific power flexible photovoltaics.

## 1.1 Motivation

TMDCs are becoming an increasingly important material in the nano-material space and a preferred choice for the fabrication of numerous components due to their excellent mechanical strength, radiation hardness, and optical and electronic properties, and these properties vary depending on the TMDC. Researchers have mostly focused on fabricating micron scale devices using mechanically exfoliated TMDCs but this is not a scalable approach. 2D TMDC synthesis techniques such as chemical vapor deposition aim to solve the scalability problem; however, several challenges are faced by the research community in this endeavor. This includes challenges in improving the quality of the synthesized 2D materials and the reproducibility of large area uniform films during synthesis. Large area high quality film synthesis is an area of high interest especially in the production of optoelectronic devices and photovoltaics. A better understanding and optimization of the chemical vapor deposition process for $MoS_2$ synthesis and the use of the powerful characterization approach by the correlative mapping of the optical and electronic properties of the films can lead to the improvement of material quality and device performance. The fabrication of mm scale devices can highlight the scalability of 2D materials for various applications. Furthermore, the design and fabrication of large area 2D TMDC photovoltaics can provide options for high specific power ultralight flexible photovoltaics for future space missions.

## 1.2 Background of 2D Materials

The most known 2D material today is graphene. Some of its properties were recorded as early as 1859, where the atomic weight and structure was discussed [11], to the late 1990s where an etch process for applications in graphene origami was explored. [12] It was the recent isolation in 2004 and exploration of some of the electronic properties of graphene, [13] that caught the attention of a number of researchers, leading to the exploration of a large number of new 2D material candidates such as TMDCs and transition metal carbides (MXenes). [14], [15] One of the more recent additions to the family of 2D materials is 2D transition metal carbo-chalcogenides (TMCCs), which is a combination of MXenes and TMDCs. [16]These materials display a wide range of properties, some of which are discussed later in this section. Some candidates are shown in **Figure 1.1**. Like every new material, 2D materials opens up a window of possibilities within the materials space and shows promise for interesting and unconventional applications. The ultrathin form factor makes them suitable for applications in nano-electronics. [17] Furthermore, the properties of 2D materials are often different from their bulk counterparts opening a new dimension for applications and exploration of novel physics, like valleytronics [18] in twisted bilayer 2D materials. [19] Additionally, 2D materials layers are held together by weak van der Waals (vdW) bonds. This is particularly important in engineering structures for various applications where the number of 2D material layers are directly related to the device performance. In this work, we focus on the semiconducting class of 2D materials for optoelectronics and photovoltaics applications.

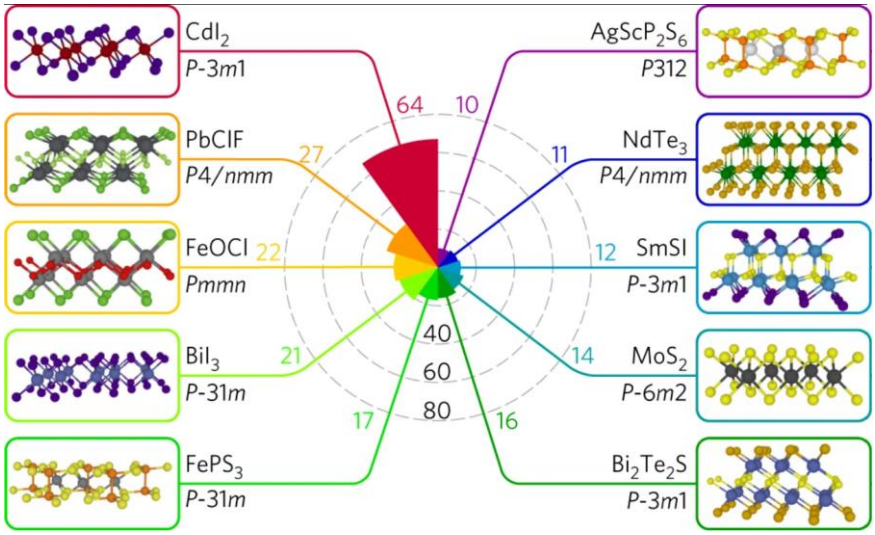


**Figure 1.1:** A representation of ten common 2D structures, with the structure-type formula and space group of the 2D systems, and the number of candidates with similar structure in a set of 1,036 2D materials. Adapted from N. Mounet et al., *Nat. Nanotechnology* (2018).

### 1.2.1 Definition

2D materials fall under the classification of nanomaterials. They are defined by their ability to exist in stable form as a single-atomic (or molecular) layer material. Only one dimension of the material is nano-sized; thus they resemble a large, but ultrathin sheet of material.

## 1.3 Properties and Characterization of 2D Materials

The properties of 2D materials are dependent on the atomic composition, which defines the microstructure, electronic structure, and other intrinsic characteristics of the material. The following sections briefly discuss some of these properties that are relevant for photovoltaic and optoelectronic applications, particularly in the family of TMDCs of formula $MX_2$, where M = transition metal, X = S, Se, Te. They are all stable in the 2H-

$MX_2$ structure at room temperature and have varying monolayer bandgaps and intrinsic doping shown in **Table 1.1**. A more interesting trait of these materials is their transition from indirect to direct bandgap transition from bulk to monolayer (~0.6-0.7 nm). This is an important property that motivates the scope of this work, and is discussed in more detail in the electronic structure section.

**Table 1.1:** Direct bandgap and intrinsic doping at room temperature of monolayer transition metal dichalcogenides. [20]–[27]

| Transition Metal Dichalcogenide | Bandgap (Eg) | Intrinsic Doping |
|---|---|---|
| **$MoS_2$** | 1.87 | n-type |
| **$MoSe_2$** | 1.62 | Ambipolar |
| **$MoTe_2$** | 1.25 | Ambipolar |
| **$WS_2$** | 1.98 | Ambipolar |
| **$WSe_2$** | 1.68 | Ambipolar |
| **$WTe_2$** | 1.24 | n-type |

TMDCs not only possess interesting electronic properties, but they also exhibit interesting layer dependent optical properties that make them suitable for light harvesting applications. In this section, we introduce all the properties relevant to the scope of the work and they are discussed in more details in the respective chapters, however, this sections may not necessarily give a holistic description of all the properties of TMDCs; more comprehensive discussions are covered by several reviews on 2D materials. [28]–[31]

### 1.3.1 Structural Properties

2D materials can be single-layer and few-layer. The few layers can be separated into stable single layers. These crystal atomic structures are single-atom-thick layers like Graphene and Hexagonal boron nitride (h-BN) or polyhedral-thick layers of atoms like $MoS_2$, that are covalently bonded in plane and within each layer, whereas the layers are held together by weak van der Waals bonds out of plane. Thus, they are also known as van der Waals solids. One of the most well-studied families of van der Waals solids is the transition metal dichalcogenides. In TMDCs, the hexagonally packed $MX_6$ octahedra or trigonal prisms share edges with six nearest neighbors within each layer, [32] and are shown in **Figure 1.2**. The 2D structure consists of three atomic layers, in which the center atomic layer is the transition metal (M), sandwiched between two chalcogen atomic layers (X), forming a hexagonally packed structure, that resembles graphite as seen in **Figure 1.2**. The common phases of TMDCs are 1T (trigonal), 2H (hexagonal) and 3R (rhombohedral). [33] In this work, large area 2H phase $MoS_2$ is synthesized and used for material characterization and device development.

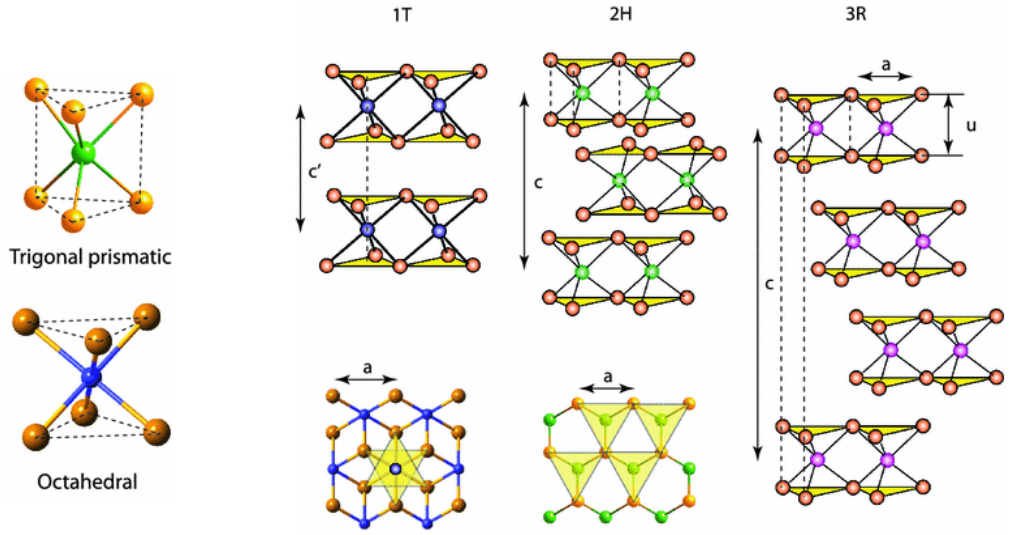


**Figure 1.2:** Leftmost figures are trigonal prismatic (top) and octahedral (bottom). Layered TMDC structures from left to right 1T (tetragonal symmetry), 2H (hexagonal symmetry) and 3R (rhombohedral symmetry). The top view of 1T and 2H phase show hexagonal structures. Adapted From A. Kolobov et al., *Springer International* (2016).

The Td (distorted octahedral) phase is not as common. Each phase has characteristic optical phonon modes and are often characterized using Raman or IR spectroscopy. Raman spectroscopy is a key technique used for characterizing the crystal structure of $MoS_2$ films synthesized in this work.

### 1.3.2 Electronic Structure

The electronic structure of 2D solids has been an ongoing research topic. One of the most prominent known traits of TMDCs is the weak interlayer bonding by electrostatic interaction between layers of ~13–21 meV/Å$^2$. [34] This allows individual layers to be easily exfoliated. The electronic properties of TMDCs mostly depend on the filling of the

outer d-orbitals. The material is a metal when these orbitals are partially filled and a semiconductor when they are full.

One of the most interesting property of some semiconducting TMDCs like $MoS_2$ 2H phase, is the indirect to direct bandgap transition when the thickness of the material decreases from bulk a monolayer [35], [36] shown in **Figure 1.3**.

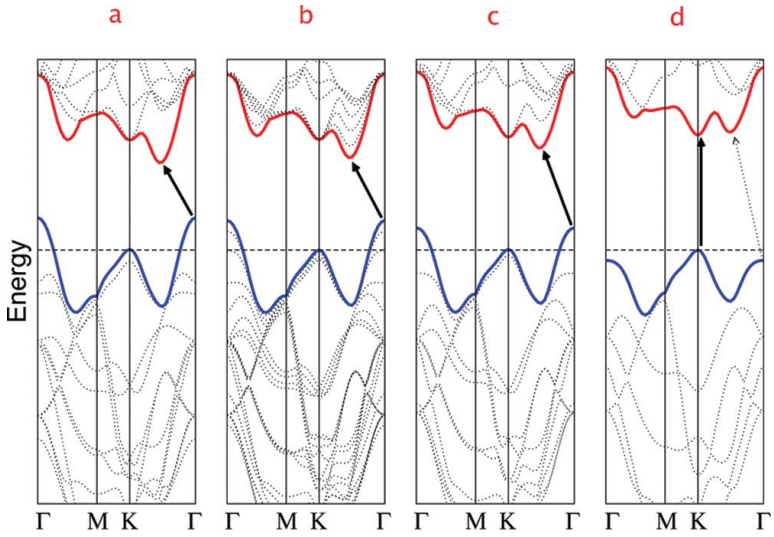


**Figure 1.3:** Calculated band structures of (a) bulk, (b) quadrilayer, (c) bilayer, and (d) monolayer $MoS_2$. The band structure shows a direct bandgap for monolayer $MoS_2$. Adapted from A. Splendiani et al*., Nano Lett.* (2010)**.**

The increase in bandgap occurs because of quantum confinement. Additionally, decreasing layers and layer spacing result in the lowering of antibonding energy thus increasing the bandgap and changing it from an indirect to direct bandgap. [35] This direct bandgap explains the superior light-matter interaction in these materials and is commonly observed experimentally in photoluminescence intensity and peak position. The superior light harvesting capability motivates the use of $TMDC_s$ in optoelectronics and photovoltaics applications, and the strong photoluminescence is ideal for the electronic property investigations discussed in the subsequent chapters.

### 1.3.3 Optical Properties

The optical properties of TMDCs make them useful for light harvesting especially in monolayer form where there is a direct bandgap as shown by the high k values at a monolayer (~0.6-0.7 nm) thickness. Additionally, in $MoS_2$, $MoSe_2$, $WS_2$, and $WSe_2$ thin films, the refractive indices (n) increase with increasing wavelength in the spectral range from 193–550 nm and decrease with wavelength until 1700 nm as shown in **Figure 1.4**. Several excitons are observed below 800 nm then the refractive indices approaches a constant value of 3.5–4.1 in the near-infrared range. [37] The high refractive index at the excitons has potential in applications, such as antireflection coatings, waveguides, and integrated photonics.

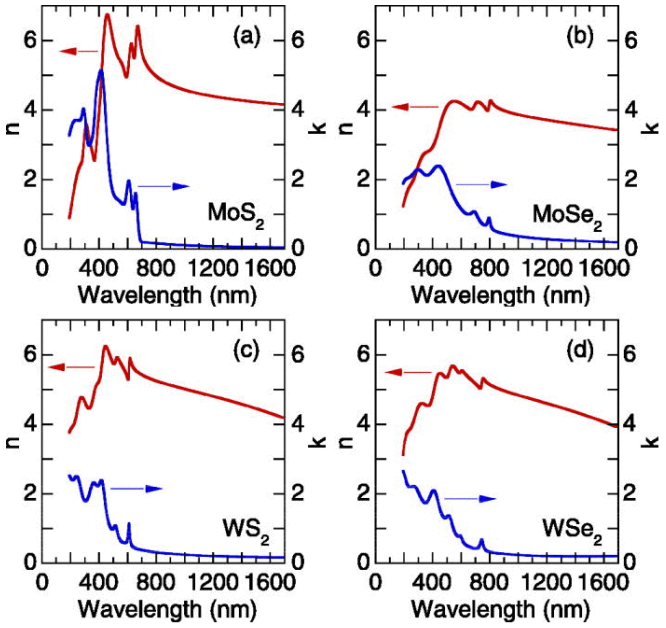


**Figure 1.4:** Refractive index n and extinction coefficient k of monolayer (a) MoS2, (b) MoSe2, (c) WS2, and (d) WSe2 thin films. Adapted from Hsiang-Lin Liu et al., Appl. Phys. Lett. (2014).

The corresponding bandgaps can also be observed in the extinction coefficient k between 600 and 800 nm and can be characterized by optical transmission or photoluminescence measurements.

### 1.3.4 Radiation-Resistance

Radiation hardness is an important characteristic of TMDCs and is beneficial for space applications. Arnold et al. showed that an $MoS_2$ FETs maintained a high currents and on/off ratios while being exposed to $He^{2+}$ fluence of $10^{15}$ ions/cm$^2$ or proton fluence of $1.26 \times 10^{16}$ ions/cm$^2$, corresponding to thousands of years of proton and alpha particle irradiation in space. [38] Additionally, Vogl et al. studied the performance of $WS_2$ devices under excessive γ-radiation and saw an increase in photoluminescence in the $WS_2$ film. The photoluminescence increase was attributed to decreased defect densities, increased carrier lifetime and a change in doping ratio proportional to the photon flux. [39], [40] Both groups showed that due to the atomically thin nature of TMDCs, there was relatively low damage resulting from the high radiation, highlighting the superior radiation resistance properties. The space industry can benefit considerably from a material that exhibits excellent radiation resistance along with strong light harvesting capabilities and flexibility as discussed in Chapter 4, where flexible photovoltaics are discussed.

### 1.3.5 Thermal Properties

Another interesting characteristic of TMDCs is their thermal resistance. The melting point ranges from few hundreds to thousands of °C. The high temperature melting points are especially impressive since the interlayer bonds are vdW bonds compared to the covalently bonded chalcogenides like S, Se and Te that melt at temperatures less than 500 °C. For example, the melting point of $MoS_2$ is 1185 °C compared to S and Se, which melts

at 115 and 220 °C respectively. [41] This property is important in the fabrication process like the photovoltaic device fabrication in this work where the material is annealed at 120 °C.

### 1.3.6 Electrical Properties

An important property in semiconducting materials that determines their usefulness in electronics and photovoltaic applications is the carrier mobility. In ultrathin materials, defects and scattering phenomena have a more significant effect on carrier mobility compared to bulk materials. The electron mobility of Silicon and Germanium can be within the thousands of $cm^2/Vs$ and graphene > 1 x $10^4$ $cm^2/Vs$, whereas 2D TMDCs have yet to exceed the hundreds of $cm^2\ V^{-1}\ s^{-1}$ mark, [42], [43] However, research efforts have been aimed at understanding and improving their carrier mobilities and designing of suitable devices. Kim et al. showed that the field-effect mobility of fabricated $MoS_2$ transistors increased from ~10 to ~18 $cm^2\ V^{-1}\ s^{-1}$ as the channel thickness increased from 1 to 6 layers, [44] showing that there is also a mobility dependance on the number of layers. A similar trend was observed by Robertson et al. [45] This is an important electrical property to be considered for the future of this work.

## 1.4 Overview

In Chapter 2, the Synthesis of monolayer 2D $MoS_2$ thin films is discussed. The $MoS_2$ films were synthesized by tube furnace CVD via the reaction of sulfur (S) with molybdenum oxide ($MoO_3$) precursors at 750 °C on C-plane sapphire substrates. Sapphire substrates provide the platform for large area quasi-epitaxial growth, where a 3-on-2 superstructure of $MoS_2$ (lattice constant 3.212 Å) and sapphire (lattice constant 4.814 Å) is expected. The efficient transfer techniques used for transferring the films to the desired substrate for characterization and device fabrication is also presented. The technique takes advantage of the weak van der Waals (vdW) inter-layer bonds in these layered materials and the hydrophobicity of the transfer polystyrene (PS) film to separate the as grown $MoS_2$ film from the growth substrate. The relevance of the common characterization techniques, namely Raman spectroscopy, photoluminescence spectroscopy, transmission electron microscopy, optical transmission, and atomic force microscopy, is discussed. For 2D devices, photocurrent spectroscopy maps can reveal properties such as the photothermoelectric effect at the material and contact interface and photovoltaic effect at a Schottky junction; PL can characterize thickness and electronic structure properties and material quality; optical transmission spectroscopy can give film thickness and layer dependent absorption information; and Raman spectroscopy can show structural and layer properties as discussed in the chapter. Lastly, the design of a single station setup with the ability to produce correlative maps for the characterization of 2D devices, and the fabrication of the devices for characterizing the electrical properties of the films is also presented.

Chapter 3 covers the ability to use the CVD film synthesis technique to produce large area $MoS_2$ films of various morphologies and presents the use of correlative spatial mapping of the 2D $MoS_2$ based films and devices to show the relationship between various growth morphologies and optoelectronic device performance. We demonstrate the quazi-epitaxial synthesis of large area $MoS_2$ 2D structures on C-plane sapphire through an optimized CVD process. The $MoO_3$ precursor and growth time was optimized to repeatedly grow films of various morphologies, from sparse flakes to uniform monolayer films and films with multilayer islands, with well aligned flakes > 20 μm. These 2D materials are fabricated into phototransistors using single and multiple monolayer structures on a transparent substrate to facilitate correlative spatial mapping and the characterization of both material and device properties. The dependence of large area 2D $MoS_2$ phototransistor performance on film morphology is shown through the correlation of high-resolution Raman, photoluminescence, transmittance, photocurrent, and generated external and internal quantum efficiency spatial maps. For example, by comparing the device performance to the spatial maps, we show that the photoluminescence peak shift and intensity reveals strain and other defects in various film morphologies that inhibit photogenerated current in the $MoS_2$ phototransistors. By increasing the thickness of the absorber layer, higher performance can be achieved. Finally, by stacking monolayers using the surface energy assisted transfer process, we show that monolayer Raman signature peaks are maintained, even where multiple monolayers are stacked.

In Chapter 4, the design, fabrication, and characterization of large area $MoS_2$ Schottky photovoltaics on flexible substrates are described. The discussion focuses on the benefits of 2D materials photovoltaics for space application, including an example of the economic benefits. The discussion highlights and benefits of 2D PV as an ideal alternative to conventional PV for space applications by comparing power performance and other properties including radiation resistance, flexibility, and specific power. The report covers the design, modeling, fabrication, and characterization of a 2D $MoS_2$ PV module to power a 6U CubeSat. The results show even at lower power conversion efficiencies (PCE), their specific power and cost to deploy in space advantages compared to the passivation emitter rear contact cell (PERC) array most commonly deployed space PV technology, makes them an attractive option for space PV.

In Chapter 5, the design, fabrication, and characterization of high-performance large area $MoS_2$ vertical Schottky photovoltaics is discussed. Several groups have suggested that a significant improvement in 2D PV performance can be attained with a vertical carrier transport architecture; therefore, the discussion focuses on the benefits of vertical architecture over lateral architecture and explores the benefits with a 2D PV model. Such architecture requires the use of a transparent top contact with low optical absorption, such as graphene or transparent conductive oxides (TCOs). The design and modeling for large area Schottky solar cells are presented with asymmetric work function ITO and Pt contacts. Model results predict that a vertical architecture device outperforms the lateral device in both $J_{SC}$ and $V_{OC}$, leading to higher efficiencies, and suggest that high performance solar cells can be achieved using these 2D TMDC materials.

Chapter 6 summarizes the findings of this dissertation and their impact on the future of optoelectronic devices and solar cells from 2D nanomaterials. The chapter also points to future directions for the field to build on this work. Appendices provide additional data, products associated with this work, and fabrication protocol for the reported materials and devices.

# CHAPTER 2

# LARGE AREA SYNTHESIS, TRANSFER AND CHARACTERIZATION OF CVD GROWN $MoS_2$

Two dimensional 2H molybdenum disulfide ($MoS_2$) has been an attractive material for optoelectronic devices since the discovery of its indirect-to-direct bandgap transition from bulk to monolayer as a result of quantum confinement, highlighting the expected high specific power harvesting capability. [46] 2D $MoS_2$ also has excellent mechanical strength and chemical stability, however compared to graphene, which possesses carrier mobility in excess of 15,000 $cm^2\ V^{-1}\ s^{-1}$, [13] $MoS_2$ has lower carrier mobility in the order of tens to a few hundreds of $cm^2\ V^{-1}\ s^{-1}$. [42] However, with a bandgap of ~1.88 eV, $MoS_2$ can be used in optoelectronics and photovoltaics. While mechanical exfoliation of $MoS_2$ samples from bulk $MoS_2$ crystals result in high-quality flakes, the large-scale production of wafer scale devices requires the synthesis of large area films. Chemical vapor deposition (CVD) techniques along with other synthesis methods are being developed and optimized by researchers for this purpose and expected to lead to large-scale production of 2D material-based devices.

## 2.1 Large Area CVD Synthesis of Monolayer $MoS_2$

In this work, the CVD $MoS_2$ growth technique was used to produce cm-scale $MoS_2$ monolayer films by a gas-phase reaction of sulfur (S) with molybdenum oxide ($MoO_3$), using ultrahigh-purity argon as a carrier gas. A 1 inch diameter quartz tube was placed in a three-zone furnace for $MoS_2$ synthesis as shown in **Figure 2.1**. An alumina crucible was used to hold the substrate and the $MoO_3$ powder. The growth substrate was placed in the

crucible 0.5 cm from the downstream end of the alumina crucible and was suspended at 1cm above the floor of the crucible. The $MoO_3$ powder was placed 15 cm from the upstream end of the substrate with the $MoO_3$ powder centered in zone 2. The 230 mg of sulfur powder was placed in a crucible in zone 1 with the front end of the sulfur crucible 30 cm away from the upstream end of the substrate. The tube was initially vacuumed down to a pressure of 15 mTorr, then Ar was flowed at a flow rate of 180 sccm, with the tube pressure maintained at 2.4 torr. The temperatures of the second and third zones of the furnace were both set to 750 °C with a 30 min ramp time. At the end of the ramp, zone 1 was heated up to 120°C for the sulfur vapor to flow downstream and zones 2 and 3 area held at 750°C throughout the duration of the growth. Zone 3 acts as a buffer zone for delayed and further downstream condensation of excess reactants and precursors.

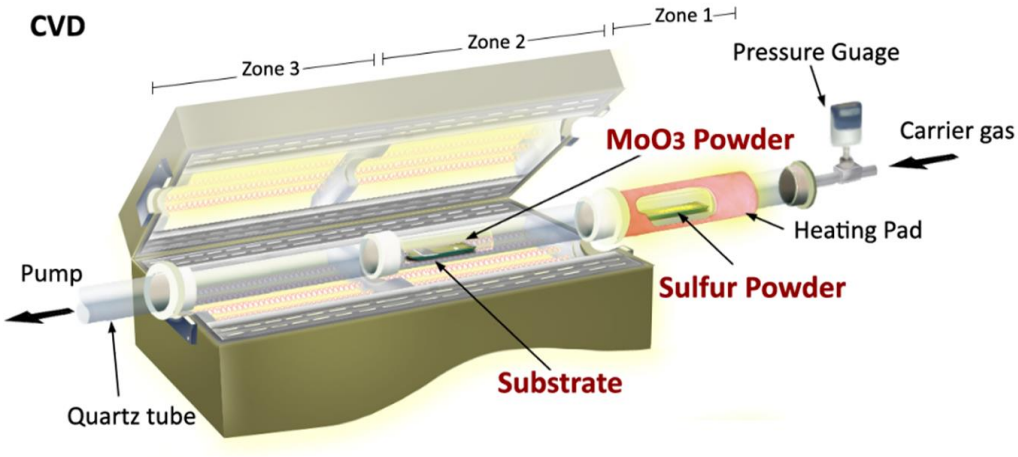


**Figure 2.1:** Schematic of the CVD synthesis showing the three heating zones and substrate and precursor locations. Adapted from Islam et al., Adv. Photonics Res. (2021).

Using sulfur and $MoO_3$ as precursors for the CVD-growth of $MoS_2$ the reaction is as follows:

$$2MoO_{3(g)} + 7S_{(g)} \rightarrow 2MoS_{2(s)} + 3SO_{2(g)} \quad \textbf{Eq. 2.1}$$

Synthesis on amorphous $SiO_2$ substrates result in randomly oriented of $MoS_2$ domains as shown in **Figure 2.2a**, however cm scale domain orientation control is achieved by using an atomically smooth crystalline sapphire ($Al_2O_3$) substrate. [47] Due to a lattice mismatch between $MoS_2$ and the C-plane (0001) sapphire surface of less than 4.7%, [48] quasi-epitaxial domain growth that subsequently coalesce into a uniform monolayer film is obtained as shown in **Figure 2.2b-d**.

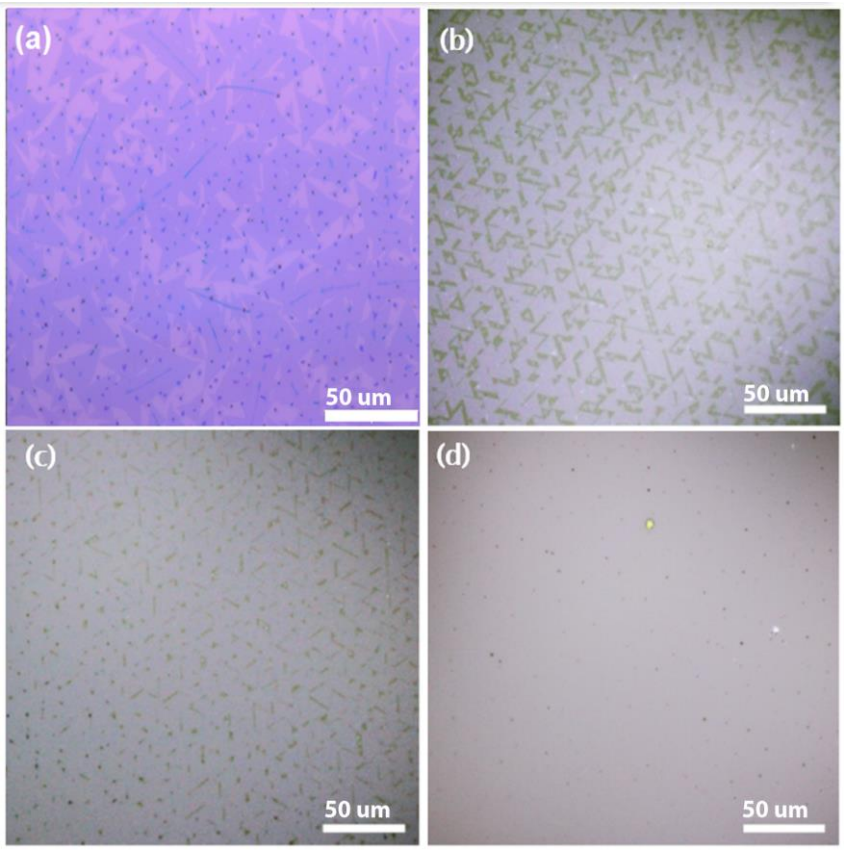


**Figure 2.2:** CVD synthesized $MoS_2$ flakes with (a) random orientation and flake morphology on $SiO_2$ substrate and highly oriented flakes from (b) sparce, (c) to less sparce, (d) to film coverage.

For quasi-epitaxial $MoS_2$ synthesized by CVD on $Al_2O_3$ substrates, the domain morphology depends strongly on the precursor flux, and growth time, and the growth mechanism follows the Stranski–Krastanov "layer-plus-island" thin film growth. Although lower $MoO_3$ flux result in larger domain sizes and less island formation, the right combination of $MoO_3$ flux and sulfurization time is needed under a set pressure, temperature, and carrier gas flow rate to synthesize a uniform large area epitaxial growth of $MoS_2$ film on C-plane $Al_2O_3$ substrates. This is investigated more closely in Chapter 3.

## 2.2 Large Area 2D $MoS_2$ Film Transfer

The grown films are transferable to any arbitrary substrate for device fabrication using a surface energy assisted layer transfer technique, [49] shown in **Figure 2.3**, that takes advantage of the van der Waals (vdW) bonds in these layered materials. A polystyrene (PS)-toluene solution is spin-coated onto the as grown $MoS_2/Al_2O_3$ leaving a PS film after the toluene solvent evaporates and the film is baked for uniformity and adhesion. Deionized water was used to lift the $PS/MoS_2$ stack with little mechanical wear on the films by taking advantage of the hydrophobicity of the $PS/MoS_2$ and the hydrophilicity of the $Al_2O_3$ substrate.

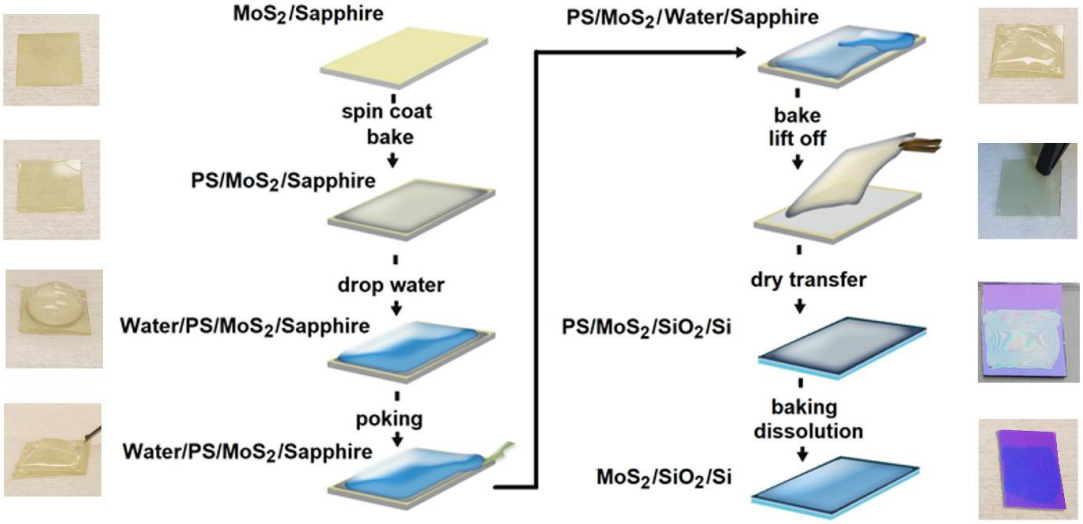


**Figure 2.3:** Schematic of surface energy assisted transfer of $MoS_2$ films.

The flakes and film are undamaged during the transfer process as shown in **Figure 2.4.** The triangular shape of the flakes is maintained post transfer showing that minimal mechanical damage is experienced using this transfer technique.

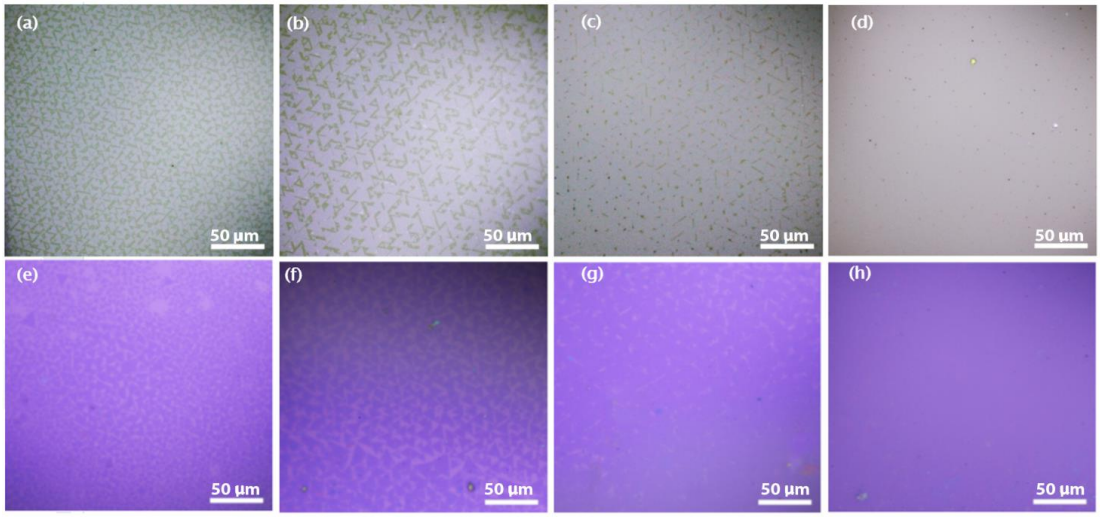


**Figure 2.4:** a-d) CVD synthesized $MoS_2$ on $Al_2O_3$ substrate from flake to film morphology and e-h) surface energy assisted transferred $MoS_2$ flakes to film unto $SiO_2$ substrate.

## 2.3 Further $MoS_2$ Film Characterization

The optical image of the synthesized $MoS_2$ from the CVD technique shown in **Figure 2.2**, showed that the flake sizes are within tens of micrometers in width. To ascertain the thickness of the $MoS_2$ flakes, atomic force microscopy (AFM) was used to measure the step edge of an $MoS_2$ flake on the C-plane $Al_2O_3$ substrate. The height profile in **Figure 2.5a** shows that the thickness of the $MoS_2$ flake is 0.61 nm, which corresponds to monolayer $MoS_2$. The flakes were transferred to a copper grid and characterized using tunneling electron microscopy (TEM) and selected area electron diffraction (SAED) to obtain the $MoS_2$ monolayer diffraction pattern shown in **Figure 2.5b** and the bilayer pattern shown in **Figure 2.5c**. The hexagonal patterns indicate that the crystal structure is the hexagonal structure of monolayer $MoS_2$ while a second hexagonal pattern indicates bilayer. In **Figure 2.5c**, one layer is slightly rotated.[50]

Raman and transmittance measurements were also used to characterize the synthesized $MoS_2$. A Perkin Elmer LAMBDA 750 UV/Vis/NIR Spectrophotometer was used to measure film transmittance. The results are shown in **Figure 2.5d**. The A (662 nm), B (617 nm) and C (432 nm) absorption peaks and the band edge at ~670 nm $MoS_2$ are shown.[45] Additionally, **Figure 2.5e** shows the Raman spectrum of the $MoS_2$ samples with the $MoS_2$ Raman peaks of the $A_{1g}$ to $E^1_{2g}$ modes at 413 cm $^{-1}$ and 390 cm $^{-1}$ respectively, and the difference of ~21 cm $^{-1}$ between the modes, indicating the characteristic $MoS_2$ monolayer Raman peak location difference. [51] The difference increases with the transition from monolayer to bulk. Photoluminescence (PL) was also used to characterize the $MoS_2$. The PL for a flake, partially coalesced and well coalesced film sample are shown in **Figure 2.5f**. The characteristic A exciton peaks at ~670 nm

indicate monolayer $MoS_2$ for each sample with the intensity of the peaks increasing from flakes to film.

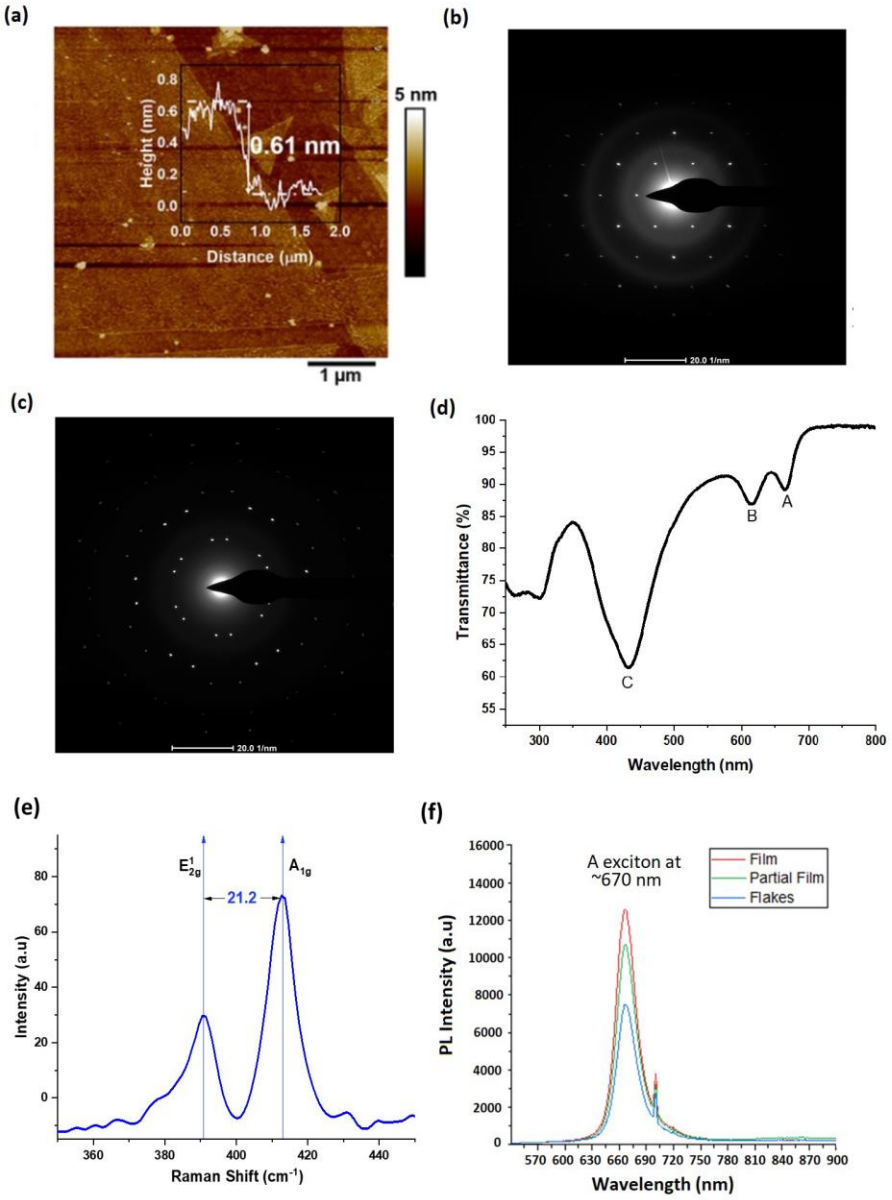


**Figure 2.5:** Monolayer $MoS_2$ (a) AFM measurement showing a monolayer thickness of 0.61 nm. (b) SAED hexagonal diffraction pattern for monolayer $MoS_2$ and (c) SAED hexagonal diffraction pattern for bilayer $MoS_2$ hexagonal TEM measurements, (d) transmission measurements for a monolayer film with the A (662 nm), B (617 nm) and C (432 nm) peaks labeled, (e) characteristic Raman peak and Δ for monolayer $MoS_2$ and (f) photoluminescence for flakes, partial film and film samples.

## 2.4 Single Station Setup for Spatial Characterization

Efficient absorbers like $MoS_2$ are considered good candidates for applications in optoelectronics and photovoltaics. However, predicted device performance is significantly affected by localized defects such as grain boundaries and non-uniformity in large-area films, including regions with varying number of atomic layers. A variety of techniques have proven to be important in characterizing the optical and electronic properties of atomically thin TMDCs. Techniques for spatially localized material property investigation will help accelerate device development from these materials. We demonstrate an optical microscope setup for measuring the transmittance, photoluminescence (PL), and photocurrent (PC) spectroscopy with <1 μm spatial resolution. The instruments and motorized stage are integrated into a single LabView VI as shown in **Figure 2.6**.

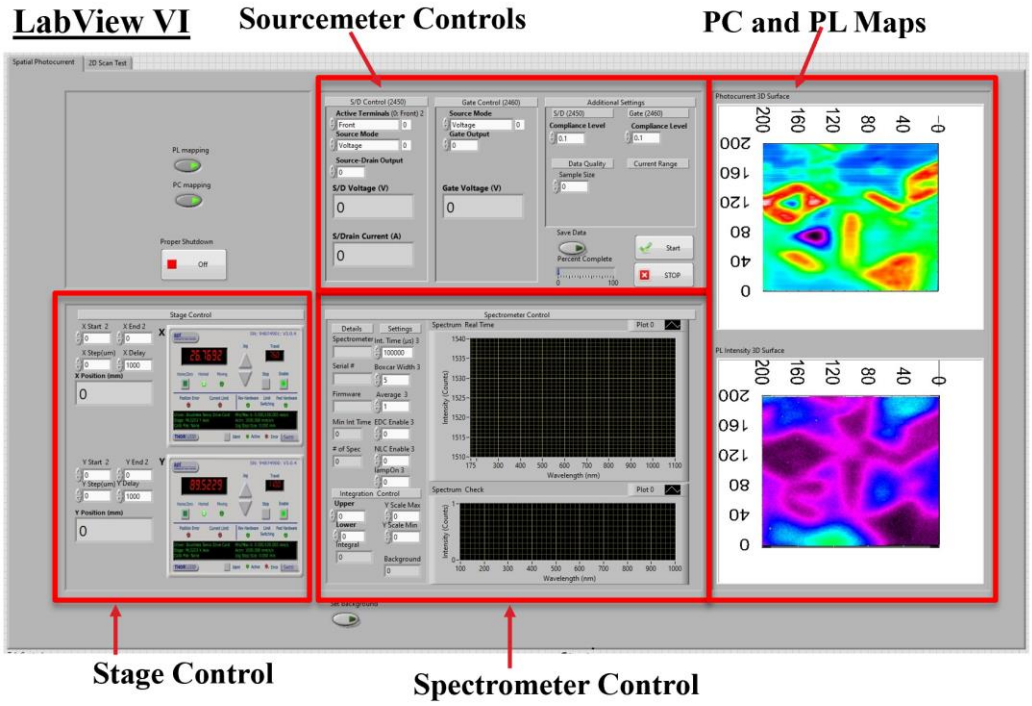


**Figure 2.6:** LabView VI for material and device spatial mapping using photoluminescence, photocurrent and transmittance characterization techniques.

By correlating each of these measurements over the same material or device region, we can draw connections between material properties and device performance. Our light source is a supercontinuum laser (Fianium/NKT Photonics) with laser line tunable filter, facilitating wavelength dependent excitation and optical studies of the $MoS_2$ flakes. Shown in **Figure 2.7** is a schematic of the single station setup with all the components for spatial mapping using photoluminescence, photocurrent and transmittance characterization techniques, and the setup can easily be adapted for Raman spectroscopy mapping.

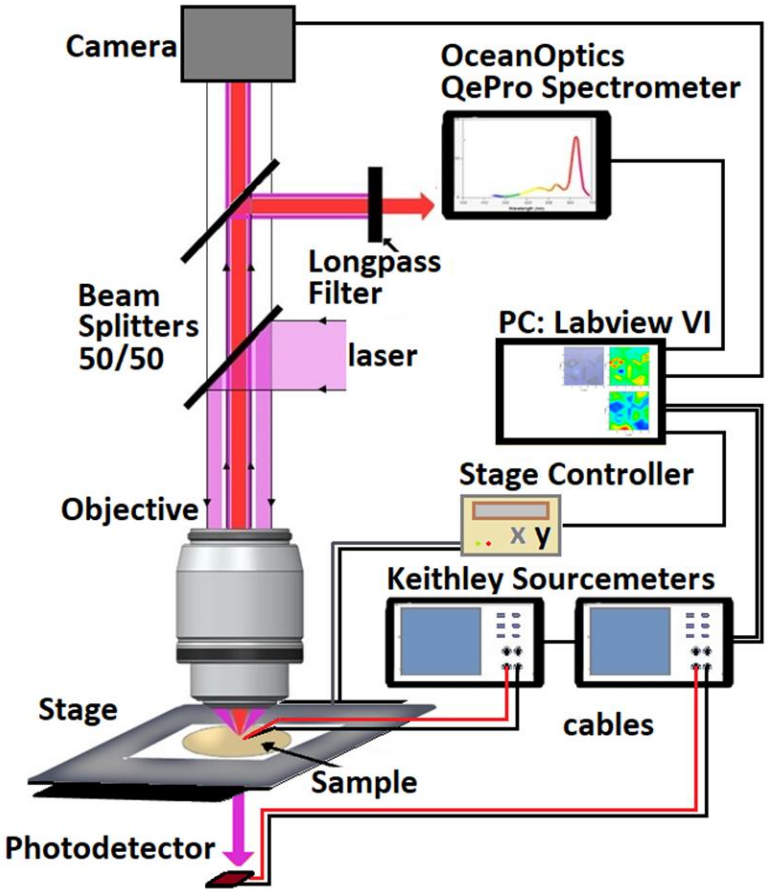


**Figure 2.7:** Schematic of the single station lab table setup with all the components for TMDC material and device spatial mapping using photoluminescence, photocurrent and transmittance characterization techniques.

PL mapping of $MoS_2$ flakes and films are carried out by exciting single and few-layer thick $MoS_2$ samples with a monochromatic 405 nm excitation; emitted PL is measured using an Ocean Optics QePro spectrometer as shown schematically in **Figure 2.8a**. Transmittance measurements are carried out with Thorlabs FDS1010-CAL calibrated photodiode mounted 1mm beneath the sample on a transparent stage for the reference and sample measurements. The setup is shown in **Figure 2.8c**. The 2D material-based devices contact are probed and the device photocurrent is measured using a Keithley 2450 sourcemeter as shown in **Figure 2.8b**. An MLS203-2 is XY scanning stage was used in each setup to facilitate spatial mapping, with all the components integrated with a LabVIEW virtual interface for data collection.

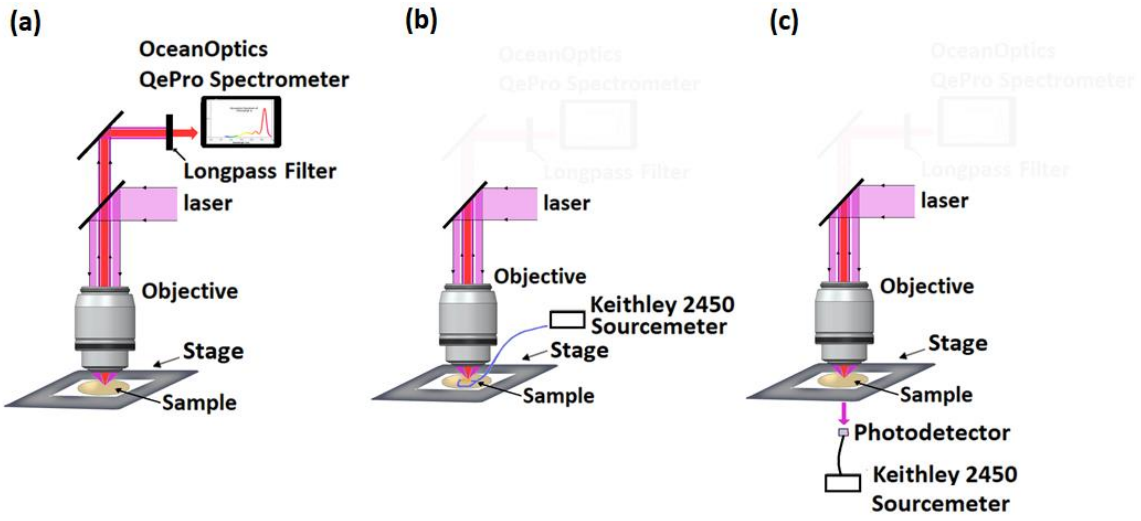


**Figure 2.8:** Schematic of the single station lab table setup for TMDC correlative mapping for (a) photoluminescence, (b) photocurrent and (c) transmittance characterization techniques.

## 2.5 Correlative Mapping of Optical and Electronic Properties in $MoS_2$

While each technique individually yields insightful information on the uniformity and properties of the 2D material, the integrated setup enables spatial correlation of properties as they relate to the performance of 2D photovoltaics, photodetectors, and other optoelectronic devices. From correlated PL and transmittance measurements we extract absorption and photogeneration information that enables mapping localized external radiative efficiency. Additionally, transmittance measurements probe wavelength absorption and reflectance and their dependence on local defects.

**Figures 2.9a, b** and **c** show the optical image, transmittance map and PL map of CVD synthesized $MoS_2$ triangular crystals on C-plane $Al_2O_3$ substrates**.** The contrast variation of the $MoS_2$ domains in the optical image shows a clear difference in coverage and thickness. The darker regions are the substrate due to the low reflection/high transmittance of the $Al_2O_3$. The lighter regions are monolayer $MoS_2$ while the most reflective triangular region is a small $MoS_2$ crystal on top of a larger crystal. A transmittance map of the $MoS_2$ within the same field of view showed that the regions of bi-layer $MoS_2$ transmitted ~78% of the incoming radiation while the monolayer regions transmitted 85% as reported. [45] Although the optical image shows consistent contrast of the region circled in red with other regions with monolayer transmittance, the transmittance map at that location is non-uniform and has a range of transmittance between 85% and 90%. The PL map of the same location shows lower photoluminescence at the bilayer region, consistent with the decrease in radiative efficiency expected from the direct to indirect bandgap transition of 2D $MoS_2$. Additionally, PL intensity was non-uniform and varied in intensity across regions of uniform contrast in the optical image. The

corresponding region on the transmittance and PL maps circled in purple, where monolayer is confirmed through transmittance measurements, showed no PL. This indicates that even with uniform optical properties, non-uniformity in the electronic properties across the sample can exist.

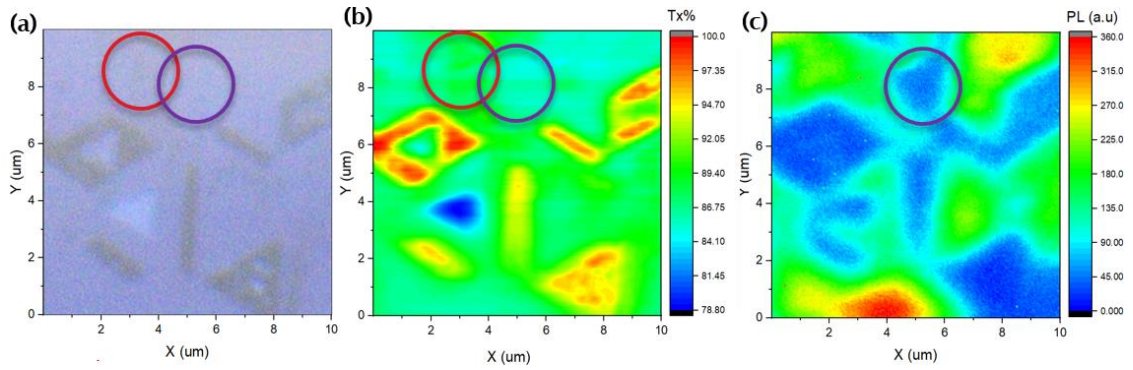


**Figure 2.9:** $MoS_2$ flakes on C-plane $Al_2O_3$ substrate's (a) optical image, (b) transmittance map and (c) photoluminescence map.

**Figures 2.10a, b** and **c** show the optical image, transmittance map and PL map of a CVD synthesized $MoS_2$ film on $Al_2O_3$ substrates**.** The contrast of the $MoS_2$ in optical image shows uniform thickness. A transmittance map of the same the region had the monolayer transmittance of across 90% of the sample, However, some regions of > 85% transmittance indicated that the film was not well coalesced and the top right blue region in the transmittance map revealed a single layer $MoS_2$ island on top of the film. Furthermore, the PL map showed non-uniformity in the electronic properties across the mapped region.

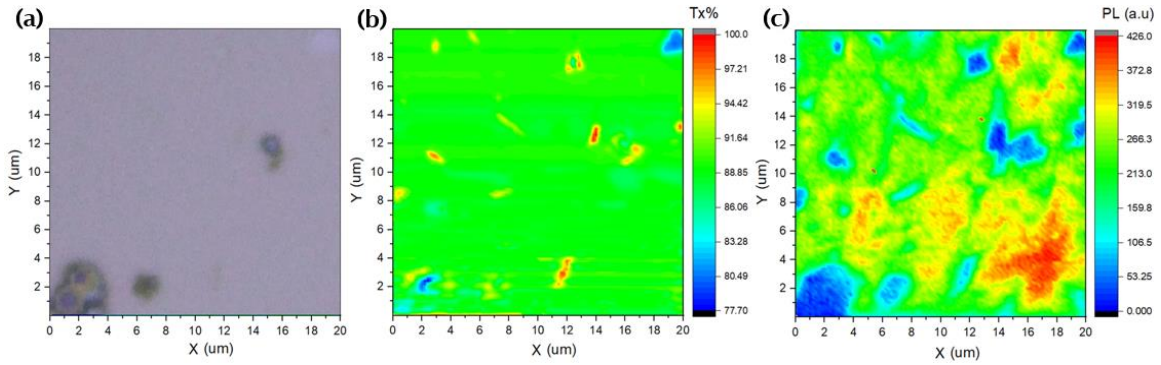


**Figure 2.10:** $MoS_2$ film on C-plane $Al_2O_3$ substrate's (a) optical image, (b) transmittance map and (c) photoluminescence map.

## 2.6 Photocurrent Mapping of Electronic Properties of $MoS_2$

The performance of optoelectronic and photovoltaic devices is a function of the carrier diffusion length withing the active medium. The longer the carrier diffusion length, the higher the probability of collection at the contacts. Scanning photocurrent microscopy can be used to estimate the carrier diffusion length directly by mapping the current induced by a laser source. [52]–[54] To show this, phototransistors were fabricated in the as-grown $MoS_2$ films on the $Al_2O_3$ substrate. The fabrication is shown schematically in **Figure B.1,** (Appendix B) and the steps are presented in **Section F.1** (Appendix F).

We measured the photocurrent of a $MoS_2$ photovoltaic device using a 660 nm laser and a 1 μm spot size and scanning across the contact edge as shown in **Figure 2.11a**. The collected current was greatest near the contact edge and decreased as the laser spot moved away from the contact edge creating the collected current line profile of the photocurrent as a function of distance from the Pt contact edge.

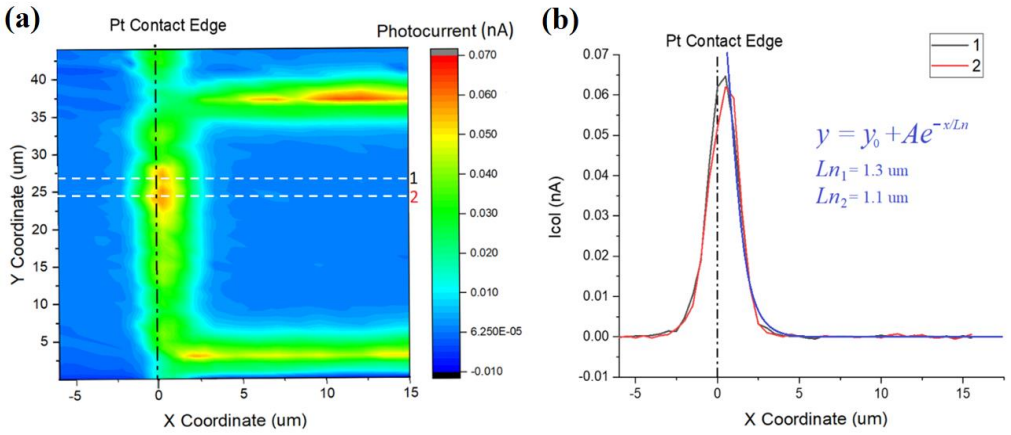


**Figure 2.11:** a) Photocurrent map measured on a 2D PV device with the black dashed line showing the Pt contact edge and the white dashed lines showing where photocurrent is plotted in (b). (b) Photocurrent line profiles as a function of the laser position x, scanned across the Pt contact edge.

The collected photocurrent $I_{col}$ follows a 1D exponential function for x > 0, as follows:

$$I_{col} = \frac{eG}{2} + exp\,(-\frac{x}{Ln}) \qquad \textbf{Eq. 2.2}$$

where *e* is the electron charge and *G* is the electron generation rate. $Ln = D_n\tau_n^{1/2}$ is the diffusion length where $D_n$ is the diffusion coefficient and $\tau_n$ is the electron lifetime. By fitting the photocurrent curve in **Figure 2.11b** with a simple exponential function, we extracted an $L_n$ of ~1.2 μm.

## 2.7 Uniformity Characterization of CVD Synthesized 2D $MoS_2$ Film

As discussed in the previous chapter, material quality and scalability have been a challenge to date and is a hindrance to the use of ultrathin and ultralightweight 2D materials in many applications. To overcome this, the low cost and scalable chemical vapor deposition (CVD) process was optimized to obtain high quality, 1.5 $cm^2$ monolayer $MoS_2$ films, through quazi-epitaxial growth on an atomically smooth sapphire substrate surface, with $MoO_3$ and sulfur as the precursors [55]. A characteristic ~1.85 eV bandgap was measured using photoluminescence spectroscopy and reasonable uniformity of the electronic properties is revealed by PL mapping shown in **Figure 2.12a**. Furthermore, RAMAN spectroscopy spatial mapping (specifically mapping the spacing between the $A_{1g}$ and $E^1_{2g}$ peaks) revealed 85% of the film is confirmed monolayer, as shown **Figure 2.12b**, showing promise towards the fabrication of $cm^2$ scale 2D PV devices as opposed to $\mu m^2$ scale PV devices made to date from exfoliated 2D flakes.

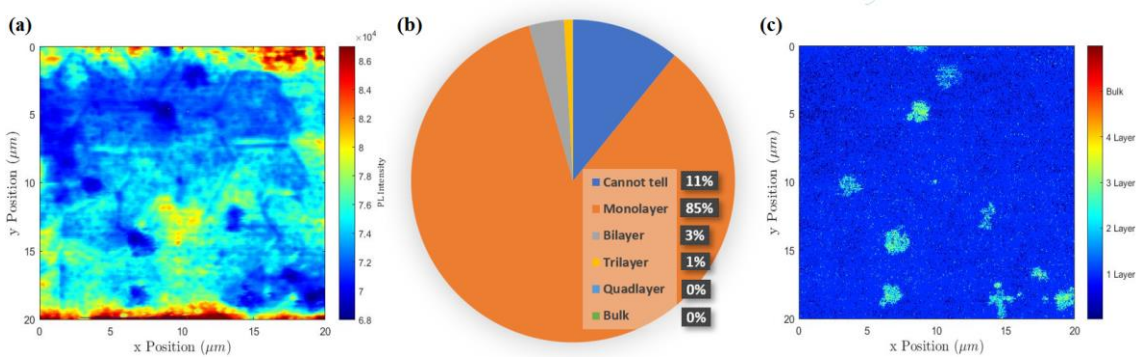


**Figure 2.12:** a) PL map of $MoS_2$ film showing coalesced domains, (b) pie chart showing the layer distribution from Raman mapping and (c) Raman peak spacing map of the $MoS_2$ film.

## 2.8 Enhanced Absorption by Stacking Monolayers

Due to the quantum nature of monolayer $MoS_2$, the same enhanced absorption per layer is not available from films directly synthesized with multiple layers. However, by stacking individual monolayers using the transfer technique shown in **Figure 2.3**, the monolayer absorption can be maintained, thus enhancing the total absorption of a stack. Raman measurements of the monolayer and 2 to 4 stacked monolayer samples were taken, and the results are shown in **Figure 2.13a.** The Raman data showed that the stacked monolayers Raman $A_{1g}$ to $E^1_{2g}$ vibrational modes peak difference of 21.5 $cm^{-1}$ was consistent with the single monolayer indicating that there was no monolayer to bulk transition from the sequential stacking of the monolayer $MoS_2$ films. We then studied the absorption of monolayer and few $MoS_2$ monolayer films experimentally by incrementally stacking the CVD grown monolayers and measuring the absorption after each layer transfer using a Perkin Elmer LAMBDA 750 UV/Vis/NIR Spectrophotometer. The results are shown in **Figure 2.13b**. The relative absorption increased with each layer in a manner associated with a direct bandgap material, and the enhancement in absorption points to an expected increase in photogenerated current in the $MoS_2$ active layer of a 2D $MoS_2$ phototransistor or photovoltaic device. This would lead to an increase in $J_{SC}$ and the overall efficiency of the 2D material based solar cell and indicates that stacked $MoS_2$ monolayers, synthesized at scale via CVD, is a promising candidate for optoelectronics and 2D PV applications.

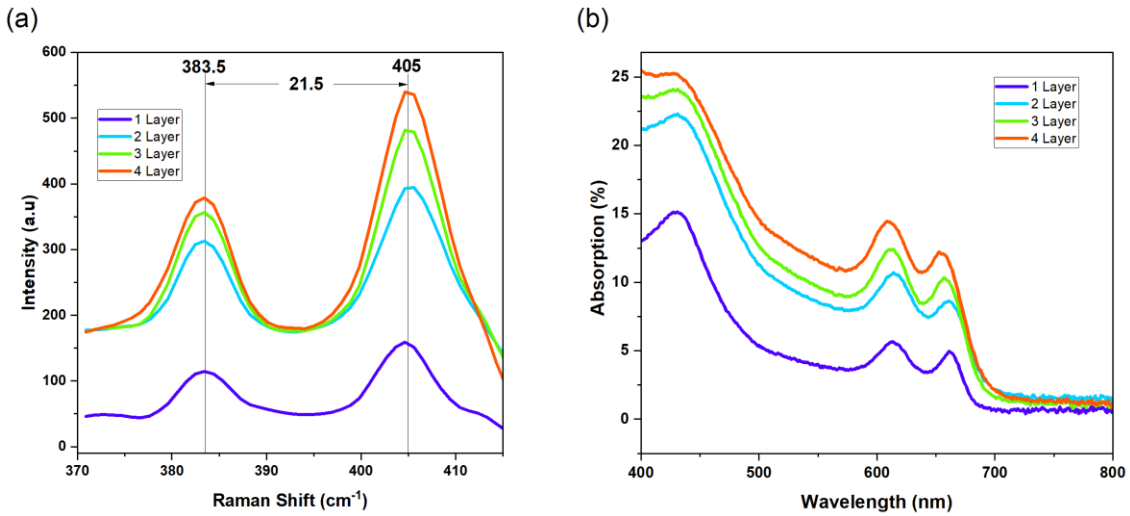


**Figure 2.13:** (a) Raman and (b) absorption results in $MoS_2$ monolayers, from a single layer to 4 stacked monolayers.

## 2.9 Electrical Quality

The carrier mobility is an important property in 2D TMDCs. Due to their ultra-thin nature, defects and scattering phenomena significantly affect the carrier mobility. To characterize the electrical quality of the films used in this work, the as-grown $MoS_2$ films were transferred onto an $Si/SiO_2$ substrate, then back-gated field effect transistors (FETs) as shown in **Figure 2.14** were fabricated on the transferred $MoS_2$ samples. These devices were made by patterning and depositing Ti/Au contacts onto the films by electron beam lithography and electron beam evaporation respectively. The fabrication steps are presented in **Figure B.2,** (Appendix B) and the steps are presented in **Section F.2** (Appendix F). The mobility extraction was carried out following the procedure discussed by Robertson et al. [45] The largest field effect mobility calculated from our devices was $\mu_{EF}$ = 3.66 $cm^2$ /(V·s). The relatively low mobility is attributed to the small domain sizes, grain boundaries and defects such as random sulfur vacancies that can be addressed through

further growth optimization and sulfur treatment by annealing in sulfur rich environment. [56] However, current mobility is sufficient for the devices in this work.

(a) (b)

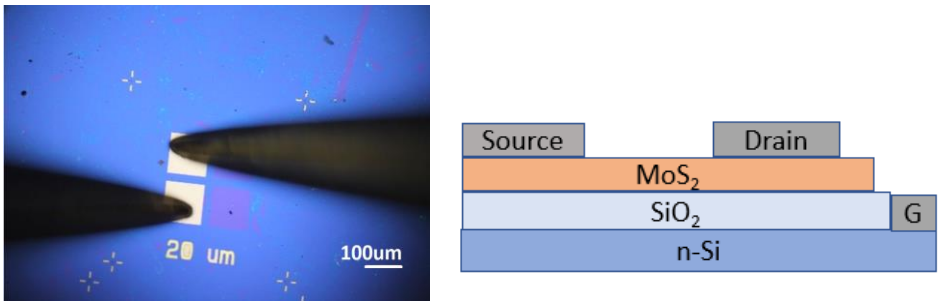


**Figure 2.14:** (a) Optical image of the source and drain contacts of a back-gated FET; (b) Schematic of a back-gated FET.

## 2.10 Conclusions

We show that the CVD process can be used to produce large-area monolayer $MoS_2$ films. Additionally, synthesis on $Al_2O_3$ substrates result in better uniformity than synthesis on $SiO_2$/Si substrates. The growth time and the right substrate can be used to produce larger domain sizes coupled with highly ordered domain alignment. This uniformity is expected to result in an increase in mobility and ultimately the improvement of 2D based optoelectronic and photovoltaic devices. Since the $MoS_2$ films only form weak van der Waals bonds with the growth substrate, the films can be easily transferred from the growth substrate to any target substrate. The surface energy assisted film transfer process leaves unnoticeable mechanical wear and tear on the film and provides the opportunity to fabricate devices on unique substrates such as flexible polymer thin-films. The number of layers in the $MoS_2$ film can be characterized efficiently through several characterization techniques

including atomic force microscopy (physical thickness), optical transmission (percentage absorption), Raman spectroscopy (Raman peak separation) and TEM SAED measurements (hexagonal diffraction pattern). Photoluminescence can reveal the bandgap of the $MoS_2$. Furthermore, combining these techniques for characterization through correlative maps can help with more in depth characterization of the material and devices. Collectively, these characterization techniques can accelerate the large-scale development of 2D material-based devices. Some of the benefits are presented in detail in **Chapter 3**.

## 2.11 Future Directions

The next step in synthesis involves the further optimization of film quality by treatments such as annealing in a sulfur rich environment to reduce sulfur vacancies. Additionally, efficient doping of 2D materials has been a challenge. It would be interesting to explore the large area synthesis of TMDCs with a combination of chalcogenides and/or dopants to facilitate vertical homojunction or heterojunction devices or to directly synthesize lateral heterojunctions films with a two-step synthesis process by masking half of the growth substrate for the initial TMDC, and then growing the second film.

Work will be done to improve film absorption and mobility by stacking monolayers instead of growing bulk $MoS_2$ films. This will be done firstly by transferring a monolayer film, and then stacking multiple monolayers of the CVD grown $MoS_2$ films to understand the relationship between multiple stacked layers and the device properties.

An addition to the single station setup, that would provide more efficient spatial characterization of the crystal structure homogeneity in our samples and accelerate the large-scale development of 2D material-based devices, is Raman mapping. Therefore, the

next step in this work involves the addition of a Raman spectrometer with the setup. Low temperature measurement capability can also be integrated with the setup to facilitate measurements that are highly temperature-dependent, such as electroluminescence.

# CHAPTER 3

# MORPHOLOGY CONTROL AND CORRELATIVE SPATIAL MAPPING OF EPITAXIALLY GROWN LARGE AREA 2D $MoS_2$ ON C-PLANE $Al_2O_3$ SUBSTRATES

With a direct bandgap of ~1.88 eV, monolayer $MoS_2$ can be used in optoelectronics and photovoltaics applications where semiconducting properties, high specific power and flexibility are desired. While mechanical exfoliation of $MoS_2$ samples from bulk $MoS_2$ results in high-quality few-layer crystals, the approach is typically limited to sub 0.01 $cm^2$ size films. The scalability of 2D materials-based technologies depends on the synthesis of high quality, sizeable (> 1 $cm^2$) films. Quazi-epitaxial CVD synthesis of $MoS_2$ films on C-plane $Al_2O_3$ is a scalable synthesis method optimized to produce wafer-scale monolayer $MoS_2$ films.[48] Generally, high crystallinity can be attained by seeding the substrate with promoters such as $MoO_3$ and NaCl for crystal nucleation at multiple points on the substrate, encouraging epitaxial growth with good domain alignment on substrates of suitable lattice such as GaN, BN, graphene, and mica. However, C-plane $Al_2O_3$ substrates provide step edges that can align with the armchair and zig-zag edges of $MoS_2$, thereby further promoting domain alignment at the right S/$MoO_3$ ratio.[57] Films synthesized on two inch c-plane $Al_2O_3$ wafers show a uniform and wrinkle-free monolayer film, with roughness as low as 100 pm. [48] Films with up to 99% unidirectional domain alignment and carrier mobilities of up to 102.6 $cm^2\ V^{-1}\ s^{-1}$,[47], [57] with consistent performance from 4 to ~80 μm channel length, have been shown using this growth method. With this technique, synthesized films can be transferred to desired substrates using various transfer techniques, [49], [58]–[60] which is useful for applications that require varying substrates, such as

large area flexible 2D phototransistors and 2D photovoltaics.[61], [62] However, domain boundaries and multilayer islands are common features in CVD synthesized $MoS_2$.[63], [64] Such defects can lead to mid-gap states, accompanied by undesirable charging effects and nonradiative recombination pathways.[65], [66] The domain boundaries and multilayer islands, along with local defects within single domains,[67], [68] reduce film conductivity and carrier lifetime and contribute to inhomogeneity in film properties that significantly influences device performance. Several techniques such as optical transmission, photoluminescence (PL), photocurrent, and Raman spectroscopy are commonly used to characterize both 2D materials and devices, and these techniques become even more powerful when spatially mapped over critical areas. For TMDCs and their devices, photocurrent spectroscopy maps can be used to investigate characteristics in devices such as photothermoelectric effect at the material and contact interface and photovoltaic effect at a Schottky junction;[69], [70] PL can be used to ascertain the thickness and electronic structure properties such as bandgap from the PL emission wavelength and the material quality from PL intensity; [71], [72] optical transmission spectroscopy can give film thickness and layer dependent absorption information;[73] and Raman spectroscopy can show structural and layer characteristics.[74] A better understanding on the interdependence of CVD synthesized $MoS_2$ film morphology and device performance through large area correlative mapping of the structural, optical, and electronic properties of the films can lead to the improvement of device design and performance. Such mapping can also illuminate the relationship between device geometry, local defects, strain, multilayer stacking, and more and how each characteristic plays a role on the generation and collection of carriers in a phototransistor. In this work, we tuned the CVD synthesis

parameters to obtain large area $MoS_2$ films of fully and partially coalesced flakes, flakes with bi-layer growth, uniform monolayer films, and monolayer films with bilayer growth. Additionally, layer transfer was used to examine multilayer films. We then used optical transmission, PL, and Raman spectroscopy to produce high resolution 20 x 20 μm spatial maps with 200 nm step size, which were subsequently correlated with photocurrent maps of large area $MoS_2$ based phototransistors that were fabricated with CVD synthesized films of varying morphology. From the correlative maps, we show that regions in the film with a strong PL result in higher photogenerated current under 660 nm incident light. Additionally, we combine photocurrent and absorption maps to generate high resolution external quantum efficiency (EQE) and internal quantum efficiency (IQE) spatial maps for the 2D $MoS_2$ based devices, illustrating the impact of various growth morphologies on optoelectronic device performance. Lastly, we fabricate a back-gated phototransistor using the CVD-synthesized large area monolayer $MoS_2$ film and show the transfer characteristics under different light illumination power.

## 3.1 $MoS_2$ Flake and Film CVD Synthesis and Morphology

The $MoS_2$ films in this work were synthesized by tube furnace CVD via the reaction of sulfur (S) with molybdenum oxide ($MoO_3$) precursors at 750 °C. C-plane sapphire substrates were used for quasi-epitaxial growth, where a 3-on-2 superstructure of $MoS_2$ (lattice constant 3.212 Å) and sapphire (lattice constant 4.814 Å) is expected.[47] Ultrahigh-purity argon was used as the carrier gas at 180 sccm flow rate. The sulfur precursor was heated to 120 °C when the furnace reached 750 °C, and the sulfur vapor was passed over the substrate for different sulfurization times to obtain different film morphologies. A schematic of the growth setup is shown in **Figure 3.1**, and the sapphire

substrates with films synthesized for 8 minutes of sulfurization time using an $MoO_3$ powder precursor of 0.5, 1, 3 and 5 mg shown in **Figure 3-1a, b, c,** and **d** respectively.

More details on the synthesis can be found in the Experimental Section. The films synthesized in this work were 1 $cm^2$ to 2.25 $cm^2$. The film size limitation was due to the 1-inch diameter quartz tube used for the synthesis process.

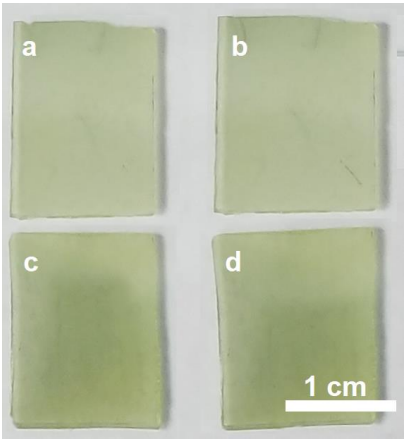


**Figure 3.1:** Optical image of films synthesized on the sapphire substrates for 8 minutes of sulfurization time using $MoO_3$ powder precursor of a) 0.5, b) 1, c) 3 and d) 5 mg.

An example of a domain is shown in **Figure 3.2g** (dashed white circle), where the edges of a single triangular flake that is partially coalesced with adjacent flakes can be easily identified by the difference in optical contrast. There is a gap between the lower edge of the domain and the adjacent domain, whereas the other two edges are partially merged with the adjacent $MoS_2$ flakes. In the CVD synthesis process, an increased or decreased $MoO_3$ vapor will typically lead to rapid or slow $MoS_2$ crystal formation, respectively. This can be achieved by increasing or decreasing the chamber temperature, carrier gas flow rate, or Mo precursor supply. The growth mechanism follows the Stranski–Krastanov "layer-

plus-island" growth, where "islands" are formed as vertical growth on top of monolayer flakes,[75], [76] resulting in few-layer $MoS_2$ regions. High Mo supply results in small domains and early island-like growth as shown in **Figure 3.2(a-f),** where 3 and 5 mg of $MoO_3$ were used. Interestingly, for a low Mo supply, domains are generally larger, but island-like growth can still occur even before the domains coalesce due to the increased nucleation sites on top of monolayer $MoS_2$ crystals or at domain boundaries as shown in **Figure 3.2l**. High performance, large area 2D material-based devices require large domains and continuous layer uniformity over the device active area. In pursuit of this goal, the Mo supply and growth time were swept to obtain the best synthesis parameters for large flakes with unidirectional alignment over large area that subsequently coalesce into a uniform monolayer film as shown in **Figure 3.2i**. For 0.5 mg of $MoO_3$, mainly flake sizes of ~10 μm or larger were obtained for 8 minutes of sulfurization time with no island formation. However, smaller flake sizes in the range of 1 to 5 μm with increased island formation arise for 3 and 5 mg of $MoO_3$ for the same 8 minutes, and the island density further increased with sulfurization time. Flakes larger than 10 μm were obtained for 0.5 and 1 mg of $MoO_3$. Islands formed for both 0.5 mg of $MoO_3$ with 12 minutes sulfurization and 3 mg of $MoO_3$ with 8 minutes of sulfurization without the domains being well coalesced. However, a well coalesced, large domain $MoS_2$ film with no islands was obtained for 1 mg of $MoO_3$ and 12 minutes of sulfurization. This film morphology is reproduceable over a large area as shown in **Figure C.1**, (Appendix C) and is repeatable in successive and ongoing growth attempts. Although lower $MoO_3$ flux results in larger flake sizes and less island formation, The adjacent flakes need to be well coalesced, therefore the right

combination of $MoO_3$ flux and sulfurization time is needed to synthesize a uniform large area epitaxial growth of $MoS_2$ film on C-plane $Al_2O_3$ substrates.

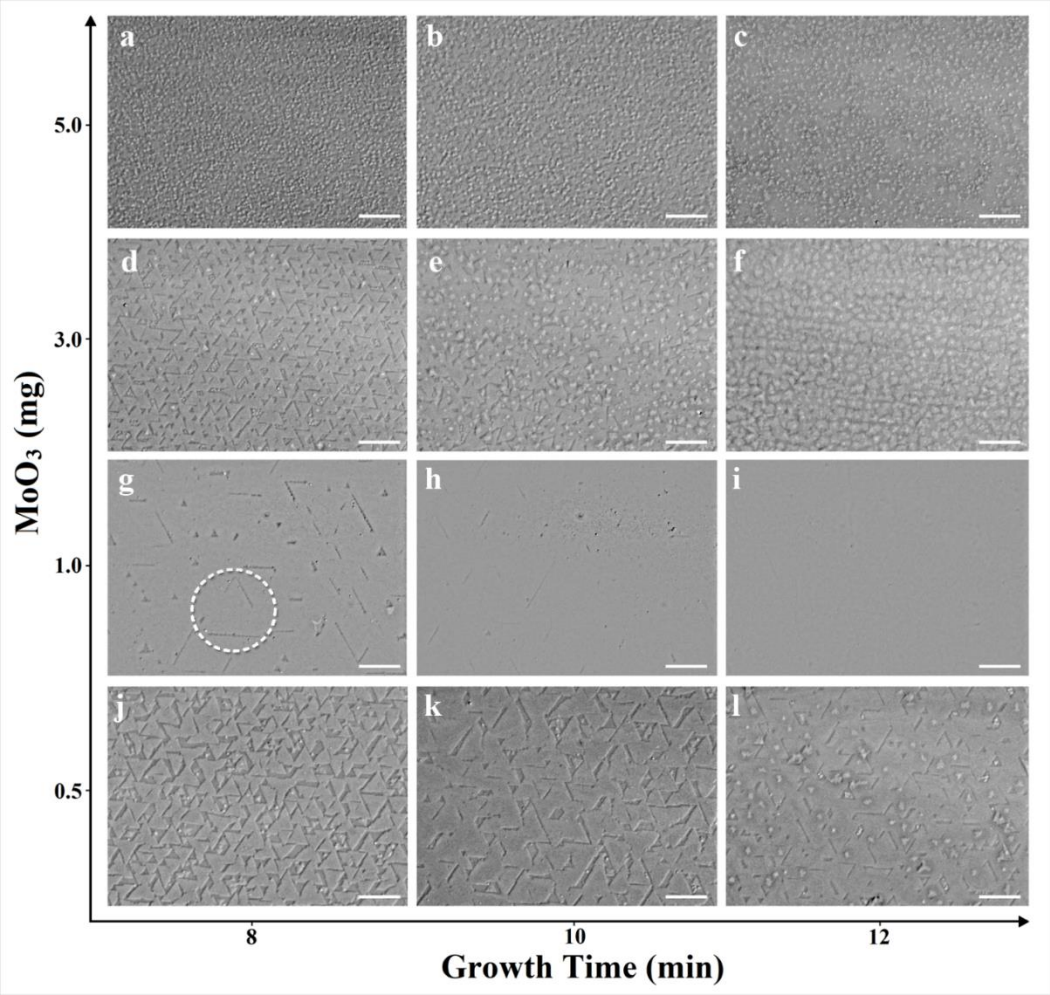


**Figure 3.2**: a-l) Optical images of CVD synthesized $MoS_2$ on C-plane sapphire substrates. As-grown $MoS_2$ flake and film morphology results from varying the amount of $MoO_3$ powder precursor (y-axis) and sulfurization time (x-axis). The scalebars are 20 μm.

## 3.2 Correlative Mapping

To illustrate the value of correlative mapping for 2D materials and devices, 2D $MoS_2$ films of varying morphology were grown on c-plane sapphire, and interdigitated

phototransistor contacts were fabricated on top to form a phototransistor and enable optoelectronic characterization. The transparent sapphire substrate enables measurement of optical transmission alongside other measurements. An optical image of a phototransistor with a monolayer $MoS_2$ film is shown in **Figure 3.3a** and the interdigitated contacts shown form the 0.15 $mm^2$ phototransistor active area. Fabrication of a device up to ~1 $cm^2$ active area is possible due to uniform film growth across the entire substrate. Films of similar area and uniformity were used as the active material for photovoltaics in our previous work.[62] Details on the device fabrication are discussed in the Experimental Section.

The transmission maps and photocurrent maps were produced during the same scan to account for any fluctuations in the light source and ambient conditions during the measurement, giving the correlation consistency needed to accurately calculate the EQE and IQE. The schematic of this optical table setup is shown in **Figure 3.3b**. The PL and Raman spatial maps were also performed simultaneously using an inverted Raman imaging confocal microscope. More details on the correlative map measurements are discussed in the Experimental Section. Due to scattering of photons within the substrate, and other non-local current spreading effects, photocurrent map resolution is broader than the 0.5 μm width incident laser spot. Because of this, incident light in locations with no $MoS_2$ still results in some photocurrent from carriers generated at different locations of the device; therefore, the spatial resolution is better in the absorption, PL and Raman maps than it is for photocurrent. Additionally, PL peak wavelength was mapped as well, as this revealed domain boundaries better than the PL intensity, since PL intensity is more sensitive to nonuniformity in film quality within domains. Finally, we map the spectral spacing

between the Raman $A_{1g}$ and $E^1_{2g}$ peaks, which provides additional insight into the number of $MoS_2$ layers at each point in space.[45]

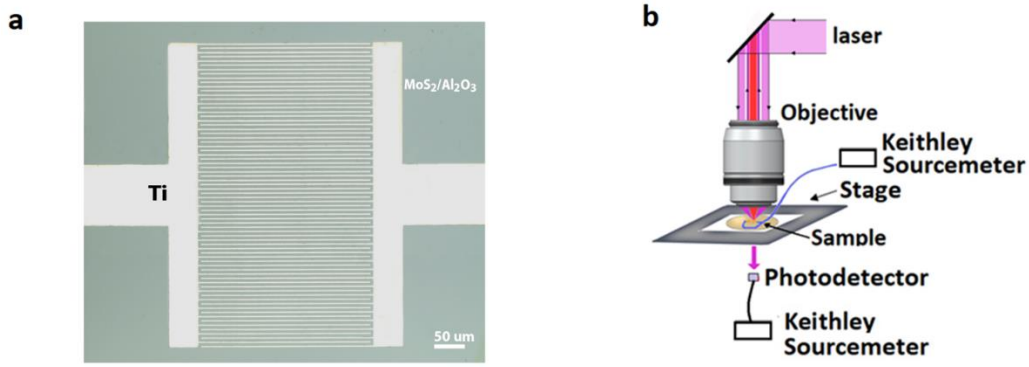


**Figure 3.3:** a) Optical image of a large area phototransistor fabricated on as-grown 2D $MoS_2$. b) The optical microscope-based setup for simultaneous spatial mapping of transmission and photocurrent.

### 3.2.1 Flake sample mapping

A film grown using 3 mg $MoO_3$ and 8 minutes of sulfurization time, as shown in **Figure 3.2d**, was selected for the flake sample correlative maps. The devices fabricated on 2D $MoS_2$ with non-coalesced flake morphology have domains with mostly unidirectional orientation within the channel, and the contacts are aligned so that one of the flake edges in the device channel almost run parallel to the contact edge, as shown in **Figure C.2**, (Appendix C). A channel length of 4 µm was chosen for the flake sample, where the triangular flake sizes were roughly estimated to be within 5 to 10 µm to ensure that most of a single flake spans the entire channel length. The flakes within the channel are partially coalesced, resulting in multiple film features in the channel active area. Some of these features are shown in the optical image **Figure 3.4a**, which has three metal contact fingers of width 4 µm running horizontally through the image. Location 1 shows a region where

the monolayer domains are well coalesced and locations 1, 2 and 4 show flakes that span the entire length of the channel. Smaller flakes with bilayer island growth can be seen in locations 3 and 4, highlighted by the difference in contrast, where the more reflective, lighter regions show multilayer $MoS_2$. The absorption spatial map **Figure 3.4c** complements the optical image, where ~5% and ~9% of the 660 nm incident light is absorbed in the monolayer and bilayer $MoS_2$ respectively. Furthermore, as depicted in **Figure 3.4i**, the bilayer regions show the standard increase in $A_{1g}$ to $E_{2g}^1$ Raman peak separation, from the monolayer $\Delta$ = ~19.2 $cm^{-1}$ to $\Delta$ = ~21.2 $cm^{-1}$ for bilayer. Additionally, increased Raman signal intensity (**Figure 3.4h**) from thicker material, and reduced PL intensity (**Figure 3.4g**) from the $MoS_2$ transition from direct (monolayer) to indirect (bilayer) bandgap, both indicate bilayer $MoS_2$ crystals in the same regions of this sample. Some flake edges are either fully or partially electrically isolated from one or both contact edges, which restricts charge carrier transport across the channel thus reducing the effective channel active area. One example of this is shown in location 3, where the low photocurrent in this region in **Figure 3.4b** can be partly explained by the discontinuity in the film across the channel, including non-coalesced small flakes that are isolated from the contacts. The locations with the best photocurrent are 1, 2 and 5. These locations show regions of strong PL within the flakes and near the contact edges (**Figure 3.4g**) and a blue shift in the PL peak (**Figure 3.4f**) within these better coalesced domains. The strong PL indicates high quality and purity in the $MoS_2$ crystal in these regions, resulting in longer carrier non-radiative recombination lifetime, and the blue-shifted PL peak position distribution within these domains infers less defects, tensile strain relaxation, and a higher carrier conductivity favorable for larger photogenerated current in the device. While location 4 had the largest

PL red shift, and the domain spans the entire channel length, it is accompanied by a low PL intensity which explains the relatively low photocurrent when comparing to locations 1, 2 and 5. With a S-D voltage bias of 1V, the maximum EQE of 0.254% (**Figure 3.4d**), and IQE of 5.821% (**Figure 3.4e**), were at location 5, which is also the largest area of strong uniform PL. The IQE is about one order of magnitude larger than the EQE.

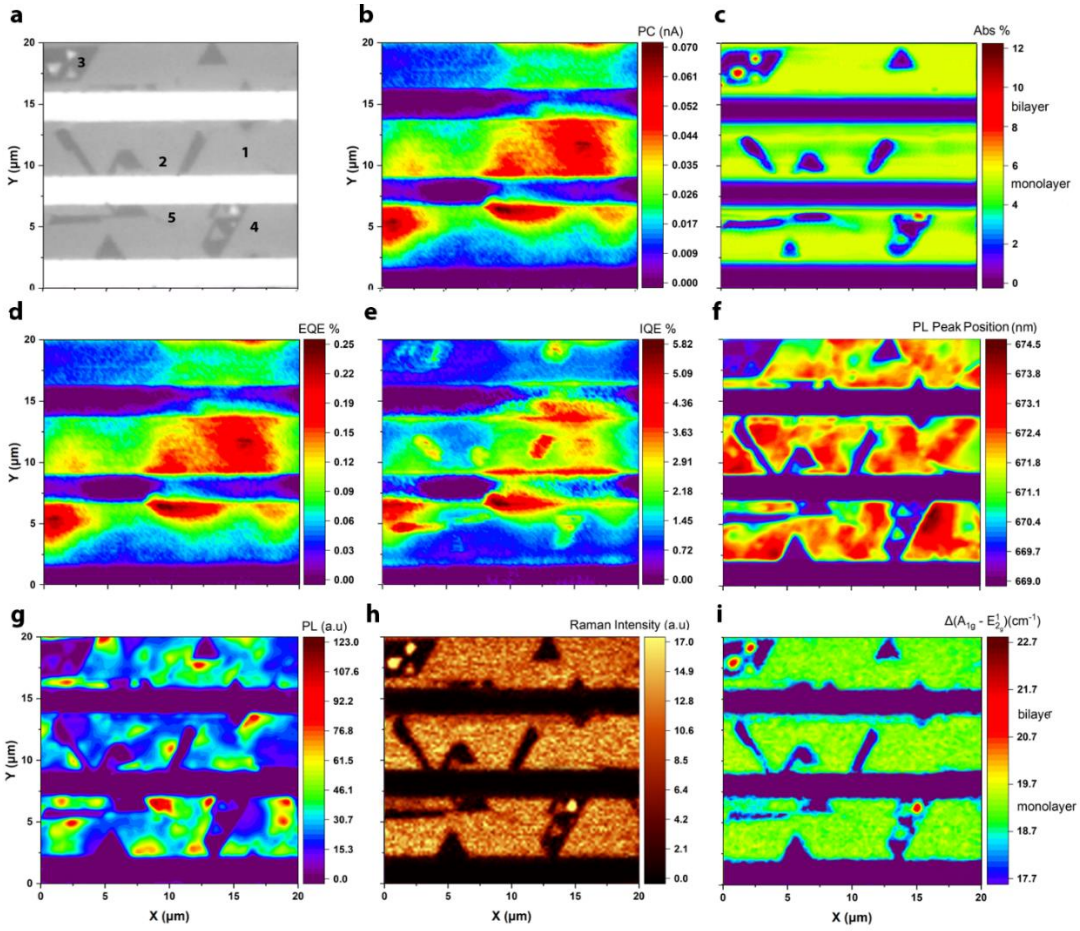


**Figure 3.4:** Spatial maps of $MoS_2$ flakes with phototransistor Ti contacts on top, all correlated to the same region: a) the optical image, b) photocurrent, c) absorption, d) EQE, e) IQE, f) PL peak wavelength, g) PL intensity, h) Raman $A_{1g}$ peak intensity, and i) Raman $A_{1g}$ to $E^1_{2g}$ peak separation.

### 3.2.2 Monolayer film mapping

Higher efficiency is expected for a 2D material film-based device with well-coalesced domains. A film grown using 1 mg $MoO_3$ and 12 minutes of sulfurization time, as shown in **Figure 3.2i**, was selected for the monolayer film sample correlative maps. The correlative maps for the uniform monolayer $MoS_2$ film-based phototransistor, with a maximum EQE of 0.374% and IQE of 10.15%, are shown in **Figure 3.5(d-e).** The optical image **(Figure 3.5a)** shows uniform $MoS_2$ over the 20 μm x 20 μm (400 $\mu m^2$) device area. Large area monolayer uniformity is confirmed by the consistent ~5% absorption of 660 nm incident light **(Figure 3.5c),** Raman intensity **(Figure 3.5h),** and monolayer $A_{1g}$ to $E^1_{2g}$ Raman peak separation of $\Delta$ = ~19.2 $cm^{-1}$ **(Figure 3.5i),** all mapped within the channels of the phototransistor. These maps show that both electrically isolated and multilayer regions do not exist in the film. This indicates that less film morphology defects are present to significantly affect the device performance as compared to the flake sample device. The photocurrent of greater than 0.07 nA was generated at all locations within the channel **(Figure 3.5b)** compared to the flake sample with less film coverage **(Figure 3.4b)**, where less than 10% of the device area produces a photocurrent greater than 0.07 nA. The maximum photocurrent in the film sample was 0.12 nA near the contact edges. Photothermoelectric effect is known to contribute to the total collected current,[70] and can be seen near some of the contact edges in the photocurrent map. While the domain boundaries cannot be easily identified in the optical image or the photocurrent, absorption, or Raman maps, the domain boundaries can clearly be seen in the map of PL peak position **(Figure 3.5f)**. Where the domains coalesce, there is a slight blue shift of the PL peak. The boundaries affect device efficiency through undesirable carrier recombination. The largest

photocurrent and IQE is mapped between the top and middle contacts. This upper channel contains a larger domain that correlates with uniform PL peak position; the upper channel also has less well-defined domain boundaries parallel to the contacts as compared to the lower channel, which also favors enhanced photocurrent. Even when the light was incident on the device contacts, photocurrent greater than 0.04 nA was collected from the photogenerated carriers resulting from the scattered light, indicating relatively good film quality.

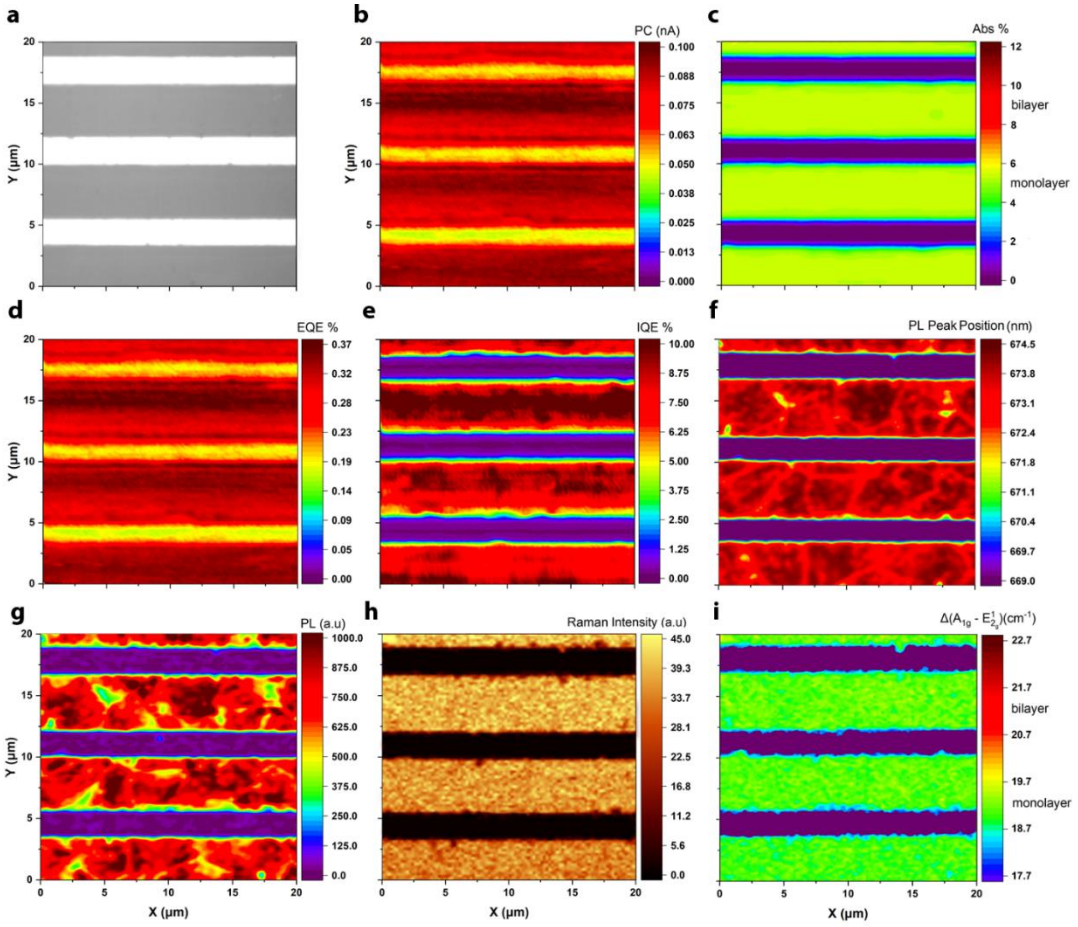


**Figure 3.5:** Spatial maps of a monolayer $MoS_2$ film with phototransistor Ti contacts on top, all correlated to the same region: a) the optical image, b) photocurrent, c) absorption, d) EQE, e) IQE, f) PL peak wavelength, g) PL intensity, h) Raman $A_{1g}$ peak intensity, and i) Raman $A_{1g}$ to $E^1_{2g}$ peak separation.

### 3.2.3 Film with bilayer islands mapping

The carrier mobility and photogenerated current within the channel is expected to increase with absorber thickness.[44], [77], [78] To show this, a device was fabricated using a continuous monolayer $MoS_2$ film with bilayer island growth in the active area. The $A_{1g}$ to $E^1_{2g}$ Raman peak difference in **Figure 3.6i** shows the bilayer regions in the film even at small sub-micron scale, with better resolution than any of the other mapping techniques. One of the bilayer islands between the contacts is shown at location 1 in the optical image in **Figure 3.6a**. The ~5% monolayer absorption and ~ 9% bilayer absorption of the 660 nm incident light clearly shows the number of layers in **Figure 3.6c** and correlates with the optical image. Additionally, the bilayer Raman shift of $\Delta$ = ~21.2 $cm^{-1}$, increased Raman intensity, and low PL all point to the bilayer islands at the same positions on the film, as seen in the respective spatial maps in **Figure 3.6**. The standard red shift in PL peak position from as-grown monolayer to bilayer is shown in **Figure 3.6f**, where the bilayer peak positions ($\lambda$) are greater than 673.7 nm (bandgap above 1.84 eV). The monolayer film PL peak is blue shifted in parts of the film near location 2, with a corresponding bandgap of ~1.85 eV. This blue shift again corresponds to strong PL in this location, indicative of higher electronic quality and relatively higher photocurrent than in nearby regions with red-shifted and reduced PL. Although the device has a fully coalesced monolayer film, the film generates non-uniform photocurrent as shown in **Figure 3.6b**. A likely explanation for the regions of enhanced photocurrent is increased absorption at the bilayer regions, clearly seen in the top and middle channels. Of the bilayer regions, the most efficient light to electricity conversion is at location 1, where the bilayer connects with the Ti contact. The IQE at location 1 is the highest of the bilayer regions (> 3.4%) compared to the other

bilayer IQE regions (< 3.34%) and is higher than parts of the monolayer film IQE. This indicates that high efficiency devices can be fabricated by increasing the number of $MoS_2$ film layers. The lower channel has the most uniform photocurrent over the mapped area. This corresponds to the region with strong PL that is most widely distributed across the mapped area, as compared to the other channels, indicating a region of monolayer film with lower defect density.

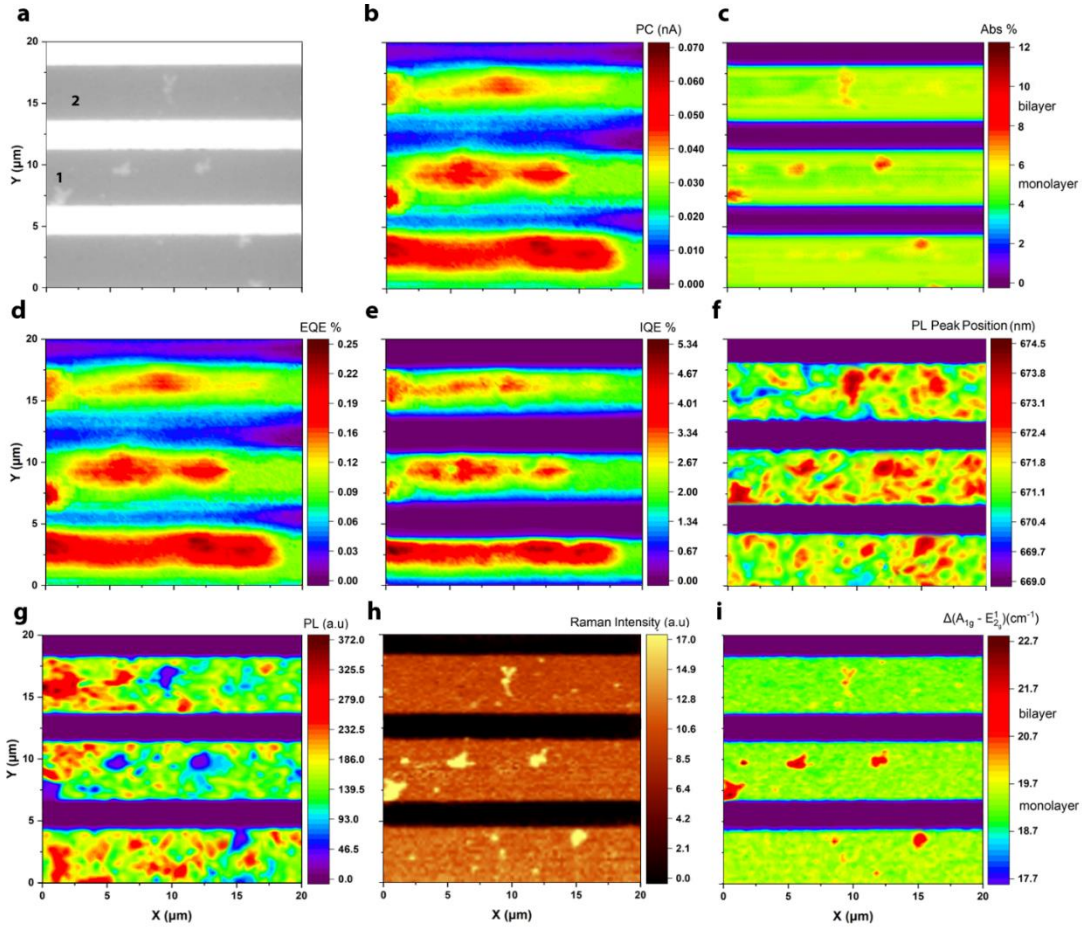


**Figure 3.6:** Spatial maps of a monolayer $MoS_2$ films with as-grown bilayer islands and phototransistor Ti contacts on top, all correlated to the same region: a) the optical image, b) photocurrent, c) absorption, d) EQE, e) IQE, f) PL peak wavelength, g) PL intensity, h) Raman $A_{1g}$ peak intensity, and i) Raman $A_{1g}$ to $E^1_{2g}$ peak separation.

### 3.2.4 Film with transferred second monolayer mapping

From the monolayer with as-grown bilayer island device performance, we know that increased absorption can lead to better phototransistor responsivity; therefore, multilayer uniform $MoS_2$ films can lead to higher efficiency devices. Several groups have explored direct synthesis of multilayer TMDC films;[79]–[82] however, it is still challenging to grow large area uniform multilayer films by CVD. Our approach to increase absorption is to use layer transfer to stack a uniform monolayer film onto a device fabricated on an as-grown monolayer film, resulting in a two monolayer $MoS_2$ film phototransistor. Two films grown using 1 mg $MoO_3$ and 12 minutes of sulfurization time, as shown in **Figure 3.2**, were selected for the device. More details on the transfer and device fabrication can be found in the Experimental Section. The optical image for a section of one device is shown in **Figure 3.7a**, where the difference in contrast clearly shows the contacts, monolayer $MoS_2$ region noted by 1, and the region with a second stacked monolayer $MoS_2$ film on top noted by 2. The lighter region to the left of the image has two $MoS_2$ layers (as-grown and transferred), and the darker region to the right has only the transferred monolayer film; the metal contacts are on top of the as-grown layer and underneath the transferred layer. The correlative maps are shown in **Figure 3.7**. The absorption map agrees with the optical image, where uniform ~ 5% and ~9% absorption was obtained for monolayer and two monolayer regions, respectively. The Raman intensity map shows uniformity in the transferred film over the mapped area, including at the Ti contacts since the film was transferred on top. Like the as-grown films with bilayer islands, the intensity increased for two stacked monolayers; however, the monolayer $A_{1g}$ to $E_{2g}^1$ Raman peak separation $\Delta$ = ~19.2 $cm^{-1}$ was maintained across both the single and double

monolayer regions, as seen in in **Figure 3.7i**, indicating that there was no structural transition from monolayer to bilayer $MoS_2$. A comparison of the Raman spectra for the as-grown and stacked monolayer films is shown in **Figure C.3**, (Appendix C).

Since the $MoS_2$ CVD synthesis on C-plane $Al_2O_3$ is quazi-epitaxial,[47] and the lattices are not perfectly matched, some lattice strain is expected. The PL peak position map **(Figure 3.7f)** shows a blue shift in the transferred monolayer film PL, unlike the standard red shift for bilayer $MoS_2$, as seen in **Figure 3.6f**. The map shows an average increase in bandgap of ~ 0.011 eV and an even further bandgap increase of ~ 0.02 eV at some regions on the Ti contact. We attribute this shift to strain relaxation, along with film and contact interface effects. Unlike in conventional bilayer $MoS_2$ films, where PL decreases due to a transition to an indirect bandgap,[74] the PL intensity is roughly tripled in the stacked monolayer region relative to the single monolayer region, as seen in **Figure 3.7g**. A PL decrease approaching as much as 14% in some locations is seen for the parts of the transferred film that are directly on the Ti contacts due to PL quenching. A comparison of the PL spectra for the stacked monolayer and for a single film pre and post transfer is shown in **Figure C.5**, (Appendix C).

The average photocurrent in the channels for the monolayer transferred film is ~0.09 nA, while the stacked monolayer regions have an average photocurrent of ~0.11 nA, with photocurrent approaching 0.15 nA in several locations. The thicker absorber created by stacking a second film produces more photocurrent than the monolayer region, with a maximum EQE of 0.54%, which is more than the maximum as-grown bilayer EQE of 0.25% in **Figure 3.6d**. An IQE ranging from 3.7% to 5.1% is shown in **Figure 3.7e** for the

stacked layers, which like the as-grown bilayer, is lower than the monolayer IQE, which is 6.3% on average in **Figure 3.7e.**

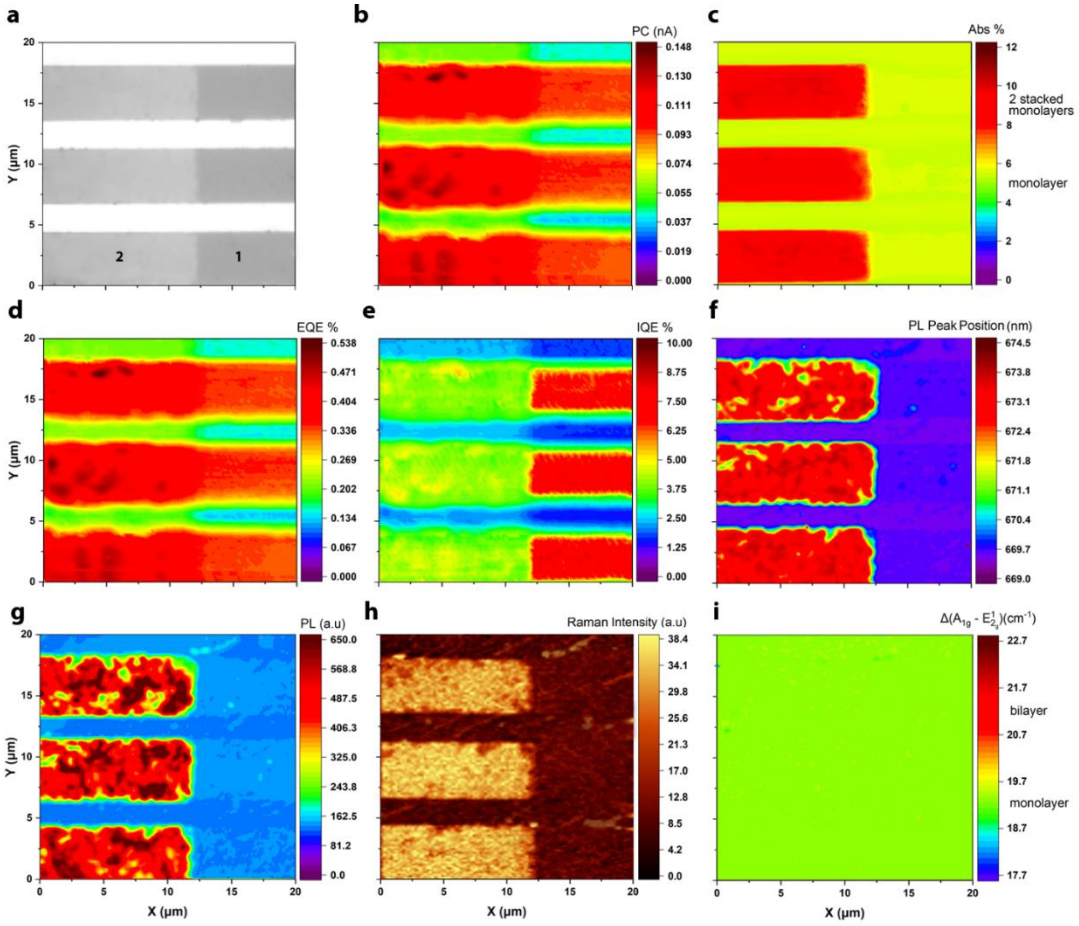


**Figure 3.7:** Spatial maps of (left) monolayer $MoS_2$ film with Ti contacts on top and a transferred monolayer $MoS_2$ film stacked on top of that and (right) just a monolayer $MoS_2$ film transferred onto Ti contacts, showing correlation between each: a) the optical image, b) photocurrent, c) absorption, d) EQE, e) IQE, f) PL peak wavelength, g) PL intensity, h) Raman $A_{1g}$ peak intensity, and i) Raman $A_{1g}$ to $E^1_{2g}$ peak separation.

While each of these 2D $MoS_2$ film morphologies show different features, consistent trends appear for the mapped properties. Tracking PL peak shifts is one of the less obvious trends. For the as-grown $MoS_2$ films, compressive strain in the monolayer

crystal lattice due to the quasi-epitaxial growth on sapphire substrates affects the film quality and the efficiency of the devices **(see Figure C.5, Appendix C)**. Across multiple morphologies with intentionally grown lower quality films, a stronger PL correlates with a blue shift in the PL peak. We attributed this shift to localized strain relaxation in regions with reduced defect density. This infers that parts of the monolayer film and flakes with lower crystalline order have a more difficult time relaxing into unstrained configurations from the as-grown position. The higher quality regions with blue-shifted PL are associated with enhanced photocurrent, especially when adjacent to other relatively low defect regions. A different trend is seen for the high quality well coalesced monolayer as-grown films, where PL peak position is relatively uniform, and a small blue shift is observed only at the grain boundaries.

### 3.3 Back-gated Phototransistor Analysis

As an example of another useful device type from these materials, the electrical characteristics of a back-gated phototransistor from the $MoS_2$ monolayer film, grown using 1 mg $MoO_3$ and 12 minutes of sulfurization time as seen in **Figure 3.2i,** are shown in **Figure 3.8**. Titanium contacts in a grid pattern are fabricated on a $SiO_2$ (300 nm) on Si substrate, and the $MoS_2$ film is transferred on top of these contacts, as shown schematically in **Figure 3.8a**. The transistor response was modulated with different incident light power at an excitation wavelength of 670 nm. With a source-drain voltage bias of $V_{SD}$ = 2 V, light-enhanced source-drain current $I_{SD}$ is seen at incident optical power as low as 8 nW, with further enhancement up to 25.2 μW, where the $I_{SD}$ reached 9 μA, which is 3 orders of magnitude larger than the dark current as shown in **Figure 3.8b**. Back-gate tunability was also obtained for the phototransistor, as shown in **Figure 3.8c,** where increased $I_{SD}$ is shown

for higher gate voltages at a source-drain bias $V_{SD}$ = 2V. The gate bias $V_G$ at which the transistor switches from the OFF to ON state is reduced as the incident light power is increased. At gate bias $V_G$ = 55 V, a photocurrent of 60.4 μA, was obtained at incident power of 8 nW. The photocurrent and photoresponsivity as a function of incident light power are shown in **Figure 3.8d**. The expected decrease in responsivity as the incident optical power and corresponding photocurrent is increased due to increased electron-trap saturation, photo-excited carrier recombination, and Auger recombination.

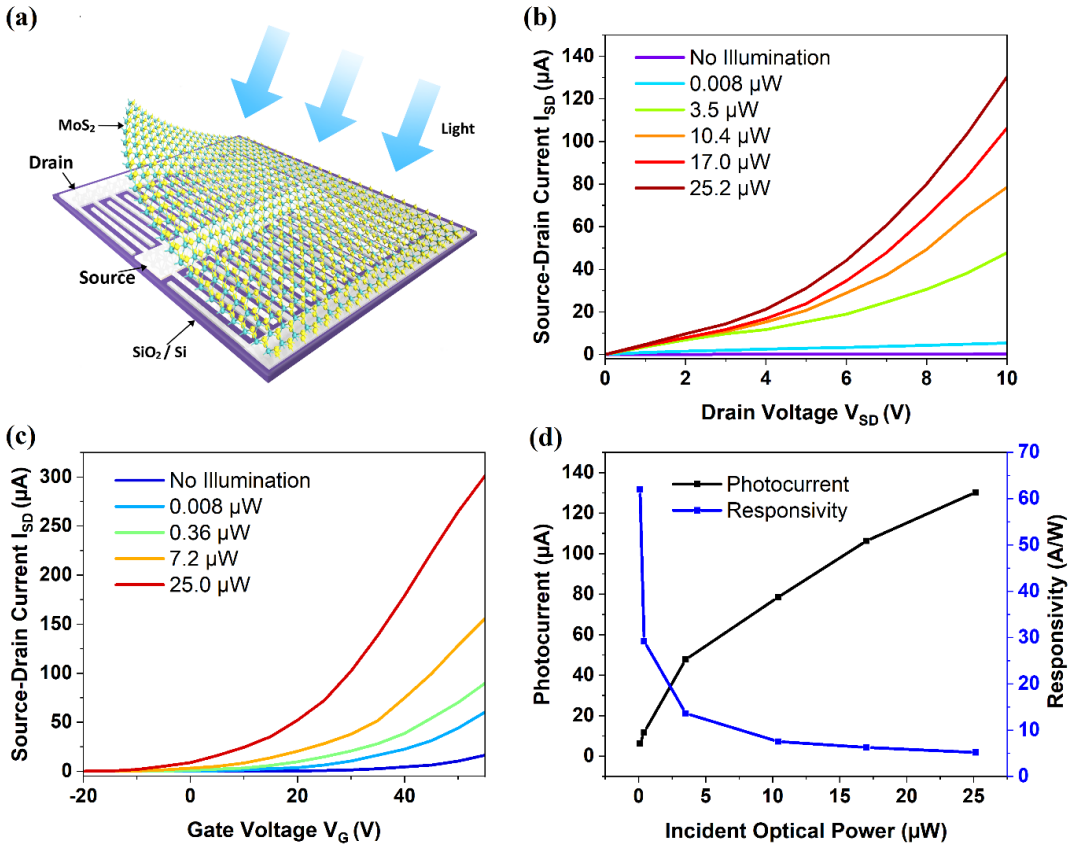


**Figure 3.8:** (a) Schematic of a phototransistor with monolayer $MoS_2$ film transferred on top of Ti contacts. (b) Drain current ($I_D$) as a function of source-drain voltage ($V_{DS}$) for an excitation wavelength of 670 nm at different illumination power and gate bias $V_G$ = 0 V. (c) Drain current as a function of gate voltage under different illumination power and source-drain bias $V_{SD}$ = 2 V. (d) The dependence of photocurrent and responsivity on incident optical power is shown.

## 3.4 Experimental Section

### 3.4.1 Synthesis of $MoS_2$ films

$MoS_2$ films of up to 1 $cm^2$ were grown using an MTI OTF-1200X-II dual zone split tube furnace. A third low-temperature zone was introduced by wrapping the quartz tube with a Grainger SLR series silicone heating blanket. ACS reagent ≥ 99.5% molybdenum (VI) oxide ($MoO_3$) powder and 99.98% trace metals basis sulfur (S) powder from Sigma-Aldrich were used as precursors for the CVD synthesis. A 1-inch diameter quartz tube was placed in the three-zone furnace where zones 1, 2 and 3 were the upstream (heating blanket), middle, and downstream zones respectively. A C-plane sapphire substrate was placed on top of an alumina boat, and the $MoO_3$ powder was positioned in the boat 1.5 cm upstream from the center of the substrate. The amount of sulfur is a critical parameter in the formation of oxy-particles of $MoO_3$ (or $MoO_2$) throughout the films.[83] For the range of $MoO_3$ precursors used, 230 mg of sulfur was used and resulted in no oxy-phases in the films, as shown in the Raman spectra in **Figure C.6**, (Appendix C). The boat with the $MoO_3$ powder and sapphire substrate was centered in zone 2, and sulfur powder was placed in an alumina boat in zone 1, 30 cm upstream from the $MoO_3$ powder. The tube was initially vacuumed down to a pressure of 15 mTorr, then ultrahigh-purity argon (Ar) was used as the carrier gas at a flow rate of 180 sccm, with the tube pressure maintained at 2.4 Torr. The temperatures of the second and third zones of the furnace were set to 750 °C with a 50-minute ramp time. At the end of the ramp, zone 1 was heated up to 120°C and zones 2 and 3 were held at 750°C throughout the duration of the growth. The growth time, for the purposes of optimization and repeatability (see **Figure 2.2**) as discussed in Chapter 2, begins when zone 1 reaches 750 °C. More growth details and schematics are reported in

our previous work.[55] The $MoO_3$ precursor supply of 0.5, 1.0, 3.0 and 5.0 mg were used for sulfurization times of 8, 10 and 12 minutes. The PL results for these films are shown in **Figure C.7**, (Appendix C). Uniform monolayer films, monolayer films with bilayer growth, films of fully and partially coalesced flakes, and flakes with bi-layer growth were chosen for the $MoS_2$ phototransistors. To assess the stability of these 2D films, we measure PL on a uniform monolayer film, grown using 1 mg $MoO_3$ and 12 minutes of sulfurization time as seen in **Figure 2.2i,** directly after growth and six months after growth (stored in a nitrogen environment at room temperature), showing no notable degradation (see **Figure C.8** in Appendix C).

### 3.4.2 Device Fabrication and Film Transfer

To fabricate the phototransistors, 200 nm of 495 A4 PMMA resist, followed by 400 nm of 950 C4 PMMA resist, both from Kayaku Advanced Materials, were spin coated on the as-grown $MoS_2$ on $Al_2O_3$ substrates. A thin chromium layer was used for charge dissipation. The contacts were patterned using a RAITH VOYAGER 100 electron beam lithography (EBL) tool, and 50 nm Ti was deposited at a rate of 0.5 Å/s using an Angstrom Engineering Nexdep electron beam evaporation tool. The complete steps are shown schematically in **Figure C.9a**, (Appendix C);. To fabricate the monolayer plus stacked monolayer phototransistor, a second EBL step and development is done to expose part of the as-grown $MoS_2$ film in the device active area. Chromium etchant from Sigma-Aldrich was used to etch away the exposed $MoS_2$ and the remaining resist was dissolved with acetone creating a clean monolayer film to no film step edge. After a solvent (acetone and IPA) clean, the surface-energy-assisted film transfer process,[49] was used to transfer a second monolayer $MoS_2$ film from an $Al_2O_3$ substrate onto the phototransistor. The

fabrication steps for this second device type are added shown schematically in **Figure C.9b**, (Appendix C). The device was then annealed at 200 °C for 2 hrs.

### 3.4.3 Analysis of film strain

Since the $MoS_2$ CVD synthesis on C-plane $Al_2O_3$ results in strain in the $MoS_2$ lattice, the strain is expected to relax when the film is transferred onto other substrates or device contacts. The $A_{1g}$ to $E^1_{2g}$ Raman peak separation does not clearly indicate any difference in strain for the as-grown $MoS_2$ on sapphire, $MoS_2$ transferred onto the titanium contacts, $MoS_2$ transferred onto sapphire, and $MoS_2$ transferred onto as-grown $MoS_2$, as shown in **Figures C.4a** and **C.4b**, (Appendix C). However, strain relaxation from as-grown to transferred films is evident in the difference in Raman intensity ratio I($A_{1g}$)/I($E^1_{2g}$) as shown in **Figure C.4c**, (Appendix C); these trends indicate that the as-grown films are compressively strained.[84] The as-grown $MoS_2$ compressive strain is more relaxed when transferred onto the titanium contact than onto the sapphire substrate.

### 3.4.4 Producing the spatial maps

The Raman and PL spectroscopy measurements and maps were generated using a WITec alpha300 Ri inverted Raman imaging confocal microscope and the analysis was carried out using WITec Suite FIVE data acquisition and analysis software. The Raman system's 532 nm excitation laser line was used to make the measurements in ambient air environment, and the laser power was kept at 1.5 mW to avoid thermal effects in the film during scans. The emission collection objective was a 100 x Nikon TU Plan Fluor EPI with a numerical aperture of 0.9. A ~ 300 nm spot size and stage step size of 200 nm was used for the area scans with an integration time of 0.02 s for PL and 1 s for Raman. The PL measurements were taken using a 300 g/mm grating with a 750 nm blaze wavelength. The

Raman measurements were done using a 600 g/mm grating with a 500 nm blaze wavelength.

The photocurrent and absorption maps were obtained with a single scan where photocurrent and transmission were measured simultaneously. An MLS203-2 fast XY scanning stage from Thorlabs was used to raster a ~ 0.3 μm beam width, 660 nm laser over a 20 x 20 μm scan area, with a 0.2 μm step size. The light source was a supercontinuum laser, coupled to a laser line tunable filter, both from Fianium/NKT Photonics. For photocurrent maps, the $MoS_2$ phototransistor contacts were probed using XYZ 300 micro positioners from Quater Research & Development. A source-drain bias of 1 V was applied and the transistor photogenerated current was measured using a Keithley 2450 sourcemeter; the dark current under 1 V bias was subtracted. The optical transmission through the film was measured using a Thorlabs FDS1010-CAL calibrated photodiode (CPD), mounted 1 mm below the sample, for both the 100% reference ($Al_2O_3$ substrate) and sample ($MoS_2$ + $Al_2O_3$ substrate) transmission measurements. All the components in the measurement setup were integrated with a LabVIEW virtual interface for data collection. The absorption was calculated from the transmittance and reflectance. For 660 nm incident light, monolayer $MoS_2$ has a reflectance of 0.048%, and bilayer reflectance is 0.096%.[85]–[88] This calculation cannot be applied at regions within the mapped area where the laser spot is the device contacts, where a reflectance of ~100% and transmittance of 0% is expected. The average monolayer absorption was used in the two-stacked monolayer devices at the regions with $MoS_2$ monolayer film directly on top of the Ti contacts.

### 3.4.5 Statistical Analysis

Synthesis of $MoS_2$ films: Growth parameters for all 12 film morphologies shown in Fig. 1 were used to show reproducibility over at least three statistically independent samples. Each sample's optical, electronic, and structural properties were characterized at nine locations (the center of each square of a 3 x 3 grid defined over the entire growth substrate) to assess film quality by transmission, photoluminescence, and Raman spectroscopy.

For the photocurrent measurements, a dark measurement was taken for baseline correction to account for detector noise and was subtracted from the final measurement as discussed in the experimental section on the spatial map production. A dark measurement was also taken and subtracted from the measurement obtained for the transmission maps.

Spatial Mapping: Spatial maps were produced over a 20 μm x 20 μm (400 $\mu m^2$) area with a 200 nm step size to obtain 10,000 sample points per map. Hyperspectral PL and Raman spectroscopy were used to obtain 10,000 spectra for all PL peak position, PL peak intensity, Raman peak intensity, and Raman $A_{1g}$ to $E_{2g}^1$ peak separation. Raman $A_{1g}$ to $E_{2g}^1$ peak positions, separation, and intensity ratio I($A_{1g}$)/I($E_{2g}^1$) are represented with mean ± standard deviation for nine measurements. The one sample *t* test was used for statistical analysis of the Raman peak intensity ratio I($A_{1g}$)/I($E_{2g}^1$) to show that the $MoS_2$ transferred on as-grown $MoS_2$, $MoS_2$ transferred on sapphire, and $MoS_2$ transferred on titanium samples were significantly different from the as-grown $MoS_2$ prior to transfer, in order to assess strain relaxation. Significance was defined as $p < 0.001$. Origin 2021b software by OriginLab Corporation was used for statistical analysis.

## 3.5 Conclusions

In summary, we demonstrated the synthesis of large-area, high-quality $MoS_2$ films with different film morphologies and domain sizes up to 30 μm by quazi-epitaxial growth on $Al_2O_3$ substrates using the CVD process. The work gives insight into the film growth mechanism under various conditions, which can be used to optimize film quality towards high quality, large area, and highly uniform films for use in efficient devices. Furthermore, we used high resolution correlative spatial mapping to reveal the connection between the optical, electronic, and structural properties of these 2D $MoS_2$ morphologies in the context of their use in a phototransistor device. The PL peak position mapping revealed domain boundaries more clearly in the monolayer film, while the $A_{1g}$ to $E_{2g}^1$ Raman peak difference showed the bilayer regions with better resolution than any of the other mapping techniques employed in mapping the multilayer as-grown films. Correlating the PL maps with photocurrent maps, we showed that strain relaxation led to stronger PL and enhanced photocurrent. Furthermore, by stacking two monolayer films, we showed that a maximum EQE of 0.29%, more than the maximum as-grown bilayer EQE, was achieved. This analysis can be employed in the development and characterization of a range of 2D based materials and devices. This approach will aid the ongoing pursuit of high-efficiency, lightweight, flexible, and wearable electronics, optoelectronics, and photovoltaics from 2D materials.

## 3.6 Future Directions

While we have demonstrated the synthesis of large-area, high-quality monolayer $MoS_2$ films using the CVD process and showed the relationship between the optical, electronic, and structural properties of these 2D $MoS_2$ films through high resolution

correlative spatial mapping, we need to explore how these properties change as we stack multiple monolayers beyond 2 films for photovoltaic applications. We can expect an increase in photoresponsivity in the phototransistor device and increased optical absorption in the film, but a more quantitative analysis and establishment of trends can be revealed through correlative mapping of the stack. A systematic characterization of how the PL peak position and the $A_{1g}$ to $E^1_{2g}$ Raman peak difference changes with stacking can lead to a better understanding of the performance of devices made using stacked monolayer $MoS_2$ films. Therefore, future steps will include the fabrication of phototransistors with stacked monolayers beyond 2 monolayers, the correlative mapping of the Raman, photoluminescence, and absorption of the stack and the device performance characterization as a function of the number of stacked monolayers.

There are external conditions that can change or dynamically tune the properties of the synthesized 2D $MoS_2$ films. Some of these conditions include temperature, magnetic field, and electric field. Spatial characterization using the correlative mapping explored in this work as a function of these external conditions can open a whole new dimension of understanding of the CVD synthesized 2D TMDCs. This can also lead to the improvement and development of 2D based optoelectronic and photovoltaic devices for current and new applications. Therefore, the future efforts in this work will involve the characterization of the $MoS_2$ films and phototransistors using correlative mapping under in the presence of a magnetic field, electric field and under different temperature profiles for monolayer and stacked monolayer $MoS_2$ films.

# CHAPTER 4

# HIGH-SPECIFIC POWER FLEXIBLE PHOTOVOLTAICS FROM LARGE-AREA $MoS_2$ FOR SPACE APPLICATIONS

Industries and researchers are continuously searching for semiconducting materials suitable for lightweight, high-specific-power photovoltaics (PV). In recent years, thin-film PV technology using materials such as cadmium telluride (CdTe), copper indium gallium diselenide (CIGS) and three-dimensional (3D) perovskites have shown some promise; however, silicon (Si) solar cells continue to be the go-to material for many applications due to the abundance of Si on earth compared to other materials, the low-cost manufacturing, scalability, and good power conversion efficiency (PCE). The high PCE requires relatively thick absorbers and is now close to its fundamental limit. [89]–[91] Future space missions will depend largely on PV to power the various systems; therefore, significant research is geared towards the development of materials and systems for space-based PV. The ideal space PV requires several properties, including high PCE, ultra-thin form factor for light weight and reduced launch costs, flexibility for ease of stowage, and resistance to radiation-induced degradation that can arise from exposure to high energy particles in space (preserving performance and minimizing the need for weighty protective layers). [92] However, the robustness and optical absorption of Si is reduced at ultrathin thicknesses. Furthermore, Si solar cell performance degrades significantly when exposed to high energy protons and electrons [93], [94], which reduces power system lifetime in missions where high radiation exposure is expected.

Thin-film PV has progressed over the years as a potential solution for space PV with good scalability. Recently, thin-film solar cells with efficiencies > 20 % at absorber thicknesses less than 5 μm have been made using conventional semiconductors such as III-V materials and CdTe [95]–[97]. However, cell fabrication cost has not been significantly reduced compared to Si cells and would require further reduction in thickness to compete with Si prices. Furthermore, like Si, additional thinning is accompanied by reduced absorption, mechanical strength, and efficiency, unless absorption enhancements, buffer layers to suppress recombination, and structural support are added back, [96], [97] all of which increase the mass and/or cost of the deployed module. Another emerging thin-film photovoltaic technology, perovskite solar modules, can attain PCEs up to 21.1%, with the lowest reported absorber layer film thicknesses in the 100 nm to 1 μm range and potential for high power density in module form. However, their considerable degradation risk, due to environmental conditions such as high humidity, temperature, and ultraviolet radiation exposure that promotes photocatalysis of metal oxides in the perovskites, makes them vulnerable to significant performance loss prior to space launch and requires more robust module packaging, which affects power density.[98]–[102]

Alongside the development of conventional semiconductors, emerging materials such as transition metal dichalcogenides (TMDCs) are being considered for thin film PV, particularly as a suitable option for high-specific-power, flexible, radiation resistant single and multi-junction solar cells. [62], [74], [103]–[105] Additionally, 2D TMDCs are predicted to achieve solar absorption an order of magnitude higher per unit thickness than GaAs and Si in the visible spectrum, and one to three orders of magnitude higher specific power than existing ultrathin solar cells. [46], [106] A 1 nm thick $MoS_2$ solar cell can

exhibit an order of magnitude higher specific power than a 1 μm thick GaAs solar cell [46] and at PCEs of 9.22%, < 4 nm thick $MoS_2$-based solar cells are projected to have a specific power values of > 100 $Wg^{-1}$ under one-sun (AM 1.5) illumination. [107] TMDCs exhibit a wide range of band gaps (~1.0–2.5 eV), [108] and the active layers are typically sub-micron, which is a significant improvement over conventional semiconductors in terms of specific power and weight. Furthermore, they are free of dangling bonds at the surface, eliminating the need for lattice matching when designing heterostructures.

The flexibility of TMDCs makes them ideal for ease of PV stowage for space deployment, and their strong in-plane covalent bonds make them relatively mechanically robust for their thickness. In one study, $MoS_2$ sheets were bent down to a radius of curvature of 0.34 nm before bond breaking was observed, [109] showing promise towards easy deployment in space by furling and unfurling 2D $MoS_2$ based PV.

Due to the atomically thin nature of TMDCs, they possess exceptional radiation tolerance suitable for space applications. In one study, 2D $MoS_2$ FETs maintained a high currents and on/off ratios while being exposed to $He^{2+}$ fluence of $10^{15}$ ions/$cm^2$ or proton fluence of $1.26 \times 10^{16}$ ions/$cm^2$ , corresponding to thousands of years of proton and alpha particle irradiation in space. [38] $WS_2$ devices were exposed to γ-radiation of fluence $18.41 \times 10^9$ $cm^{-2}$ $sr^{-1}$ $MeV^{-1}$ and had increased photoluminescence (PL) and carrier lifetime that was attributed to decreased defect densities, [40], [110] highlighting the radiation hardness benefit of 2D PV.

Work has been done to demonstrate large-area 2D PV and incorporate various techniques to improve PCE, [62], [111]–[113]. Projections show that a $V_{OC}$ of up to ~1.2

V and a FF up to ~81% can be obtained for an $MoS_2$ solar cell, [107], [114] while a $J_{SC}$ of 13.4 mA/cm$^2$ under one-sun (AM 1.5) illumination has already been demonstrated. [115] Separately, integration of very small-area high-PCE 2D PV on flexible substrates has been shown. [116] The PCE of TMDC solar cells is generally affected by strong Fermi-level pinning at the metal contact–TMDC interface and doping limitations, which have been addressed by the insertion of an ultrathin graphene interlayer at the metal–TMDC interface, a $MoO_x$ capping layer for doping and passivation, and an anti-reflective coating, all on a 5 μm, flexible polyimide substrate; this work achieved a PCE of 5.1% and a specific power of 4.4 Wg$^{-1}$. [117] However, the scalability of 2D PV to large-area devices incorporating flexible substrates has not yet been demonstrated and is necessary to demonstrate their promise for applications in space.

In this chapter, we demonstrate the design and fabrication of scalable, large-area CVD-grown monolayer $MoS_2$-based flexible PV devices on 3 μm polyimide films, which are subsequently encapsulated with a 1.6 μm thick polyimide layer. The device structure features a lateral Schottky-junction with interdigitated, asymmetric-work function Pt and Ti contacts. This chapter reports on PV performance, bending compatibility, and radiation resistance of the solar cells and provides model projections for cells with a thicker $MoS_2$ absorber. We also present the design and techno-economic analysis for the implementation of this 2D PV in a solar array on a 6U CubeSat, highlighting some of the benefits of 2D PV in space applications.

## 4.1 Module Design and Fabrication

Current cell technology such as CIGS, inverted metamorphic multijunction (IMM) III-V, and passivated emitter and rear contact (PERC) Si cells limit the active region minimum thickness to the 10 - 100 micron range, with module thickness of 10 to 50 mm. [118]–[120] However, ultrathin high-specific-power 2D material-based solar cells can reduce active region thickness to < 150 nm, with module thickness less than 10 microns, thus reducing the weight and volume per generated watt. There have been considerable efforts to demonstrate p-n junction and Schottky junction high-specific-power thin film PV both computationally and experimentally using single and few layer exfoliated 2D materials. [108], [116], [121]–[123] Previous reports have also demonstrated large-area chemical vapor deposition (CVD) synthesis of lateral Schottky-junction 2D $MoS_2$-based PV using Ti and Pt for contact asymmetry. [62] This work builds on the latter, scalable approach. The high work function ($\Phi_h$) contact Pt, is hole selective with the metal Fermi level closely aligned with the $MoS_2$ valence band, whereas the low work function ($\Phi_e$) contact Ti, is electron selective with the metal Fermi level closely aligned with the $MoS_2$ conduction band. The asymmetric metal-$MoS_2$-metal interface band structure forms a large Schottky barrier at the Pt-$MoS_2$ junction while an ohmic contact is formed at the Ti-$MoS_2$ junction, enabling carrier separation. Device model projections showed that with $\Phi_h$ as 5.65 eV, $\Phi_{MoS2}$ as 4.72 eV and $\Phi_e$ as 4.33 eV, 69.9 kW/kg (cell active area specific power only) is attainable with a 0.65 nm thick monolayer $MoS_2$ film. The energy band diagram schematic for the device architecture is shown in **Figure 4.1a**.

To further optimize the aforementioned solar cell architecture for space applications, the cells were directly fabricated on a strong, flexible, tear-resistant colorless polyimide

(CP1) substrate produced by NeXolve. [124] With a density of 1.54 g/cm$^3$, a 3 μm thick substrate and 1.6 μm encapsulant using the same polyimide adds just 7.08 x $10^{-4}$ g/cm$^2$ to the mass of the solar cell. The lateral PV cells were fabricated with a monolayer $MoS_2$ (0.65 nm) absorber layer as shown schematically in **Figure 4.1b**. The back interdigitated contact design was patterned on the polyimide substrate using electron beam lithography, and Ti and Pt contacts were deposited on the substrate in successive fabrication steps by electron beam evaporation. A 1.6 μm thick film of NeXolve's CP1™ Polyimide liquid resin in diglyme with viscosity of 2500 cP ±250 cP, was spin-coated onto the as-grown $MoS_2$ film on its sapphire growth substrate for the transfer support film and encapsulant. A surface-energy-assisted film transfer process, [49] was used to transfer the monolayer $MoS_2$ film, with encapsulant layer, from the sapphire growth substrate onto the interdigitated device contacts and polyimide substrate. The fabrication steps for the device are detailed in the Supporting Information and shown schematically in **Figure D.1** (Appendix D). By fabricating solar cells on the flexible polyimide substrate up to 10s of mm$^2$ of active area, as compared to the 10s of μm$^2$ active area from exfoliated 2D TMDC-based PV, we demonstrate the scalability of the 2D PV device fabrication process in this work. A photograph of large-area 2D solar cells with 25 mm$^2$ active area on the flexible polyimide substrate are shown in **Figure 4.1c**.

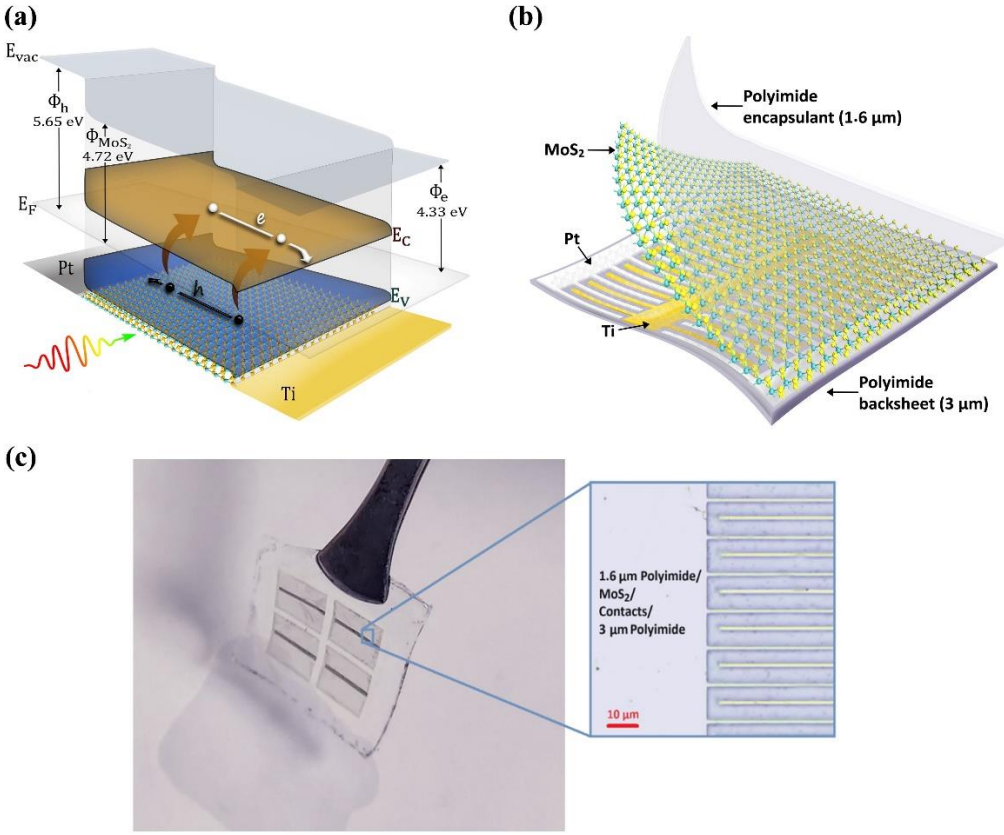


**Figure 4.1:** a) Bandstructure of a Ti−$MoS_2$−Pt Schottky-junction solar cell showing the band bending at the metal-semiconductor interfaces. b) Schematic of a Schottky-junction PV device with asymmetric interdigitated contacts and monolayer $MoS_2$ on polyimide substrate with polyimide encapsulation. c) Optical image of large-area (25 $mm^2$) ultra-thin and flexible 2D PV devices with a 5 µm channel length.

## 4.2 Optical Characterization and Modeling

The absorption spectra of the polyimide layers, the $MoS_2$ layer, and the $MoS_2$ polyimide stack of the solar cell were measured and modeled to characterize the absorption of each layer. The absorption spectra for the $MoS_2$ monolayer (0.65 nm), polyimide substrate ($PI_{subs}$), polyimide encapsulant ($PI_{encaps}$), and the stack after an $MoS_2$ monolayer was transferred onto the polyimide substrate and encapsulated ($PI_{encaps}/MoS_2/PI_{subs}$) are shown in **Figure 4.2(a)**. The transfer matrix method (TMM) was used to model the optical

absorption of the cell and the absorption of its individual layers. [125] The absorption spectra between 400 and 800 nm wavelength range are plotted to include the absorption in the visible range below the bandgap ~1.88 eV, clearly showing the modeled A, B and C peaks of monolayer $MoS_2$ at 652, 606 and 419 nm respectively. The n and k data reported by Islam et al. was used to simulate the $MoS_2$ monolayer absorption, [55] while the CP1™ Polyimide n and k data was obtained from NeXolve. The simulated monolayer $MoS_2$ peak locations are blue shifted relative to the peak locations of the experimentally measured $MoS_2$ film. This is because the experimental absorption is measured for as-grown monolayer $MoS_2$ on sapphire, while the n and k data used in the simulation are from variable angle spectroscopic ellipsometry (VASE) measurements of transferred monolayer $MoS_2$ on an $SiO_2$-on-Si substrate. Compressive strain relaxation of the $MoS_2$ lattice is expected when the as grown $MoS_2$ is transferred, [126] however, there is no $MoS_2$ strain relaxation in the $PI_{encaps}/MoS_2/PI_{subs}$ stack since the $MoS_2$ lattice strain is maintained by the polyimide encapsulant, which is applied prior to the transfer step. The absorption measurements and simulations match closely both in spectra and relative absorption percentages for the three cases.

Most of the absorption in the $PI_{encaps}/MoS_2/PI_{subs}$ stack results from the $MoS_2$ monolayer layer absorption, where the 0.65 nm thick absorber exhibits as high as ~17% absorption at 430 nm, and ~9% total absorption in the 400–800 nm wavelength range. Early experimental evidence, as shown in **Figure D.2** (Appendix D), indicates that stacking monolayers of $MoS_2$ via surface-energy-assisted film transfer results in additive absorption increases, rather than seeing a transition to indirect bandgap $MoS_2$. Based on this trend, we use TMM to calculate the absorption in a varying thickness stacked $MoS_2$ absorber layer

for a stand-alone $MoS_2$ film, $MoS_2/PI_{subs}$ stack, and $PI_{encaps}/MoS_2/PI_{subs}$ stack. We show that increasing the $MoS_2$ thickness increases the absorption in the 400–800 nm wavelength range shown in **Figure D.3a** (Appendix D). The total absorption is shown in **Figure 4.2(b)**. In the stand-alone $MoS_2$ absorber, a significant increase in absorption is seen from 0.65 to 3.25 nm (1 to 5 layers) and a less pronounced increase up to 11 nm. A slight decrease in absorption is shown from 11 to 28 nm thickness, due to interference effects in the stack, followed by a steady increase up to 68 nm before leveling off at thicknesses above 94 nm. Similar absorption trends are shown for the $MoS_2/PI_{subs}$ and $PI_{encaps}/MoS_2/PI_{subs}$ stacks, except that while the increase in the 1-to-5-layer thickness range is less dramatic, no decrease in absorption is shown in the $PI_{encaps}/MoS_2/PI_{subs}$ stack as the thickness increases. The short-circuit current density ($J_{SC}$) from the $MoS_2$ absorber in the $PI_{encaps}/MoS_2/PI_{subs}$ stack, as a function of $MoS_2$ thickness, was calculated by integrating the absorption with the AM0 one-sun extraterrestrial photon flux over the 280–800 nm range, assuming unity internal quantum efficiency (IQE). The $J_{SC}$ increases with $MoS_2$ thickness as shown in **Figure 4.2(b**), showing that stacking monolayers will lead to a significant increase in absorption and $J_{SC}$ of the $MoS_2$ solar cells. A maximum $J_{SC}$ of 17.71 $mA/cm^2$ was calculated using the 280-800 nm simulated absorption spectrum for a 100.1 nm (154 layer) $MoS_2$ absorber.

The encapsulant absorption is minimal in the 400-800 nm range with ~5% absorption at 400 nm which quickly decreases to ~0% at around 475 nm. The effect of the $PI_{encaps}$ thickness on the absorption of an $MoS_2$ monolayer in the 400–800 nm range is shown in **Figure D.3b** (Appendix D) and for a 100.1 nm (154 layers) stacked $MoS_2$ absorber in **Figure 4.2(c)**. While the thin film interference from $PI_{encaps}$ significantly

changes the wavelength-dependent absorption of a monolayer $MoS_2$, altering the thickness of the polyimide encapsulant up to 500 nm results in negligible changes in the total absorption for a 100.1 nm thick $MoS_2$ absorber as shown in **Figure 4.2(c)** and **Figure D.3c** (Appendix D), suggesting that applying a polyimide coating for protective purposes should have no significant negative impact on the cell's performance.

From the calculated $J_{SC}$ for the $PI_{encaps}/MoS_2/PI_{subs}$ stack, along with using 0.92 V $V_{OC}$ and 60.4% fill factor (FF) consistent with the projections in a previous study [62], the estimated specific power as a function of $MoS_2$ thickness was calculated for a solar cell including the polyimide substrate and encapsulant. This $PI_{encaps}/MoS_2/PI_{subs}$ stack represents a fully encapsulated single cell unit, scalable to a full module with other units in series or parallel with interconnects. Model projections indicate that for a 7.1 nm thick $MoS_2$ absorber, ~5 kW/kg can be attained, which is comparable to existing Si and GaAs flexible PV cells (which are not fully encapsulated into modules) [127]–[129] and much higher than the 0.1 kW/kg specific power for ultrathin flexible Si modules. [130] Specific power of our $MoS_2$ flexible thin film solar cell, which does include the encapsulating layers associated with full module construction, approaches 12.97 kW/kg at 100 nm thickness. These results show that 2D TMDC PV has the potential to be the leading candidate for high specific power applications, such as those in space.

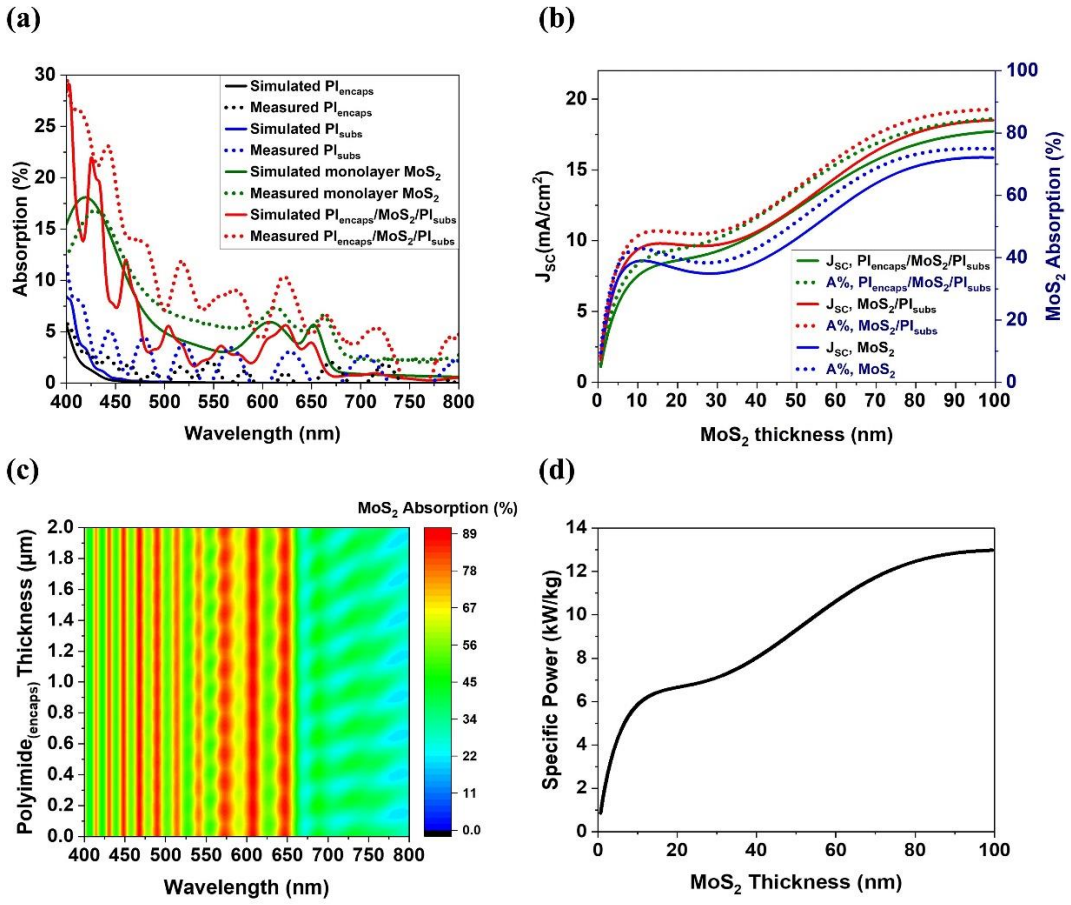


**Figure 4.2:** a) Simulated and measured absorption spectra for the $MoS_2$ monolayer, polyimide substrate ($PI_{subs}$), polyimide encapsulant ($PI_{encaps}$), and the 1.6 µm encapsulant on monolayer $MoS_2$ on 3 µm polyimide substrate stack ($PI_{encaps}/MoS_2/PI_{subs}$). b) Simulated $J_{SC}$ and absorption vs. $MoS_2$ thickness using the TMM for the $MoS_2$, $MoS_2/PI_{subs}$ and the $PI_{encaps}/MoS_2/PI_{subs}$ stack. c) Simulated absorption spectra in the 100nm thick $MoS_2$ layer vs polyimide encapsulant thickness using TMM for the $PI_{encaps}/MoS_2/PI_{subs}$ stack. d) Simulated specific power for the 2D Ti-$MoS_2$-Pt solar cell, encapsulated on a polyimide substrate, vs $MoS_2$ thickness.

## 4.3 Electrical Performance and Bending Tests

To characterize these flexible 2D $MoS_2$ solar cells, 0.25 $cm^2$ (as shown in **Figure 4.1(c))** and 0.0015 $cm^2$ active area cells, sandwiched between polyimide layers, were fabricated as previously described, and the current density-voltage (JV) characteristics under AM0 one Sun illumination were obtained. The JV measurement for a device with a

1 μm channel length between the interlocking metal contacts is shown in **Figure 4.3(a),** showing a $V_{OC}$ of 0.121 V, $J_{SC}$ of ~0.2 mA/cm$^2$, 30% FF, 0.0006% power conversion efficiency, and a specific power of 0.001 kW/kg. Solar cells with back interdigitated contacts of 1, 3, and 5 μm channel lengths were fabricated and measured to show the dependence of cell performance on channel dimensions. The average specific power for nine solar cells of each channel length 1, 3 and 5 μm, shown in **Figure 4.3b,** clearly indicates that the shorter 1 μm channel length is more desirable in the cell design. The average $V_{OC}$, $J_{SC}$, FF, and efficiency of the cells are also shown in **Figure D.4** (Appendix D). While the $V_{OC}$ and FF show no significant dependance on the channel dimensions, a strong dependance of $J_{SC}$ on channel length is observed. We attribute the 1 μm channel cells' better performance to the relatively short carrier diffusion length in monolayer $MoS_2$ and the resulting increased fraction of total cell area within the diffusion length of a contact in this lateral contact geometry. An average $V_{OC}$ of 0.130 V, $J_{SC}$ of 0.02 mA/cm$^2$, 28.7% FF, 0.0005% efficiency, and specific power of 0.001 kW/kg was obtained for 1 μm channel solar cells. The low cell efficiency is due to numerous factors, including defects in the large-area film growth and transfer process; for example, small air pockets form between the polyimide encapsulant, $MoS_2$ film, contacts, and polyimide substrate, reducing the total $MoS_2$ to contact coverage over the entire cell area, even after annealing. A more efficient and scalable transfer process is currently being explored. Fermi level pinning is known to degrade $V_{OC}$ in these devices relative to model expectations, though recent work shows pathways to reduce this effect. [131], [132] A low $J_{SC}$ is expected for the 0.65 nm thick monolayer $MoS_2$ absorber; however higher efficiency is expected for thicker active layers and specific power is expected to increase by at least two orders of magnitude with a 100

nm thick absorber layer made from stacking monolayer $MoS_2$, as discussed previously (Fig. 4.2d). And finally, vertical transport devices provide a clear pathway to increase the internal quantum efficiency and reduce series resistance in these devices. [133], [134]

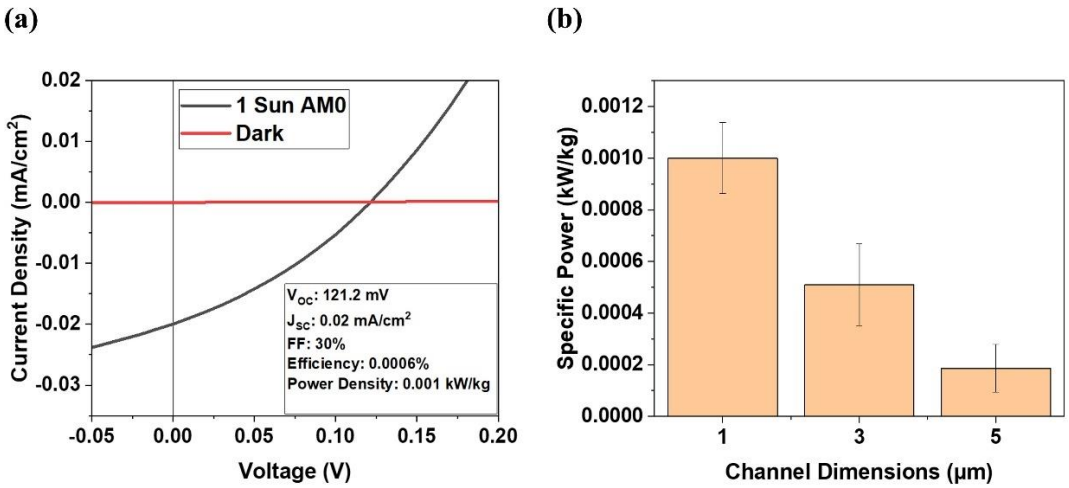


**Figure 4.3:** a) JV performance of a 0.0015 cm$^2$ area monolayer $MoS_2$ lateral Schottky-junction solar cell encapsulated in flexible polyimide under dark and 1 sun equivalent AM0 illumination. b) Specific power vs channel dimensions for these cells under 1 sun equivalent AM0 illumination. All measurements are at room temperature.

### 4.3.1 Bending test

An attractive property of 2D materials is their flexibility and the ease with which they can change substrates. For 2D PV in particular, this property can be leveraged for efficient stowage and deployment, which makes 2D material-based PV desirable for space and other remote applications. To explore the robustness of our flexible cells and their ability to undergo a successful retraction and deployment process, the stack was wrapped around a tube of 5 mm bend radius 10 times, as seen in the inset of **Figure 4.4(a),** and subsequently bent once at a 4, 3 and 2 mm radius. The JV characteristics of the 1, 3 and 5

μm channel cells were measured after each bend. Due to the thin form factor of the stack, when the stack is bent, the stress on the stack can be approximated by the following equation:

$$\varepsilon_f = \frac{d}{2r}$$

where d is the substrate thickness and r is the radius of curvature. [135] At the 5 mm bend radius, the ~4.6 μm stack experienced 0.046% stress. A negligible reduction in the average specific power is observed, compared to the specific power before bending, across all the solar cells when subjecting the devices to a 5 mm bend radius. Furthermore, the $V_{OC}$ of ~0.122 V, $J_{SC}$ of ~0.21 mA/cm$^2$, 31% FF, 0.0006% efficiency and a specific power of 0.0011 kW/kg were consistent after 10 bending cycles as shown in the JV characteristic curves in **Figure 4.4(b)**. The JV characteristics after 10 consecutive bends of a 1 μm channel cell are shown in **Table D.5** (Appendix D). However, further reducing the bend radius resulted in performance degradation across all the samples. An average of 77% specific power reduction was measured for the 4 mm bend radius, and a 100% reduction was seen for the 2 mm bend radius, as shown in **Figure 4.4(a).** Similar observations were made for the $V_{OC}$, $J_{SC}$, FF, efficiency, and the number of working cells as shown in **Figure D.6** (Supporting Information). The degradation of performance after bending to smaller radius is explained by the formation of cracks in the contacts near the finger-busbar junction, resulting in open circuits in the cells. An image of cracks in the Ti contacts is shown in **Figure D.7** (Appendix D); this failure mode is expected due to the sudden change in dimensions at this junction during bending. The test shows that the cell's ability to maintain the same performance after bending is not currently limited by the 2D material's resistance to bending but rather to that of the metal contacts, the design of which may be

modified to improve bending performance. The results highlight the consistency in performance of the 2D solar cells over multiple bends at a 5 mm bend radius, which is desirable for array stowage at launch and deployment in space.

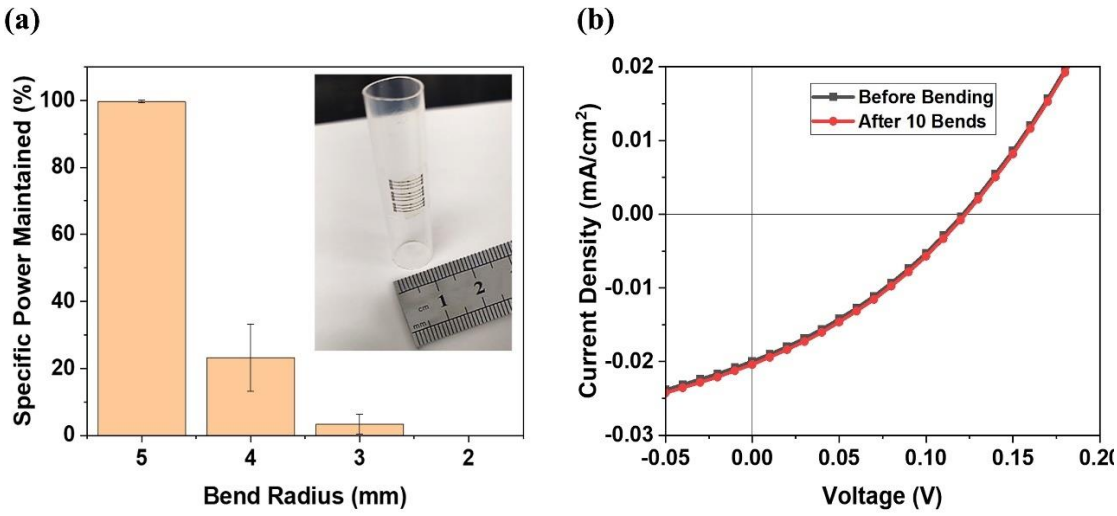


**Figure 4.4:** a) Average specific power maintained (relative to pre-bend performance) vs bending radius of the flexible 2D $MoS_2$ solar cells on polyimide substrates, with inset showing the cells bent at a 5 mm bend radius. b) JV performance of a 0.0015 $cm^2$ monolayer $MoS_2$ solar cell under AM0 one sun illumination before and after 10 bends at the 5 mm bending radius.

## 4.4 Radiation Testing

As mentioned previously, 2D TMDC materials are known for their exceptional radiation tolerance, and here we validate the performance of these devices under radiation levels typical of low Earth orbit conditions. **Figure 4.5a-d** shows the comparison of the solar cell's average $V_{OC}$, PL, Raman spectrum, and optical transmission spectrum before and after exposure to 1 MeV electrons at the NEO Beam Alliance Inc. electron accelerator facility. [136], [137] The solar cells and as grown $MoS_2$ films on $Al_2O_3$ substrates without encapsulation were exposed to fluence levels of 1.03e14, 5.02e14, and 1e15 $e^-/cm^2$. The

first of these exposure doses is equivalent to 150 years in low-Earth orbit (LEO), while the latter dose is equivalent to 15 years in geostationary orbit (GEO), both using the displacement damage dose (DDD) method for space solar cell degradation analysis developed for GaAs and Si cells. [136], [138], [139] The average $V_{OC}$ of the solar cells increased after exposure to all fluence levels, as shown in **Figure 4.5a** and **Figure D.8d-f** (Appendix D). A similar trend is observed in the FF, with the exception of the 1 μm smallest channel cells (**Figure D.8g-i**, Appendix D). However, the increase in the $J_{SC}$ was not consistent across all the devices (**Figure D.8a-c**, Appendix D). For example, the 3 μm channel cells post 5.02e14 $e^-/cm^2$ exposure and the 5 μm channel cells post 1e15 $e^-/cm^2$ exposure both had a decrease in average $J_{SC}$. A possible explanation for decreased $J_{SC}$ is the loss of $MoS_2$ film through slight film degradation or etching during exposure. Nevertheless, an average improvement in the efficiencies is observed for all exposures and channel lengths, as shown in **Figure D.8j-l** (Appendix D), with the largest increase in efficiency, by a factor of 2.2, occurring after the 1.03e14 $e^-/cm^2$ exposure in **Figure D.8j** (Appendix D). The solar cell performance improvements are attributed to radiation-induced defect healing in the $MoS_2$ film, similar to the observations made by Vogl, et al., while studying the radiation resistance of $WS_2$, [110] or radiation induced improvements in the $PI_{encaps}/MoS_2/PI_{subs}$ and $MoS_2$/metal contact interfaces. This defect healing is supported by the average ~24% increase in PL shown in **Figure 4.5b** after exposing the as-grown $MoS_2$ films to 1 MeV electrons with fluence of 1.03e14 $e^-/cm^2$. **Figure D.9a** also shows an average increase in PL after 5.02e14 $e^-/cm^2$ exposure of ~15%, along with an average PL red shift of ~2.28 nm is seen. The red shift can be attributed to slight film delamination from the sapphire substrate during irradiance, resulting in strain relaxation.

Slight PL reduction is observed after the 1e15 $e^-/cm^2$ exposure, with more strain relaxation red-shifting the PL by ~3.05 nm, corresponding to a 0.01 eV decrease in bandgap. The standard monolayer $MoS_2$ $A_{1g}$ to $E^1_{2g}$ Raman peaks, located at ~405 and ~385 $cm^{-1}$ respectively, remained consistently after each fluence level, as shown in **Figure 4.5c** and **Figure D.10a-b** (Appendix D). However, a decrease in the average Raman peak intensity ratio I($A_{1g}$)/I($E^1_{2g}$) is observed, as expected for the relaxation of compressively strained 2D materials. [84] [126] The intensity ratio changes from ~1.13 after the 1.03e14 $e^-/cm^2$ exposure, to ~1.11 after the 1e15 $e^-/cm^2$ exposure which is indicative of some delamination and relaxation of the $MoS_2$ film. Finally, a decrease in optical absorption and red shift of the absorption edge for the $MoS_2$ films is observed with increasing radiation exposure, shown in **Figure 4.5d**. The red-shift in absorption edge correlates with the aforementioned compressive strain relaxation. The decreased absorption is likely due to the loss of some of the $MoS_2$ material during the radiation process, which is likely offsetting the defect healing in the relatively lower PL increase for higher fluence levels seen in the PL data. This highlights the importance of encapsulation to mitigate against loss of active material after deployment of 2D PV in space. While interface investigations are beyond the scope of this work, we expect that both the material quality and the 2D semiconductor/contact interfaces to have significant effects on the solar cell's performance in the space environment. The beneficial effects of defect healing and interface treatment under radiation will eventually be overcome by material degradation from prolonged exposure, albeit at fluences associated with exposure duration far beyond the expected lifetime of standard space PV.

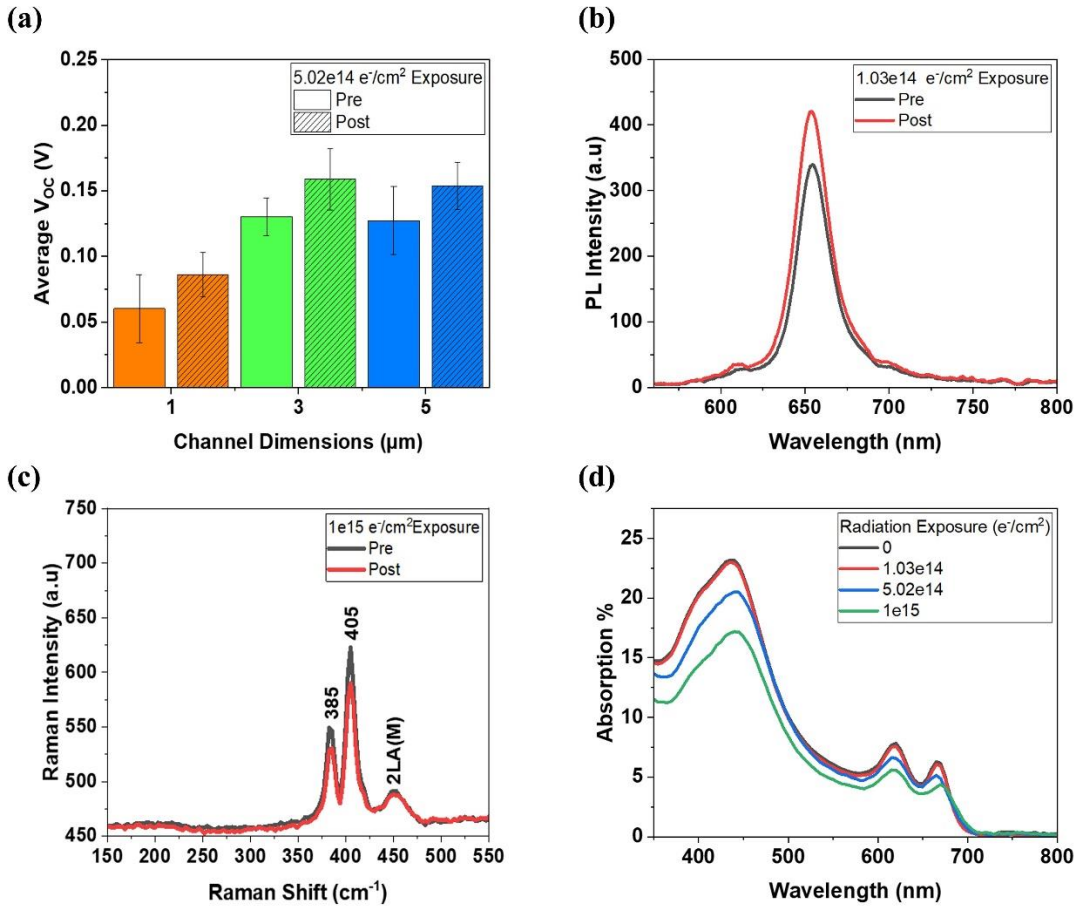


**Figure 4.5:** a) Average $V_{OC}$ before and after 5.02e14 $e^-/cm^2$ of 1 MeV electron radiation exposure for the 2D $MoS_2$ solar cells at different channel dimensions. b) PL spectra of the as-grown monolayer $MoS_2$ film before and after 1.03e14 $e^-/cm^2$ of 1 MeV electron exposure. c) Raman spectra of this film before and after 1e15 $e^-/cm^2$ of 1 MeV electron exposure. d) Optical absorption of this film before and after 1.03e14, 5.02e14 and 1e15 $e^-/cm^2$ of 1 MeV electron exposure.

## 4.5 Design and Techno-Economic Analysis of 2D PV for Space Deployment

An ideal application for the 2D solar cell is to generate power for spacecrafts like nanosatellites and CubeSats. The deployment of these miniature spacecrafts has grown significantly in recent years for several mission types, including interplanetary, low earth orbit (LEO), medium earth orbit (MEO), geostationary transfer orbit (GTO), geostationary orbit (GEO) and other missions. To date, over 2500 nanosatellites and 2300 CubeSats have

been launched as of January 1, 2024, launch failures included. [140] For an average mass of 1.5 kg per U (1000 $cm^3$), the total estimated mass of launched CubeSats is greater than 7428 kg. [141] Body mounted solar panels can be used for low power CubeSats, while deployable panels which are easily scalable, use lightweight backsheets for cell support, and feature compact opening mechanisms can be used to meet higher power demand CubeSats. [118] Replacing conventional thin film solar panels with ultrahigh power density deployable 2D PV arrays can result in even higher power generation per mass while further reducing the payload volume at launch.

## 4.6 CubeSat 2D PV Power System Design

A full-scale 2D material-based flexible 60 W solar power system compatible with a 6U CubeSat was designed as shown in **Figure 4.6,** based on the experimental sub-scale array prototype demonstrated in this work. The power generation system consists of four triangular cell arrays, composite polymer booms with stored strain energy for the array deployment (as implemented in the Roll-Out Solar Array, or ROSA), [142], [143] and a central electrical hub, all stowed in a 300 $cm^3$ housing at launch.

Each triangular array is fabricated on the strong, tear-resistant colorless polyimide (CP1) substrate used in this work, which is similar to the material used for NASA's CP1TM solar sail produced by NeXolve. [124], [144] The design is also compatible with other array deployment mechanisms such as origami pattern deployment. [145], [146] The CubeSat with the solar arrays fully deployed is shown in **Figure 4.6a.**

## 4.7 Array Deployment

Deployment of a 3 μm thick PV array in LEO presents a unique challenge and opportunity to an aerospace system integrator. The two main approaches to deployment for an ultra-thin array are unfolding and unrolling. Using a compliant boom mechanism, or a compliant array itself, enables passive deployment and reduced system complexity. [145] Folding patterns informed by origami researchers offer new and creative ways to stow systems, and 2D arrays can take unique advantage of these techniques due to their thickness and flexibility. The design shown in **Figure 4.6a** posits a compliant mechanism in the form of a high strain composite boom that unrolls to unfold the array in a sail-like manner. This array architecture and deployment mechanism has been demonstrated at technology readiness level (TRL) 6 in practice [147], [148], in a manner well-matched to a 2D material PV array. More mature deployment methods like the flexible composite boom we propose exist for traditional cells, most notably NASA's ROSA, which has two successful deployments in LEO on the International Space Station.

In our 6U CubeSat design, the 2D material-based solar cells include a 3 μm thick polyimide backsheet with 4 μm thick by 2 mm wide gold cell interconnects fabricated on the same backsheet. The cell-to-cell interconnects are shown in **Figure 4.6b**. The front is coated with a 1.6 μm thick transparent polyimide layer for cell encapsulation and structural support as shown in **Figure 4.6b**, which can be optimized as a flexible antireflection coating [149] for increased absorption in the semiconducting layer. For this design, we use our previously modeled results for $V_{OC}$ and FF, where each cell has a $V_{OC}$ of 0.7 V, which is lower than the estimated 2D $MoS_2$ $V_{OC}$ of 0.92 V to account for non-idealities, and a FF of 60.4%. [150] The TMM modeled $J_{SC}$ of 16.61 mA/cm$^2$ for a 78 nm

thick $MoS_2$ absorber between polyimide layers is used here. Each cell is 10.24 $cm^2$ in area and supplies 0.54 V and 12.91 $mA/cm^2$ at the maximum power point. To achieve the target output voltage of >27 V, 51 cells are wired in series, with 6 parallel strings in each array blanket (four arrays in the total system). A total of 1224 cells is required to achieve the required 60 W of output power by end of life (EOL) (~88 W at beginning of life (BOL)), with total solar power system area of 1.51 $m^2$.

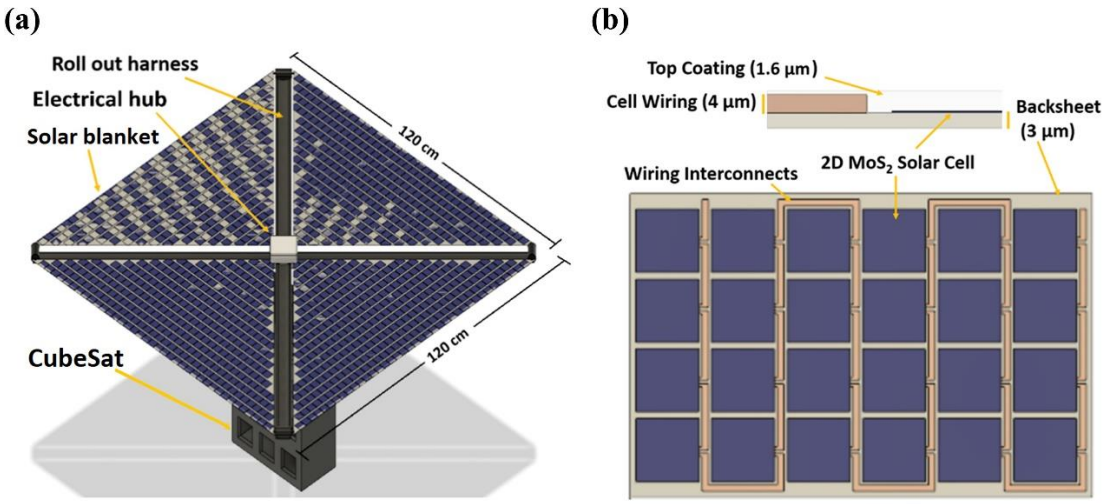


**Figure 4.6:** a) Schematic of a 2D-material based solar power system deployed in space on a 6U CubeSat. b) Schematic of the array cross-section and top view with cells and wiring on the polyimide backsheet.

Assessing the practical feasibility of a new PV technology requires techno-economic analysis to compare against existing options. Two critical figures of merit for space-based PV are specific power (W/kg) and cost of power ($/W). **Equation 4.1** is used to calculate the power cost and **Equation 4.2** is used to calculate the specific power for the module.

$$Power\ Cost_{total}\left[\frac{\$}{W}\right] = Power\ Cost_{material}\left[\frac{\$}{W}\right] + \frac{Cost_{orbit}\left[\frac{\$}{kg}\right]}{Specific\ Power\ \left[\frac{W}{kg}\right]} \qquad \textbf{Eq 4.1}$$

$$Specific\ Power\ \left[\frac{Watt}{kg}\right] = \frac{Power\ Output\ [W]}{Total\ PV\ Mass\ [kg]} \qquad \textbf{Eq 4.2}$$

Where Total PV Mass includes the solar power producing units but not the support structure or central electronics; for the 2D PV array, this includes the top coating, back sheet, cells, and interconnect wiring. Specific power (W/kg) informs the relative cost to launch a payload to orbit and the power available to mass-constrained space missions. The cost of power ($/W) is derived from the manufacturing and launch cost of the PV power units and is an appropriate indicator of feasibility in space. The cost incurred launching mass to LEO, $2720/kg for Falcon 9 as of 2018, [151] dominates the cost of manufacturing the PV system, and so a more expensive system to manufacture can be economical if it has a higher specific power. This total power cost does not include integration expenses, which are challenging to model accurately and are borne by the spacecraft integrator and not the PV system manufacturer. Cost projections for commercialized 2D cells and arrays are modeled with a detailed bill of materials from supplier quotes and device design parameters, with performance metrics based on the aforementioned modeled device with multiple layers of 2D $MoS_2$. The benchmark space PV comparison used here is a SunPower monocrystalline Si PERC commercial panel. [120] PERC cells are used by the space industry due to their relatively low cost of power ($/W) and competitive efficiency, [152] making them a relevant benchmark for powering CubeSats in LEO. All relevant parameters and calculated values for comparing the 2D PV array with a PERC panel are displayed in **Table D.11-15 (Appendix D)**. In **Table 4.1,** a side-by-side technology comparison

presents a 2D and silicon specific power of 6697.74 W/kg and 26.02 W/kg, respectively, when the mass of the metal contacts and interconnects are added. This specific power advantage of the thin-film design is also reflected in the total power cost (material plus launch) comparison, at $104.83 per watt for the PERC panel and $12.64 per watt for the 2D PV array. This specific power advantage demonstrates the practical potential for 2D nanomaterial-based PV to be used in mass constrained environments like space. The advantage of 2D PV over conventional Si space PV is even greater when the support structure weight and cost is included. The results show that although 2D TMDC-based PV may have lower PCE, their significant advantage in specific power and cost to deploy in space, relative to the current most commonly deployed space PV technology, makes them a compelling option for further investigation.

**Table 4.1:** Comparison of 2D PV Array with Si PERC Panel Deployment in Space.

| Performance Metrics | 2D Array | Si PERC Panel |
|---|---|---|
| Cost/Area ($/m$^2$) | $ 863.14 | $ 21,238.94 |
| Weight/Area (kg/m$^2$) | 0.0105 | 10.64 |
| Power/Area (W/m$^2$) | 70.58 | 276.77 |
| Specific Power (W/kg) | 6697.74 | 26.02 |
| Cost/watt ($/W) | $ 12.64 | $ 104.83 |

## 4.8 Methods

### 4.8.1 Synthesis of $MoS_2$ and PV Device Fabrication

$MoS_2$ films were synthesized by chemical vapor deposition (CVD) in a MTI OTF-1200X-II dual zone split tube furnace with a third low temperature zone heated by a Grainger SLR series silicone heating blanket. ACS reagent ≥99.5% molybdenum (VI) oxide ($MoO_3$) powder and 99.98% trace metals basis sulfur (S) powder precursors were used. More growth details are discussed in previous work. [55] To fabricate the 2D solar cells, the contacts were patterned using a RAITH VOYAGER 100 electron beam lithography (EBL) tool, and the Ti and Pt contacts were both deposited using an Angstrom Engineering Nexdep electron beam evaporation tool. A surface-energy-assisted film transfer process, [49] was used to transfer the monolayer $MoS_2$ film from an $Al_2O_3$ substrate onto the contacts on the polyimide substrate. The complete steps are shown schematically in **Figure D.1** (Appendix D).

### 4.8.2 Solar Cell Absorption and JV Characteristics

The absorption measurements were obtained using a Perkin Elmer LAMBDA 750 UV/Vis/NIR spectrophotometer equipped with an integrating sphere. The solar cell's current−voltage characteristics are measured by using a Keithley 2450 sourcemeter. A TS-Space Systems Unisim five-zone solar simulator with tunable halogen and metal halide lamps and three tunable LEDs is used to simulate the 1 sun AM0 illumination conditions at room temperature.

### 4.8.3 Radiation test

The radiation tests were conducted using a 5 MeV 150 kW electron accelerator at the NEO Beam Alliance – Mercury Plastics electron radiation facility. The electron beam was scanned over a test plate with the samples mounted, similar to a scanning electron microscope. Samples were grouped by exposure time for ease of planning. Once an exposure target was reached, the beam was paused, and the relevant samples were removed from the test plate. This procedure was repeated until the full dose of 1e15 electrons/$cm^2$ was achieved for the third batch of samples, for a fluence on the three batches of 1.03e14 e/$cm^2$, 5.02e14 e/$cm^2$ and 1e15 e/$cm^2$. A thermocouple was mounted between the Faraday cup and test stage to monitor temperature throughout testing. The maximum recorded temperature was roughly 40$^o$C as shown in **Figure D.16** (Appendix D).

## 4.9 Conclusions

In summary, we present the design, modeling, and fabrication of large-area CVD-grown monolayer $MoS_2$-based flexible PV devices on 3 μm polyimide substrates with polyimide encapsulation, developed for deployment in space. The cell JV performance is characterized under a 1 sun AM0 simulated illumination source and an average $V_{OC}$ of 0.130 V, $J_{SC}$ of 0.0198 mA/$cm^2$, 28.7% FF, 0.0005% efficiency, and specific power of 0.001 kW/kg is achieved for 1 μm channel solar cells, with a maximum efficiency of 0.0006%. We explore the performance improvement of these PV devices with thicker $MoS_2$ films. Model projections indicate that the polyimide encapsulant introduces negligible absorption in the 400-800 nm range, and with a 7.8 nm (12 stacked monolayers) thick $MoS_2$ absorber, ~5 kW/kg can be attained, which is comparable to existing Si and GaAs flexible PV cells

and exceeds existing modules. Furthermore, 12.97 kW/kg can be obtained for a 100 nm thick $MoS_2$ layer. The bending test reveals the ability of the flexible solar cells to maintain performance after multiple bending cycles to a 5 mm bend radius, which is suitable for array stowage and deployment in space applications, and that both the metal contacts and 2D material's resistance to bending are important in applications where the cells will be bent. Performance is shown to improve after radiation exposure to 1 MeV $e^-$ fluence equivalent to 150 years in LEO or 15 years in GEO, which can be partially attributed to defect healing. Lastly, we present the design and techno-economic analysis of 2D PV for a 6U CubeSat. The results show that although 2D TMDC-based PV may have lower PCE, their specific power projects to be two orders of magnitude higher than a Si PERC panel, and the cost when deployed in space forecasts to be one order of magnitude less. This indicates that flexible, large-area, high-specific-power 2D material-based PV has great potential for space applications. Continued emphasis on improving 2D PV cell performance is critical to achieve large-scale adoption of 2D PV in space.

## 4.10 Future Directions

Thin-film deployable space arrays from 2D materials can increase the power to mass performance with additional monolayers as shown by the model results. One of the next steps in this work is the fabrication of 2D Schottky PV with thicker absorbers by stacking monolayers on contacts deposited on flexible polyimide back sheets. While Schottky PV architecture is reported in this work, p-n homojunctions or heterojunction 2D PV could result in better charge carrier separation and lead to even higher specific power performance. It would be good to explore vertical or lateral transport 2D p-n junction PV in future steps.

Tandem cells, composed of 2D materials with multiple bandgaps, can also be explored to maximize output voltage and power density. For example, $MoSe_2$ can be used in tandem with $MoS_2$ PV to boost power generation in the 430-480 nm range. Furthermore, the flexible PV demonstrated here can be scaled to larger area. The design can be adapted to an even more scalable optical lithography process which could lead to easier adaptation in industry.

# CHAPTER 5

# HIGH PERFORMANCE VERTICAL TRANSPORT 2D PHOTOVOLTAICS FROM LARGE-AREA CVD GROWN $MoS_2$

Several groups have demonstrated the use of 2D materials to produce solar cells of various architectures, highlighting a number of advantages such as flexibility and high specific power, [108], [115], [117] According to Bernardi et al., PV based on 2D materials have the potential to achieve specific powers up to three orders of magnitude greater than the specific power of conventional PV. [46] A power conversion efficiency (PCE) of 5.1% and specific power of 4.4 kW/kg was demonstrated for a flexible $WSe_2$ solar cell by using graphene contacts, $MoO_x$ encapsulation for doping, passivation and anti-reflective coating, and a film transfer technique to fabricate the PV devices on flexible polyimide substrates. Their projections indicate that the 2D solar cells could attain specific power of up to 46 kW/kg, [117] Other studies suggest that specific power > 100 kW/kg can be attained using these material even though <13% might be the limit to their PCE.[107] The record PCEs and specific powers are from solar cells fabricated with exfoliated TMDCs. However, some efforts are focused on scalability by the implementation of TMDC films produced using synthesis techniques such as chemical vapor deposition (CVD) and a Schottky PV design. [62], [116] While these studies show promise in scalability, the PCEs are relatively low (< 1%). Along with poor charge carrier separation and fermi level pinning in these Schottky devices, these devices are limited in efficiency by an architecture where the charge carriers travel laterally (in-plane) through the films over several microns or more in distance, instead of vertically (out-of-plane) through the films over 100 nanometers or less in distance. A solution to this problem is a vertical carrier transport device architecture. Such

architecture requires the use of a front contact with low optical absorption, such as graphene or transparent conductive oxides (TCOs). [153], [154] Vertical transport Schottky PV has been demonstrated by Shanmugam et al., where 110 nm and 220 nm thick $MoS_2$ films synthesized by the thermal vapor sulfurization of Mo film, with Au and indium tin oxide (ITO) asymmetric workfunction contacts, resulted in a PCE of 0.7% and 1.8% respectively. [134] Wang et al. reported on a proof-of-concept electrochemical PV using a conformal liquid electrolyte junction to facilitate vertical charge transport in $MoS_2$, $WSe_2$, and $MoS_2/WSe_2$ solar cells, achieving PCEs up to 0.19%. [133] Wong et al. achieved 3.4% PCE using a multilayer TMDC vertical transport heterostructure device of 0.6 nm-thick few-layer graphene/9 nm $WSe_2$/3 nm $MoS_2$/Au. [155]

In this work, we propose the design and explore the fabrication process of vertical carrier transport Schottky 2D PV that, for the first time, uses large-area CVD grown $MoS_2$. In the design, the as-grown $MoS_2$ films are transferred onto a transparent contact like graphene or ITO, and then a back contact of Pt or Au is added. To explore the device fabrication, the $MoS_2$ films are transferred on a 700 nm thick ITO film on a soda lime glass substrate and Pt contacts are transferred onto the $MoS_2$ film to form a ITO/$MoS_2$/Pt stack for a vertical carrier transport PV architecture. The work shows a promising pathway towards improved performance in large-area 2D materials-based PV for high performance solar energy harvesting applications.

## 5.1 Vertical 2D Schottky PV Design and Modeling

### 5.1.1 Device Design

To form the 2D $MoS_2$ Schottky PV, the $MoS_2$ active layer is sandwiched by two contacts, with one contact having low optical absorption. The contacts are selected with large workfunction asymmetry to ensure selective transport of the excited carriers into either the hole-selective contact or the electron-selective contact, a necessity for charge carrier separation in the device. ITO and Pt are good candidates for such a device architecture since ITO is optically transparent in the visible and has a low work function of 4.5 eV compared to the Pt contact work function of 5.5 eV. [131], [153], [156] This results in ITO serving as an electron selective contact ($\Phi_e$) and Pt serving as a hole selective contact ($\Phi_h$). The energy band diagram of the device is shown in **Figure 5.1**. The associated band bending at the ITO/$MoS_2$ interface on the right of the band structure is shown. Here, the 4.5 eV work function leads to an almost ohmic contact at the junction. However, a large Schottky barrier is formed at the $MoS_2$/Pt interface with the 5.5 eV work function. The asymmetry in the band bending is critical for carrier separation under illumination in the device as discussed in previous work. [62], [134]

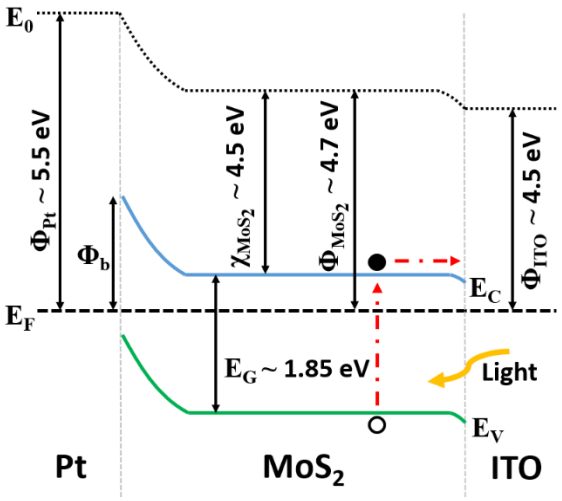


**Figure 5.1:** Band structure of an ITO/$MoS_2$/Pt Schottky-junction photovoltaic showing the asymmetric band bending at the contact/$MoS_2$ interfaces.

## 5.2 PV Device Model

COMSOL Multiphysics simulation tool's Semiconductor Module was used to produce 1D finite element analysis device models to compare the performance of lateral and vertical carrier transport Schottky 2D $MoS_2$ PV devices with ITO and Pt asymmetric workfunction contacts. Firstly, a 100 nm thick (154 stacked monolayers) and a 0.65 nm thick (single monolayer) $MoS_2$ absorber layer was used to explore the performance of both device architectures, then the device performance vs film thickness and channel length was characterized to further explore the limitations of both architectures. Note that while devices with larger film thicknesses made from stacked $MoS_2$ monolayers may be difficult to fabricate, previous work on stacking these monolayers shows potential for scalability [126] and the ability to maintain desirable monolayer-like optical properties, as discussed previously in Chapter 4. Using the Semiconductor Analytical Doping Model, the $MoS_2$ was homogeneously doped with a donor concentration of $1 \times 10^{18}$ $cm^{-3}$. [157] A bandgap of 1.85

eV, electron affinity of 4.5 eV, relative permittivity of 3.5, electron effective density of states $2.66 \times 10^{19}$ $cm^{-3}$, and hole effective density of states $2.86 \times 10^{19}$ $cm^{-3}$ were used for the $MoS_2$ layer. [158], [159] Shockley-Read-Hall (SRH) recombination is implemented in the model to account for loss in the device, [113], [160] and is parameterized by electron and hole carrier lifetimes. The lifetime of 1.85 ns used in the model was experimentally measured for our $MoS_2$ films using time resolved photoluminescence lifetime (TRPL) as shown in **Figure E.2**, (Appendix E). A mobility of 50 $cm^2$ $V^{-1}s^{-1}$ was used for the lateral transport and monolayer devices, which is within the range of in-plane mobility values for CVD grown $MoS_2$ films [161]; however, a mobility of 0.3 and 1 $cm^2$ $V^{-1}s^{-1}$ was chosen for the monolayer and stacked monolayer vertical transport devices where a lower out-of-plane mobility is expected. [162]

The ITO and Pt work functions used were 4.5 and 5.5 eV respectively.[131], [153], [156] The energy band structure of the device is calculated by the model. The band structure forms an upward bend in the energy band at the $MoS_2$/Pt interface and a nearly ohmic contact at the ITO/$MoS_2$ interface as shown in **Figure 5.1** and **Figure E.3**, (Appendix E), which results in the charge carrier separation in the device. A more ideal device can be achieved with Schottky barriers at both $MoS_2$-contact interfaces such that an asymmetric downward bend (hole barrier) and upward bending (electron barrier) occurs in the band structure. For example, asymmetric contacts with $\Phi_e < 3$ eV and a $\Phi_h > 5.5$ eV would lead to more desirable band bending at the interface thus increasing carrier selectivity and resulting electric fields. In this design, monolayer graphene with a 4.3 eV work function is a good alternative to ITO. For the lateral device architecture, the 2 μm wide contact finger used in previous experimental work [62], [126] is used and is accounted for in the total

device area. The contact spacing between fingers defines the channel length for the lateral device; however, the channel length is defined by the $MoS_2$ film thickness in the vertical device architecture. In both designs, as the channel length decreases, the more the entire channel length becomes a part of the depletion region as shown in **Figure E.3**, (Appendix E), and more efficient carrier collection is expected due to the shorter path length and limited diffusion length (~0.04 μm in the vertical device with 0.3 $cm^2\ V^{-1}s^{-1}$ mobility and ~0.49 μm in the lateral device with 50 $cm^2\ V^{-1}s^{-1}$ mobility) of the carriers. A schematic of the lateral carrier transport PV architecture is shown in **Figure 5.2a** and of the vertical carrier transport PV architecture in **Figure 5.2b**.

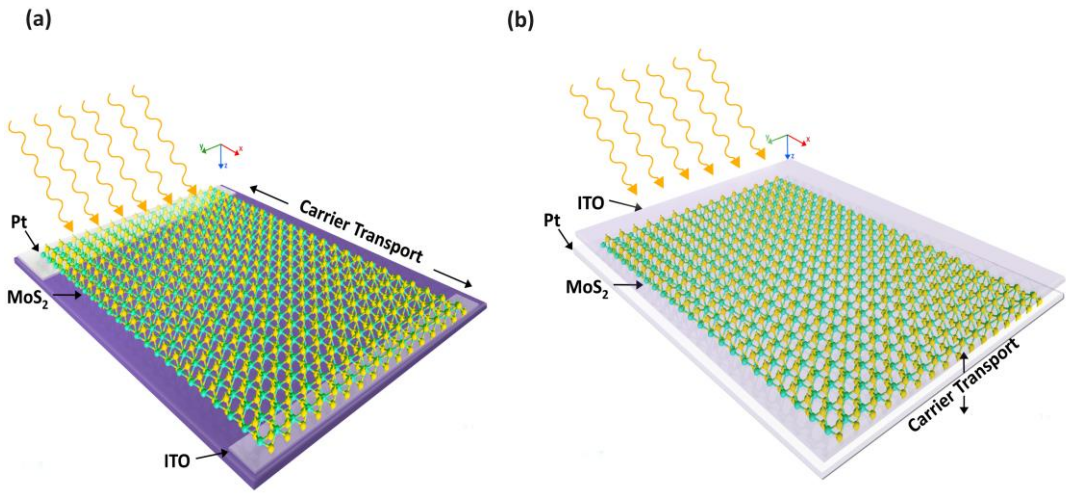


**Figure 5.2:** (a) Schematic of a lateral carrier transport Schottky photovoltaic with monolayer $MoS_2$ film on top of the interleaved ITO and Pt contact fingers. (b) Schematic of a vertical carrier transport Schottky photovoltaic with monolayer $MoS_2$ film sandwiched between a bottom Pt contact and a top ITO contact.

In the model, the photogeneration ($G$) in the devices under AM1.5D solar irradiance are calculated using **Equation 5-1**. The monolayer $MoS_2$ extinction coefficient ($\alpha$) from

our previous work [55] is used in **Equation 5-2** to calculate the absorption in the device, and the photon flux ($\varphi$) is calculated from **Equation 5-3**.

$$G = \int_0^\infty \alpha(\lambda)\varphi(\lambda)\exp(-\alpha(\lambda)z)\,d\lambda \qquad \textbf{Eq. 5-1}$$

$$\alpha(\lambda) = \frac{4\pi\kappa(\alpha)}{\lambda} \qquad \textbf{Eq. 5-2}$$

$$\varphi(\lambda) = \frac{\lambda}{hc}F(\lambda) \qquad \textbf{Eq. 5-3}$$

In **Equation 5-1**, $z$ is the depth into the $MoS_2$ layer from the surface. In the vertical transport device, the generation profile changes with depth $z$, decreasing through the $MoS_2$ film from the top ITO contact to the bottom Pt contact, whereas the lateral transport device has a constant generation profile in the $MoS_2$ film across the entire junction (x-y plane). $\lambda$ is the wavelength of the light irradiating the device. In **Equation 5-2**, $\kappa(\lambda)$ is the wavelength-dependent extinction coefficient, and in **Equation 5-3,** $F(\lambda)$ is the AM1.5D solar irradiance spectrum.

For the current density-voltage (J-V) calculations, the model assumes that all the generated electron-hole pairs that do not undergo recombination based on the SRH recombination model can participate in carrier transport, and the carrier mobility is accounted for in the one-dimensional drift model for carriers in the electric field of a typical semiconductor. The constant generation profile calculations are discussed in **Section E.4**, and the generation and recombination profiles for 100 nm thick $MoS_2$ film vertical and lateral transport PV devices are shown in **Figure E.4a** and **b** (Appendix E) respectively.

Additionally, the recombination rate within the channel vs the channel length is shown in **Figure E.5** (Appendix E).

### 5.3 PV Device Fabrication

To fabricate the device, high quality large-area $MoS_2$ films are synthesized by chemical vapor deposition (CVD). A tube furnace was used to facilitate the reaction of molybdenum oxide ($MoO_3$) with sulfur (S). Precursor quantities of 1 mg of $MoO_3$ and 230 mg of sulfur were used, and the growth temperature was 750 °C. To achieve quasi-epitaxial growth, C-plane sapphire ($Al_2O_3$) substrates were used where $MoS_2$ (lattice constant 3.212 Å) and sapphire (lattice constant 4.814 Å) form a 3-on-2 superstructure.[47] Ultrahigh-purity argon was flowed at 180 sccm during the temperature ramp, and once the growth temperature reached 750 °C, the sulfur was heated to 120 °C. A growth time of 10 mins was used for the films. More details on the synthesis can be found in the Experimental Methods section. ITO coated float glass (soda lime) microscope slides were obtained from SPI Supplies. The 700 nm thick sputtered ITO film has a sheet resistance of 8-12 ohms per square (Ω/□). The as-grown $MoS_2$ film was transferred from the sapphire substrate onto ITO coated substrates using the surface energy assisted transfer process. [49] Thicker $MoS_2$ films are achieved by stacking multiple monolayers using the same transfer technique. The Pt metal contact was patterned using electron beam lithography to define the device active area (0.04 $mm^2$) but can also be done using photolithography. The metal was deposited by electron beam evaporation and followed by resist lift-off, and then the patterned back contact was transferred onto the $MoS_2$/ITO stack using the same surface energy assisted transfer process used for the $MoS_2$ film transfer. More discussion on the photovoltaic cell fabrication can also be found in the Experimental Methods section. The contacts are

depicted in **Figure E.1a** and **b** (Appendix E), shown after fabrication on the $Al_2O_3$ sapphire substrate and after transfer unto the $MoS_2$/ITO stack, respectively.

## 5.4 Results and Discussion

### 5.4.1 Model Predictions

The J-V curves for the vertical and lateral devices under a voltage bias between -0.1 and 0.6 V and AM1.5D solar irradiance are shown in **Figure 5.3a** for a 100 nm thick $MoS_2$ film and a 100 nm channel length for both the vertical and lateral transport device. A higher short circuit current ($J_{SC}$) of 21.13 mA/cm$^2$ and an open circuit voltage ($V_{OC}$) of 0.62 V is achieved in the vertical device compared to the 0.11 μA/cm$^2$ $J_{SC}$ and $V_{OC}$ of 0.5 V in the lateral device. A $J_{SC}$ five orders of magnitude larger than the lateral device is achieved in the vertical device even with a mobility 0.6% of the lateral device $MoS_2$ mobility. This is attributed to the fact that no carriers are generated over the contact area in the lateral device resulting in a relatively small active area which negatively impacts the current per total cell area. The $V_{OC}$ also decreased because of the decrease in current. A similar trend in $J_{SC}$ and $V_{OC}$ is obtained for a monolayer $MoS_2$ device as seen in **Figure E.6a** (Appendix E). Here, the $J_{SC}$ of 0.45 mA/cm$^2$ and $V_{OC}$ of 0.39 V is achieved in the vertical device and 0.002 μA/cm$^2$ $J_{SC}$ and $V_{OC}$ of 0.36 V is achieved in the lateral device. The vertical device with 100 nm thick active layer has 8.6% efficiency and 169.94 kW/kg specific power, while the lateral device with 100 nm channel length between fingers has efficiency of 0.00004% and specific power of 0.00085 kW/kg. highlighting the benefits of the vertical device architecture. This indicates that the lateral device architecture is a poor design choice for maximizing performance.

For the 100 nm thick absorber, while the lateral junction device has a better fill factor (FF) 78%, compared to the vertical device FF of 66.3% due to higher series resistance

as seen in **Figure 5.3a**, the vertical device outperforms the lateral device in specific power ($P_{s)}$ and efficiency. The FF difference arises from the difference in carrier mobility and sheet resistance; it is also attributed to differences in the diode ideality factor in the vertical device vs. the lateral device. In **Figure 5.3b**, a FF of 66.3%, 74.6% and 79% is obtained for devices with 0.3, 1 and 50 $cm^2\ V^{-1}s^{-1}$ carrier mobilities respectively for the same 100 nm thick $MoS_2$ vertical device with the same generation and recombination profiles. A small increase in $J_{SC}$ by 0.73 and 0.93 $mA/cm^2$ is also observed when the mobility is increased from 0.3 to 1 and then to 50 $cm^2\ V^{-1}s^{-1}$ carrier mobility in the 100 nm thick $MoS_2$ vertical device which is expected for longer diffusion length of the carriers in the semiconductor.

From previous work it was shown that the open circuit voltage ($V_{OC}$) depends strongly on the Pt contact work function (Φh), where the upward band bending is expected. [62] The model projections shows that the $V_{OC}$ also depends on the mobility, film thickness, generation and recombination profile and channel dimensions. For example, for decreasing mobility, an increase in $V_{OC}$ from 0.5 V to 0.6 V and then to 0.62 V for the 50, 1 to 0.3 $cm^2\ V^{-1}s^{-1}$ carrier mobility change is shown in **Figure 5-3b** in the vertical device with.

An increase in $V_{OC}$ from 0.53 V to 0.55V is shown in **Figure E.6b** (Appendix E) for a 100 nm channel length lateral device when the film thickness is increased from 0.65 nm to 100 nm. A similar trend is observed for a vertical device where an increase in $V_{OC}$ from 0.39 V to 0.62 V is observed when the film thickness is increased from 0.65 nm to 100 nm as shown in **Figure 5-3c**. This is attributed to more photogenerated carriers in the thicker film compared to the monolayer film and the large contact cross-sectional area. The 100 nm thick $MoS_2$ absorber lateral transport PV device with a $V_{OC}$ that closely matches the vertical transport device $V_{OC}$ (0.62 V) is shown in **Figure 5.3d**. At this channel length (800 nm), the

lateral device $J_{SC}$ (0.006 μA/cm$^2$) is three orders of magnitude smaller than the vertical device $J_{SC}$.

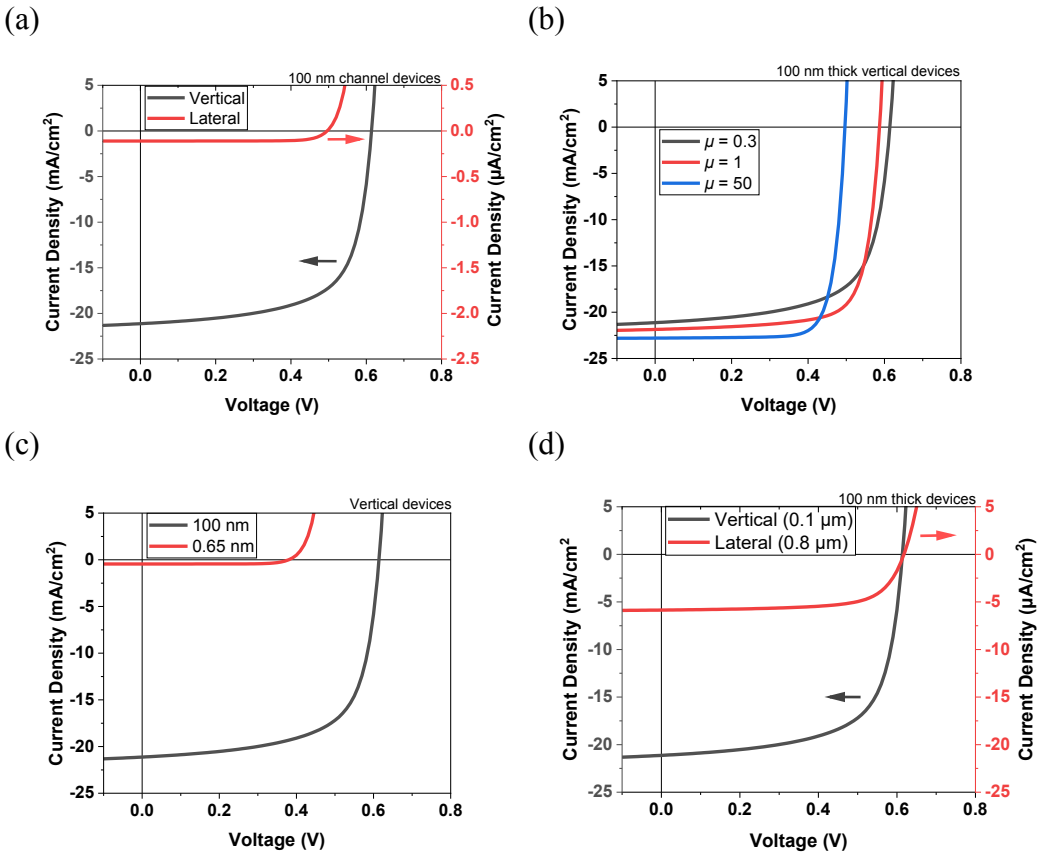


**Figure 5.3:** Simulated J-V characteristics of (a) a 100 nm channel length lateral device and a vertical ITO/$MoS_2$/Pt PV device using a 100 nm thick $MoS_2$ (b) vertical ITO/$MoS_2$/Pt PV devices with 1, 0.3 and 50 cm$^2$ V$^{-1}$s$^{-1}$ carrier mobilities using 100 nm thick $MoS_2$. (c) vertical ITO/$MoS_2$/Pt PV device with 100 and 0.65 nm thick $MoS_2$ films and (d) lateral ITO/$MoS_2$/Pt PV device of 100 $MoS_2$ thickness, with channel length 800 nm, compared to a vertical ITO/$MoS_2$/Pt device of 100 nm thickness, showing a $V_{OC}$ for the lateral device that matches closely with the $V_{OC}$ and of the vertical device.

From **Figure E.4** and **5** (Appendix E), we see that the lowest recombination rates are near the contacts, where the generated carriers are easily collected and from such a profile, we expect the $J_{SC}$ to depend strongly on the channel dimensions in both the vertical

and lateral transport devices. The highest generation rate is at the illuminated surface of the device. Due to a continuous contact/$MoS_2$ interface over the entire device area for the vertical devices, we expect more generated carriers to be collected because of the shorter path length for a larger number of the generated carriers compared to a lateral device whose channel dimensions are equal to the film thickness of the vertical device, especially when the channel dimensions are larger than the carrier diffusion length. In the lateral device, more of the generated carriers away from the contacts recombine before collection and therefore less carriers contribute to the overall lateral device current.

The $J_{SC}$ and $V_{OC}$ versus film thickness for vertical architecture devices with carrier mobilities of 0.3 and 1 $cm^2\ V^{-1}s^{-1}$ are shown in **Figure 5.4a** and **b** respectively. A significant increase in $J_{SC}$ and $V_{OC}$ is shown for up to 100 nm of film thickness in the device with a carrier mobility of 0.3 $cm^2\ V^{-1}s^{-1}$, after which the $V_{OC}$ begins to decrease. The increase in $J_{SC}$ becomes less dramatic up to 200 nm where the device output power peaks, after which a decline is observed. The J-V characteristic curves (**Figure E.7a**, Appendix E) show increasing series resistance as the film thickness increases. A similar trend is seen for the device with a carrier mobility of 1 $cm^2\ V^{-1}s^{-1}$, however the $V_{OC}$ continues to increase less dramatically along with the $J_{SC}$ up to the peak output power at 400 nm thickness. The results show that higher specific power and efficiency can be obtained for higher carrier mobilities and thicker films in the vertical device. The vertical device architecture continues to outperform the lateral architecture device even at larger film thicknesses. **Figure 5.4c** shows the $V_{OC}$ and $J_{SC}$ of a lateral device with a carrier mobility of 50 $cm^2\ V^{-1}s^{-1}$. The maximum $V_{OC}$ is 100 mV less than that of the vertical devices in **Figure 5.4a** and **b**, and the maximum

$J_{SC}$ (4.5 μA/cm$^2$) attained at 1 μm thickness is three orders of magnitude lower than in the vertical devices. The J-V characteristic curves are shown in **Figure E.7b** (Appendix E).

From previous experimental work on lateral transport Schottky junction 2D PV, where the mobility was estimated to be between 1 to 3 cm$^2$ V$^{-1}$s$^{-1}$, no dependance of $V_{OC}$ on channel length was observed for the channel lengths of 1, 3, 5, 10, and 15 μm. [62] This is expected, as shown in **Figure 5.4d**, where the $V_{OC}$ dependance on channel length for the 100 nm thick $MoS_2$ film with 50 cm$^2$ V$^{-1}$s$^{-1}$ carrier mobility only becomes significant at channel lengths < 4 μm. No further increase in $V_{OC}$ is seen as the channel length is increased to as far as 30 μm, however, $J_{SC}$ continues to increase up to a channel length of 6 μm, after which fewer carriers are able to get to the contacts resulting in a decrease trend in $J_{SC}$ for channel lengths > 6 μm. The J-V characteristic curves are shown in is shown in **Figure E.7c** (Appendix E) which indicates increased series resistance as the channel length is increased.

The lateral device in **Figure 5.4d** achieved a maximum efficiency of 0.0015% and a specific power of 0.029 kW/kg, however the vertical device achieved a maximum efficiency of 8.6% and a specific power of 169.7 kW/kg. The model results show that the vertical device architecture is better for high performance 2D PV than the lateral architecture. Higher $P_s$ can be achieved for lower $MoS_2$ thickness in a vertical device that can lead to better device efficiencies. Furthermore, at the low $MoS_2$ films thicknesses, the Pt contact serves as a back reflector, giving the device a second opportunity to absorb the reflected photons, and the glass and ITO thicknesses can be optimized to function as an anti-reflective coating to further increase the solar cell's performance.

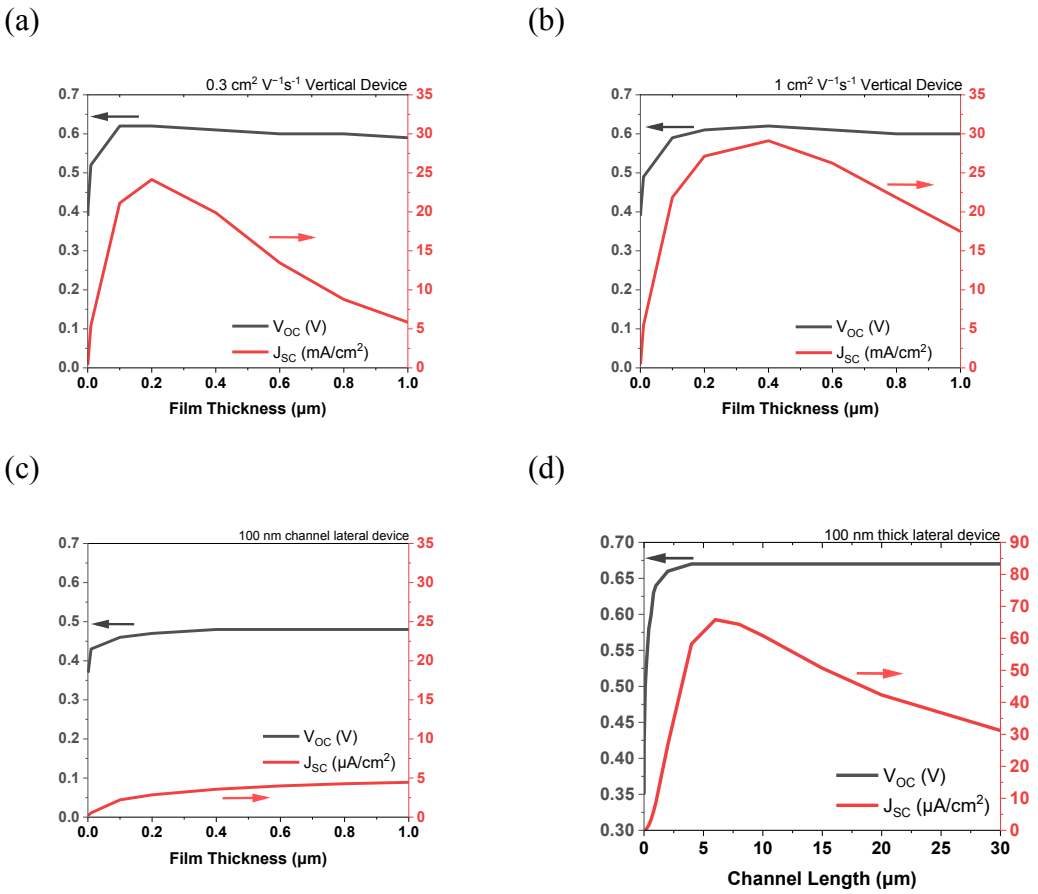


**Figure 5.4:** Simulated $V_{OC}$ and $J_{SC}$ vs film thickness for a vertical transport with (a) 0.3 and (b) 1 cm$^2$ V$^{-1}$s$^{-1}$ carrier mobilities, (c) lateral transport architecture vs film thickness and (d) lateral transport vs channel length for films with 50 cm$^2$ V$^{-1}$s$^{-1}$ carrier mobilities.

## 5.5 Experimental Results and Analysis

Preliminary results for a monolayer ITO/$MoS_2$/Pt vertical PV device with active area of 4 x 10$^{-4}$ cm$^2$ are shown in **Figure 5.5**. The IV curves indicate that no charge carrier separation may have occurred in the device. One thing to note is that a monolayer $MoS_2$ film was used in this case, and significant shunting may be present in the device due to a low resistance between the Pt and ITO contact (essentially a short circuit at various pinhole defects). A possible approach to mitigate against this is by increasing the $MoS_2$ layer

thickness by stacking multiple monolayer films. Additionally, the work function of the ITO contact needs to be measured to ensure that the work function relative to the Pt work function is ideal for a Schottky PV device. The aforementioned issues are being addressed in ongoing efforts.

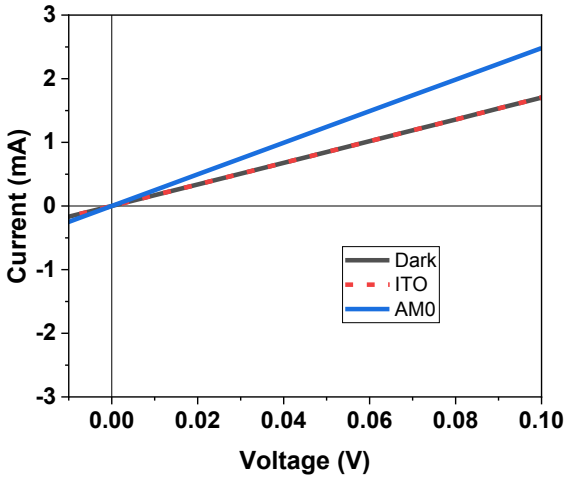


**Figure 5.5:** Preliminary J-V characteristics of an experimental ITO/$MoS_2$/Pt vertical 2D PV device. The red curve is an ITO-only film.

## 5.6 Conclusions

The design and modeling for large-area, vertical-transport 2D $MoS_2$ Schottky solar cells have been presented using ITO and Pt as the contacts. Significant modeling was performed to assess and compare the difference in solar cell performance for various designs of both vertical and lateral device architectures for these $MoS_2$-based photovoltaics. The results from the model comparing the device architectures show that the vertical architecture PV device outperforms the lateral device in both $J_{SC}$ and $V_{OC}$, leading to higher efficiency and specific power in vertical devices even under varying $MoS_2$ film thickness and channel length. In the vertical devices, $J_{SC}$ is projected to be up to 3 orders of magnitude larger than

the lateral devices, even with an out-of-plane mobility less than that of the in-plane lateral transport device. The design and model demonstrate that high performance solar cells can be achieved using vertical transport photovoltaics from these 2D TMDC materials. Experimental validation of these predictions is underway.

## 5.7 Experimental Methods

### 5.7.1 $MoS_2$ film Synthesis

The 2D $MoS_2$ films are grown by CVD using an MTI OTF-1200X-II dual zone split tube furnace and a third heating zone created by placing a Grainger SLR series silicone heating blanket around the 1-inch diameter quartz tube on the upstream end. 99.98% trace metals basis sulfur (S) powder and ACS reagent ≥ 99.5% molybdenum (VI) oxide ($MoO_3$) powder from Sigma-Aldrich were used as the synthesis precursors. A ½ $inch^2$ c-plane sapphire substrate was placed on top of an alumina crucible. 1 mg of $MoO_3$ powder was placed ~1.5 cm upstream from the growth substrate and the crucible with the $MoO_3$ powder and sapphire substrate was placed in the tube in the heating zone 1 of the tube furnace. The 230 mg of sulfur was placed in an alumina crucible and positioned beneath the heating blanket. The tube was vacuumed down to 15 mTorr, then argon (Ar) gas was flowed at 180 sccm for 10 minutes to fully purge the system. The temperatures of both heating zones of the furnace were ramped to 750 °C in 50-minutes. When the set temperature was achieved, the heating blanket was ramped to 120°C. A growth time of 10 minutes was used. More growth details and schematics are reported in our previous work. [55]

### 5.7.2 Contact Patterning and Transfer

To fabricate the Pt contacts, 200 nm of 495 A4 PMMA resist, followed by 400 nm of 950 C4 PMMA resist, both from Kayaku Advanced Materials, were spin coated on the

$Al_2O_3$ substrate. A 15 nm thick chromium layer was used for charge dissipation. The RAITH VOYAGER 100 electron beam lithography (EBL) tool was used to pattern the contacts. The Cr layer was etched using Chromium etchant from Sigma-Aldrich before development. After development, 100 nm thick Pt was electron beam evaporated to form the contacts at a deposition rate of 0.5 Å/s using an Angstrom Engineering Nexdep evaporator. After liftoff, the surface energy assisted transfer technique is used to transfer the contacts. [49] The steps are shown schematically in **Figure E.8** (Appendix E).

## 5.8 Future Directions

It is important to have a continuous $MoS_2$ film sandwiched in the vertical device to prevent shorting between the contacts. Since the monolayer films are being transferred with a flexible carrier film and the stack is then submerged in a solvent to dissolve the carrier film, there is a possibility of gaps and tears arising in the $MoS_2$ film from the transfer process. One way to address this is by stacking multiple monolayer $MoS_2$ films, where pinhole defects and small tears are unlikely to overlap. Improved mechanical support in the transfer process will also help minimize shunt defects. The next step in this work is to stack multiple monolayer films to obtain thicker absorber layers before transferring the Pt contacts onto the stack. This will ensure that a continuous $MoS_2$ layer lies between the ITO and Pt contacts while also enhancing optical absorption, $J_{SC}$, and overall performance.

While the work function of the contacts plays a key role in the $V_{OC}$ and ultimately the efficiency of the Schottky PV, the contacts also contribute significantly to the total mass of the 2D solar cell. It would be beneficial to explore other contact candidates for transparent contact such as graphene that can lead to specific power improvements with higher sheet

resistance per contact layer thickness. Future efforts will be focused on exploring the candidate contacts' work functions (e.g. looking at other transparent conductive oxides and metal contact options) through ultraviolet photoelectron spectroscopy (UPS) to identify the best candidates for maximizing the $V_{OC}$ while reducing the overall mass of the solar cell. This will be beneficial for applications where specific power performance is critical and will enable much higher $V_{OC}$ to be obtained.

# CHAPTER 6

# CONCLUSION AND FUTURE PERSPECTIVES

This dissertation has been written to contribute to ongoing work that is geared towards the development of ultrathin 2D material-based optoelectronics and photovoltaic devices and the improvement of their efficiencies. 2D materials exhibit an array of extraordinary properties due to their quantum effects and that can lead to new dimensions of applications. Some of the exciting applications of these devices include flexible and wearable electronics where light to energy conversion applications is not constrained by bulky or ridged supports. Another application is in deep space exploration where both the solar propulsion system and photovoltaics are integrated to reduce cost in our drive to explore and understand the universe. Four important components critical for the large-scale deployment of 2D materials in photovoltaic applications were explored in this dissertation: scalable large-area 2D TMDC synthesis; film morphology control and efficient film characterization; large-area flexible 2D space photovoltaics; and fundamental advances in device architecture for improved 2D PV performance. These advances highlight the potential benefits of employing these 2D materials in important applications involving light-matter interactions.

## 6.1 2D Material Synthesis

The work in Chapter 2 reports on the development of a CVD growth process for large-area monolayer $MoS_2$ growth at ~0.5 $in^2$ size. The process is easily scalable and can be adapted to produce wafer scale films of 2D materials. Domain size > 10 μm was achieved with uniform monolayer films over 160 $mm^2$ area. The reduction in domain

boundaries and morphology improvements shown can lead to higher quality films, thus increasing device efficiencies.

Additionally, results shown from the single station setup for correlative spatial mapping of 2D film properties at sub-micron resolution presented highlights the wealth of information that can be extracted from such a technique. The significance of the common characterization techniques namely, photoluminescence spectroscopy, optical transmission and photocurrent measurements become much more apparent once the correlations are presented. The development of tools to provide high throughput characterization can accelerate the development of synthesis processes and facilitate shorter optimization times.

The desire to improve on the scalability of 2D materials and the material quality has been a major thrust in academia and industry. The goal has been to find inexpensive and high yield manufacturing processes for this unique family of material. Reducing the dimensions and manufacturing cost of devices while at the same time increasing their efficiencies can speed up other technological advancements. For example, the development of ultra-light, wearable self-powered biosensor systems, for human health monitoring in real time can lead to significant advancements in biomedical research while improving the health of the patient.

## 6.2 2D Material Film Uniformity Control and Characterization

In Chapter 3, the CVD film synthesis technique was optimized to grow large-area $MoS_2$ films of various morphologies. The growth process can be used to consistently obtain the desired film morphologies, highlighting the robustness of the growth technique. The quazi-epitaxial synthesis of large-area 2D $MoS_2$ on C-plane sapphire through the optimized

CVD process can be easily adapted in industry, a precursor to wide-scale deployment of 2D material-based devices.

Furthermore, the use of high resolution correlative spatial mapping of the 2D $MoS_2$ based films and devices to show the relationship between the various growth morphologies and optoelectronic device performance was presented with discussion on the insights attainable once the technique is employed. For example, by comparing the device performance maps to the photoluminescence peak shift and intensity can highlight strain and other defects in various film morphologies that inhibit photogenerated current in a 2D material-based phototransistors. The relationship between morphology and device performance on film morphology shown through the correlation of high-resolution Raman, photoluminescence, transmittance, photocurrent, and generated external and internal quantum efficiency spatial maps can give insight to researchers working with these materials and accelerate improvements in device efficiency.

Finally, by stacking monolayers our results suggest that some monolayer properties like absorption can be maintained by stacking instead of using bulk 2D materials. This could potentially lead to highly efficient light absorbers for applications such as high specific power photovoltaics.

## 6.3 2D Photovoltaics for Space Applications

The development of large-area CVD-grown monolayer $MoS_2$-based flexible PV devices on lightweight polyimide substrates for deployment in space is presented in Chapter 4. Under the 1 sun AM0 illumination as expected in space, our fabricated devices achieved an average $V_{OC}$ of 0.130 V, $J_{SC}$ of 0.0198 mA/cm$^2$, 28.7% FF, 0.0005% efficiency, and specific power of 0.001 kW/kg. Furthermore, our model projections show that with

improved material quality, a $V_{OC}$ of 0.92 V and a 60.4 % FF can be achieved, and ~5 kW/kg can be attained with just 12 stacked $MoS_2$ monolayers instead of bulk $MoS_2$ as the active layer of a Schottky junction 2D PV. This specific power is comparable to existing thin film PV technology. The ability to maintain performance after bending to 5mm bend radius over multiple bending cycles shows how these devices can be adapted into applications where the power generation system will need to be stowed or folded, such as space or wearable photovoltaics. Techno-economic analysis shows that 2D TMDC-based PV outperforms Si PERC panels in specific power while costing less for deployment, showing promise in space applications. Furthermore, the increased performance after radiation exposure shows that the system can reliably supply needed power in the harsh space environment for a significant amount of time. All these attributes could help with optimizing future space missions.

### 6.4 New 2D Photovoltaic Device Architectures for Improved Efficiency

The design, fabrication, and characterization of high-performance large-area 2D $MoS_2$ Schottky solar cells, redesigned for vertical carrier transport, is discussed in Chapter 5. The work demonstrates the possibility of having large-area scalable 2D material based photovoltaics with high efficiencies by employing a vertical carrier transport architecture. The design employs the use highly transparent contacts such as graphene or transparent conductive oxides (TCO) at the illuminated face of the solar cell to maximize carrier collection. Model projections indicate that the vertical architecture device outperforms the lateral carrier transport device, further supporting the expectations of high performance solar cells using these 2D TMDC materials compared to conventional materials.

The design can be adapted for flexible high specific power solar energy conversion applications like space missions where low mass is critical for deployment. The design is

also suitable for stacking multiple monolayer 2D films where improved absorption would lead to higher photogenerated current. 2D solar cells with p-n homojunction, heterojunctions, or even multiple junctions can also be easily adapted to the vertical transport design, opening a new window into radical enhancements in 2D PV performance. For example, n-type $MoS_2$ and p-type $WSe_2$ layers can be stacked to form a p-n junction for more efficient charge carrier separation in the device. The space and terrestrial PV industries can benefit significantly from these developments.

## 6.5 Overall Perspective

The contributions towards the development of 2D materials and their devices presented in this work has revealed the wealth of benefits stored in these nanoscale materials. However, there is still room for improvement in 2D materials and devices beyond what was discussed in the future work of each chapter. To reach their full potential, easy access to low cost, large area, low defect synthetic films is critical. A combination of the scalability of the synthesis techniques, low energy growth process, low-cost precursors, and low-cost growth substrates, where direct synthesis on the final substrate is not feasible, are all part of the ingredients needed to achieve this. The maximum film area in this work was limited by the quartz tube diameter, the growth temperature was 750 °C, and the sapphire substrates were used for a single growth. However, larger area films can be produced by increasing the growth chamber, which would in turn reduce the number of growths runs. Lower growth temperatures can also be explored to reduce the energy demand for synthesis and the growth substrate like sapphire could be re-used for multiple growths by using an efficient substrate cleaning process such as piranha etch, thus decreasing the cost of synthesis. New growth substrates that promote epitaxial growth and

are compatible with the synthesis techniques can be further explored through theoretical calculations like density functional theory and can further accelerate the drive to attaining low defect, large-area synthetic films.

One possible addition to the 2D $MoS_2$ CVD synthesis process that has not been explored in this work is the substrate motion during the growth. Film uniformity and quality could potentially be improved by implementing substrate movements such as rotation to promote layer control as the crystals grow. This would involve the use of compatible motorized substrate holder or stage with targeted substrate heating and localized precursor delivery similar to an atomic layer deposition (ALD) system.

At present, film transfer is an unavoidable step in several device fabrication processes that use large area 2D materials. The transfer step could potentially damage the film and add surface impurities that affect the electronic properties, Therefore, more efficient transfer techniques that limit film handling can be developed to improve the yield of devices. For example, an automated film transfer setup using robotics and stage heating that deposits the transfer film on the as-grown 2D material, cures and delaminates the transfer film/2D material stack, then transfers the stack to the receiver substrate and then place the receiver substrate with the stack in the necessary solvent to remove the transfer film can reduce poor film handling during the transfer step.

There is little reported data on the properties of stacked synthetic 2D materials. It is known that the interlayer spacing can be a few angstroms larger than interlayer spacing in the as-grown or exfoliated multilayer films, and it is important to fully understand how this affects the material properties. For example, while the absorption is expected to improve in the vertical PV device, the $J_{SC}$ improvement requires efficient interlayer carrier

transport; therefore more research on the carrier transport mechanism in stacked 2D materials can lead to improved device performance.

Direct synthesis on the desired substrate can also boost device performance. For example, directly synthesizing the $MoS_2$ films on the Pt contact for vertical device architecture in this work can reduce the possibility of shorting between contacts. The deposited metal contact can be annealed to obtain an atomically smooth surface that would then be used for the 2D film growth, similar to how graphene is grown on copper films. This can be easily explored using electron beam evaporation or sputtering for contact deposition, and various growth techniques like CVD and TVS for film synthesis.

2D material homo and heterojunctions can lead to the development of exciting and efficient devices, and exciting device architectures can be further explored and developed adapting existing techniques. For example, $MoS_2$ can be substitutionally doped with group five transition metals such as vanadium (V), niobium (Nb), and tantalum (Ta). This can lead to p-n homojunctions for PV device exploration or other optoelectronic devices. Think of a 2D PV device with $MoS_2$ and $WSe_2$ or other 2D materials in tandem, or a multijunction vertical 2D PV utilizing a combination of p-n homojunctions and heterojunctions to maximize absorption, along with an anti-reflection coating, back reflectors, and mitigation of undesirable recombination pathways through surface passivation. This could potentially lead to ultra-high efficiency and specific power photovoltaics that could surpass the record solar cell performance.

Let's not forget that 2D materials are excitonic materials that can have performance variations under lattice strain that enhance the performance of optical devices. The integration of 2D materials with other tunable or phase-change materials such $VO_2$ and

$Sb_2S_3$ can lead to exciting devices. For example, dynamic tuning of the $MoS_2$ electronic or absorption properties has been shown by inducing strain using an $MoS_2/VO_2$ heterostructure. More unique devices can potentially be attained through asymmetric or localized tuning using such heterostructures. Furthermore, 2D materials can potentially be a go-to material for very high refractive index optical devices like waveguides or to functionalize waveguides due to their excitonic effects and other optical properties.

It has been an exciting journey adding to the knowledge that has been accumulated among researchers over the years in the 2D material space. Due to the rapid pace of advancement, I would not be surprised to see 2D materials used in applications such as wearable 2D photovoltaics and optoelectronics and as a common fixture in society in the near future. This work along with ongoing work will pave the way for such a future.

# FUNDING AND SUPPORT

This work was supported in part by the NASA EPSCoR program of the Louisiana Board of Regents under Award No. NASA(2021)-RAP-37, the NASA Grant and Cooperative Agreement Award 80NSSC20M0110 through Subaward PO-0000244065 with the Louisiana Space Grant Consortium (LaSPACE), the National Science Foundation under Award No. 1727000, the Carol Lavin Bernick Faculty Grant, the CELT Faculty Mentored Undergraduate Research fund, and the Newcomb Institute at Tulane University.

# APPENDIX A

# RELATED PUBLICATIONS, PRESENTATIONS, AND PATENTS

## A.1 PUBLICATIONS

**T. Ismael**, M. A. Abbas, O. P. Harris, G. B. Ingrish, M. E. Bush, J. M. Sasson, J. S. McNatt and M. D. Escarra, *High-specific-power flexible photovoltaics from large-area $MoS_2$ for space applications*, Currently Under Review, 2024

**T. Ismael**, N. J Grinalds, M. A Abbas, N. Hill, C. E Luthy, M. D Escarra, *Correlative spatial mapping of optoelectronic properties in large area 2D $MoS_2$ phototransistors*, Advanced Materials Interfaces, 2023

K. M Islam, **T Ismael**, C. Luthy, O Kizilkaya, M. D Escarra, *Large-Area, High-Specific-Power Schottky-Junction Photovoltaics from CVD-Grown Monolayer $MoS_2$*. ACS Applied Materials & Interfaces, 2022

K. M. Islam, R. Synowicki, **T. Ismael**, I. Oguntoye, N. Grinalds, M. D. Escarra, *In-Plane and Out-of-Plane Optical Properties of Monolayer, Few-Layer, and Thin-Film $MoS_2$ from 190 to 1700 nm and Their Application in Photonic Device Design*, Advanced Photonics Research, 2021

J. Robertson, D. Blomdahl, K. Islam, **T. Ismael**, M. Woody, J. Failla, M. Johnson, X. Zhang, M. D. Escarra, *Rapid-throughput solution-based production of wafer-scale 2D $MoS_2$*. Applied Physics Letters, 2019

## A.2 CONFERENCE ABSTRACTS AND PROCEEDINGS

**T. Ismael**, K. M Islam, M. A Abbas, G. B Ingrish, C. E Luthy, O Kizilkaya, C. M Gutierrez, M. E Bush, J. S McNatt, A. J Hoffman, M. D Escarra, *High-specific-power Schottky-junction photovoltaics from CVD-grown $MoS_2$*, IEEE 49th Photovoltaics Specialists Conference (PVSC), 2022

K. Islam, **T. Ismael**, C Luthy, O Kizilkaya, M. D. Escarra, *2D Materials-based Optoelectronic Devices*, Optical Devices and Materials for Solar Energy and Solid-state Lighting, 2020

## A.3 PRESENTATIONS

**T. Ismael**, K. M Islam, M. A Abbas, O. Harris, G. B Ingrish, C. E Luthy, C. M Gutierrez, M. E Bush, N. Hill, J. S McNatt, A. J Hoffman, M. D Escarra (2023) *Large-area hig-specific-power photovoltaics from CVD-grown monolayer $MoS_2$*, Materials Research Society Spring Conference (MRS)

M. A Abbas, **T. Ismael**, O. Harris, N. Hill, T. Perez-Arteta, C. E Luthy, M. D Escarra (2023) *Optoelectronic properties of stacked CVD-grown $MoS_2$ monolayers toward high-performance 2D material-based photovoltaics*, Materials Research Society Spring Conference (MRS)

**T. Ismael**, K. M Islam, M. A Abbas, G. B Ingrish, C. E Luthy, O Kizilkaya, C. M Gutierrez, M. E Bush, J. S McNatt, A. J Hoffman, M. D Escarra (2022) *High-specific-power Schottky-junction photovoltaics from CVD-grown $MoS_2$*, IEEE 49th Photovoltaics Specialists Conference (PVSC); **Winner of best poster award in category.**

**T. Ismael**, K. M Islam, M. E Bush, C. E Luthy, M. D Escarra, (2021) *CVD-Grown 2D Material Schottky Photovoltaics with Interlocking Asymmetric Contacts*, Materials Research Society (MRS) Meeting & Exhibit

**T. Ismael,** K.M Islam, N. Grinalds, C. E Luthy, and M. D Escarra, (2020) *Correlative Mapping of Photonic Properties in 2D Semiconductors and Optoelectronics*, Materials Research Society (MRS) Meeting & Exhibit

K. Islam, **T. Ismael**, and M.D. Escarra, "2D Materials-based Optoelectronic Devices," *OSA Advanced Photonics Congress*, Virtual, July 2020.

K. Islam, J. Robertson, **T. Ismael**, D. Blomdahl, M. Kothakonda, A. Ollanik, J. Sun, and M.D. Escarra, "2-D $MoS_2$: Rapid Growth and Advanced Opto-Electronic Devices," *MRS Spring Meeting*, Phoenix, AZ, April 2019.

## A.4 PATENTS

"Large-area Schottky-junction photovoltaics using transition metal dichalcogenides," M.D. Escarra, K.M. Islam, **T. Ismael**, US provisional patent application No. 63/343,670, filed May 19, 2022.

# APPENDIX B

# SUPPLEMENTARY INFORMATION FOR CHAPTER 2

## B.1 PATTERNING OF AS-GROWN $MOS_2$ FILMS PHOTOTRANSISTOR FABRICATION

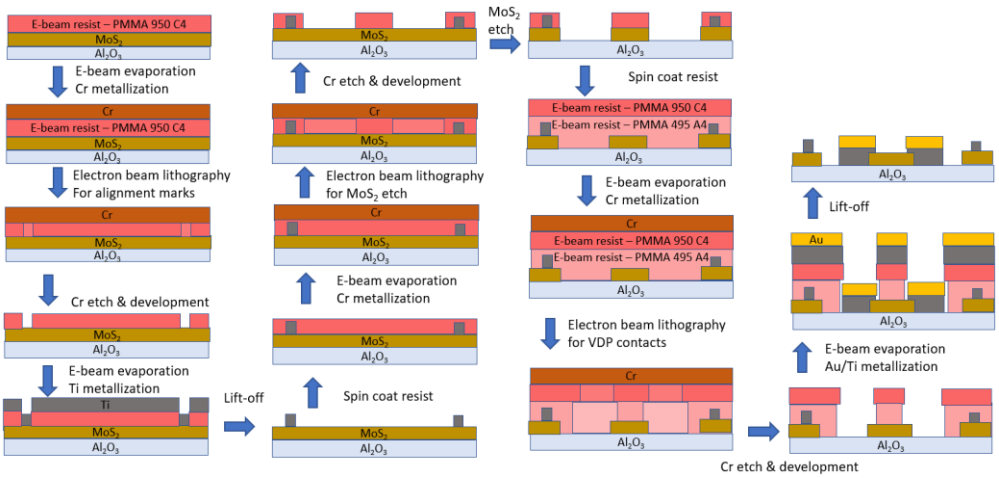


**Figure B.1:** Schematic showing fabrication steps for a phototransistor on as-grown $MoS_2$ film with patterned $MoS_2$.

## B.2 BACK-GATED FIELD EFFECT TRANSISTOR FABRICATION

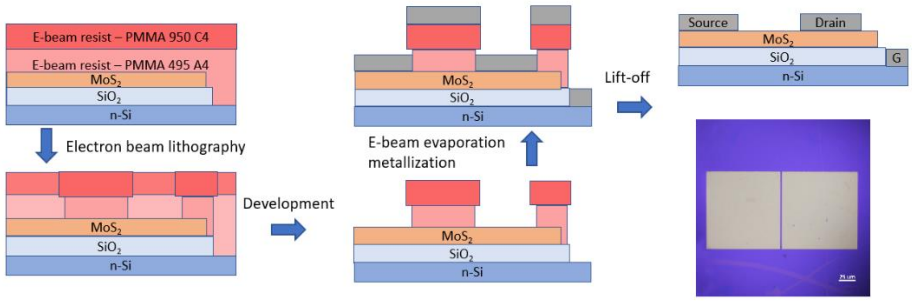


**Figure B.2:** Schematic showing fabrication steps for a back-gated field effect transistor.

# APPENDIX C

# SUPLEMENTARY INFORMATION FOR CHAPTER 3

## C.1 EPITAXIAL GROWTH FROM FLAKE TO FILM DURING CVD $MOS_2$ SYNTHESIS

Precise control of the concentration of $MoO_3$ and the growth time is critical for high-quality and uniformity in large area monolayer $MoS_2$ synthesized by CVD. Good domain orientation control is achieved by using an atomically smooth crystalline sapphire ($Al_2O_3$) substrate.[47] Due to a lattice mismatch between $MoS_2$ and the C-plane (0001) sapphire surface of less than 4.7%,[48] quasi-epitaxial domain growth that subsequently coalesces into a uniform monolayer film is obtained, as shown in **Figure C.1**.

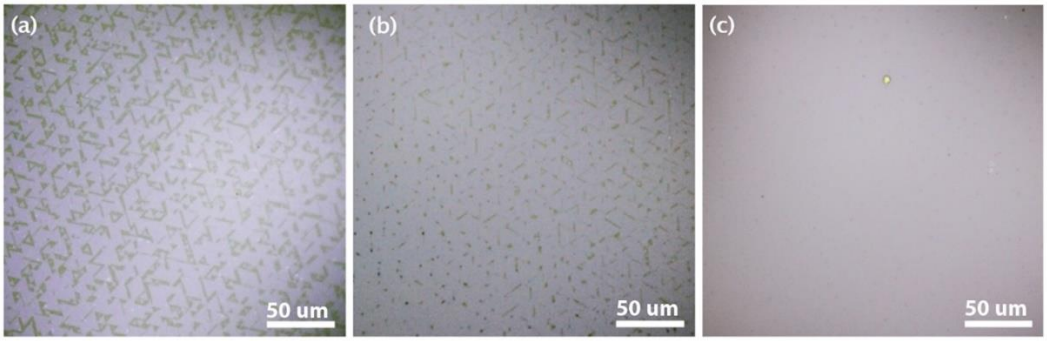


**Figure C.1:** CVD synthesized $MoS_2$ flakes on C-plane sapphire substrate for 1 mg of $MoO_3$ precursor with high flake orientation from (a) sparse, to (b) less sparse, to (c) uniform film coverage for 6, 10, and 12 minutes of growth time respectively.

## C.2 PHOTOTRANSISTOR ON TRANSPARENT $AL_2O_3$ SUBSTRATE SHOWING FLAKE ORIENTATION

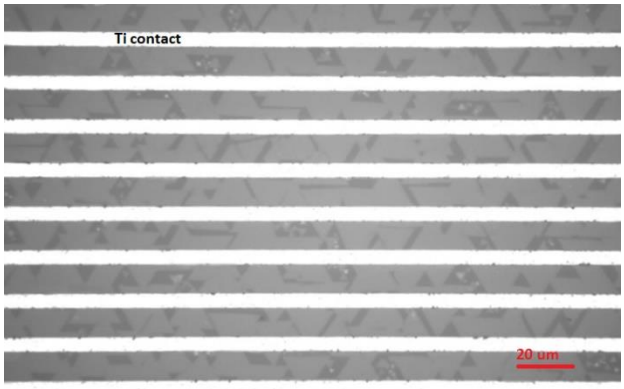


**Figure C.2:** CVD synthesized $MoS_2$ flakes on C-plane sapphire substrate with unidirectional orientation. One edge of the flakes is parallel to the phototransistor's Ti contact fingers.

## C.3 RAMAN SPECTRA FOR AS-GROWN VS TRANSFERRED $MOS_2$ FILMS

**Figure C.3** shows the Raman spectra for CVD-grown monolayer $MoS_2$ samples, showing the comparison between as-grown film (still on its growth substrate) and the as-grown monolayer plus transferred monolayer stack. The standard monolayer $A_{1g}- E^1_{2g}$ Raman peaks are located at 404.54 and 384.82 $cm^{-1}$, respectively. The 19.72 $cm^{-1}$ $A_{1g}- E^1_{2g}$ peak difference observed in both of these samples is consistent with our previous work for monolayer samples. [55], [62] The stacked monolayers sample shows no monolayer to bilayer or bulk transition in the Raman spectrum.

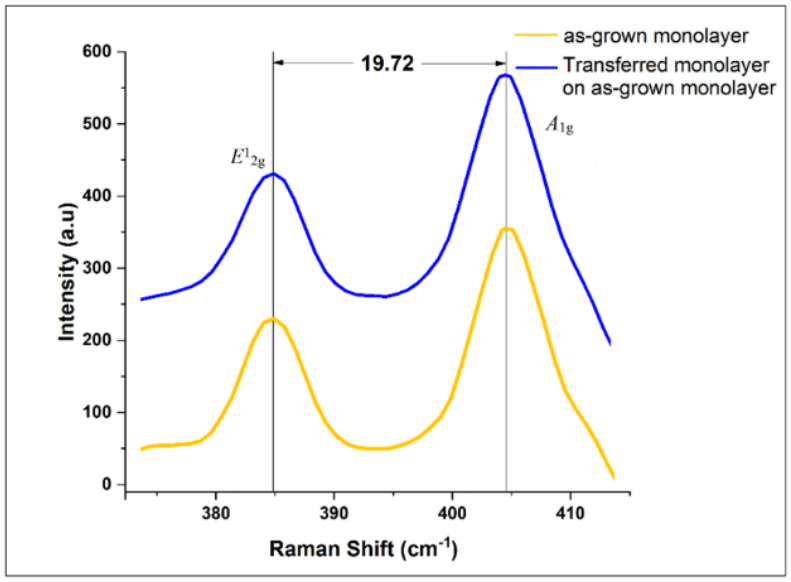


**Figure C.3:** CVD-synthesized $MoS_2$ film Raman spectra for both an as-grown monolayer sample and a sample with an additional monolayer transferred on top.

## C.4 $MOS_2$ FILM STRAIN ANALYSIS FROM RAMAN

Raman spectroscopy can be used to characterize strain in the $MoS_2$ films in this study, including as-grown films and films transferred to various substrates.[47] An increase in Raman peak spacing ($A_{1g}- E^1_{2g}$) is indicative of increasing tensile strain, while an increase in Raman peak intensity ratio I($A_{1g}$)/I($E^1_{2g}$) is indicative of increasing compressive strain. As shown in **Figures C.4a and C.4b**, the peak spacing is not shifting for our materials, nor are the absolute peak locations, which is indicative of samples that are all compressively strained. However, as seen in **Figure C.4c**, Raman peak intensity ratio is shifting, as expected for compressively strained materials. The as-grown strain is relaxed most after transfer to Ti and less so when transferred to sapphire (difference in intensity ratio

I($A_{1g}$)/I($E^1_{2g}$), relative to that of as-grown $MoS_2$, of ~0.08 and ~0.07 respectively). For the film transferred onto as-grown $MoS_2$, the Raman signal from the as-grown film cannot fully be decoupled from the transferred film; however, some relaxation is shown.

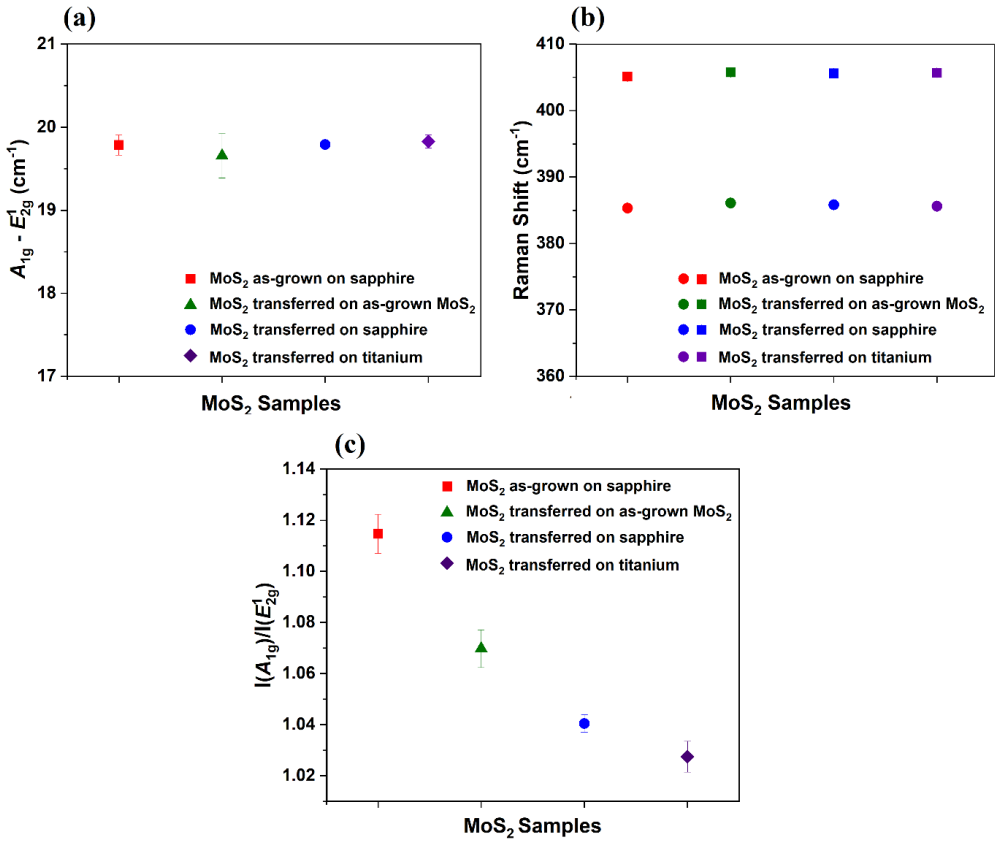


**Figure C.4:** CVD-synthesized $MoS_2$ film Raman spectra are analyzed to understand strain: (a) $A_{1g}$ to $E^1_{2g}$ Raman peak separation, (b) $A_{1g}$ and $E^1_{2g}$ Raman peak positions and (c) Raman intensity ratio I($A_{1g}$)/I($E^1_{2g}$). All data is averaged over 9 locations on the sample and includes standard deviation. $MoS_2$ as-grown on sapphire shows Raman intensity ratio I($A_{1g}$)/I($E^1_{2g}$) M = 1.11, SD = 0.006. The I($A_{1g}$)/I($E^1_{2g}$) results are significantly different for $MoS_2$ transferred on as-grown $MoS_2$ ($p < 0.001$), $MoS_2$ transferred on sapphire ($p < 0.001$), and $MoS_2$ transferred on titanium ($p < 0.001$) compared to the $MoS_2$ as-grown on sapphire.

## C.5 PHOTOLUMINESCENCE COMPARISON OF AS-GROWN VS TRANSFERRED $MOS_2$ FILMS

**Figure C.5** shows the photoluminescence (PL) intensity of a CVD-grown monolayer $MoS_2$ film, before and after transfer onto another $Al_2O_3$ substrate, alongside the PL of an as-grown monolayer plus transferred monolayer $MoS_2$ stack. The excitonic A-peak pre-transfer has the signature PL peak at 672 nm and is consistent with our previous work, [55], [62] while the transferred PL is blue shifted due to film strain relaxation. The stacked film has the same emission peak as the pre-transfer film, indicating that photo-generated electron-hole pairs in the stack are preferentially relaxing into and re-emitting from the as-grown film rather than the transferred film lying on top.

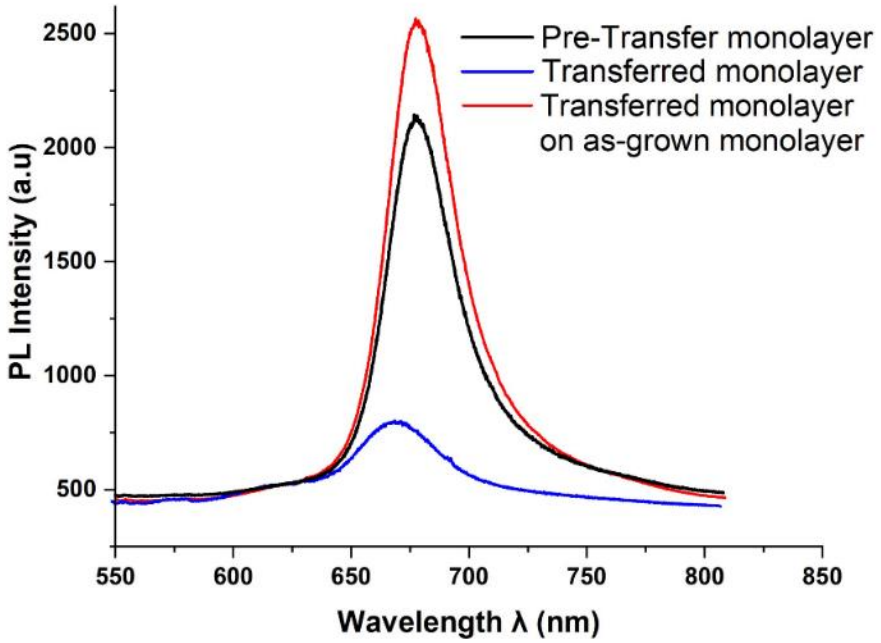


**Figure C.5:** CVD synthesized $MoS_2$ film photoluminescence spectra for a monolayer before transfer, the same monolayer after transfer, and a stack of two monolayers (one as-grown, one transferred on top).

# C.6 RAMAN SPECTRA FOR CVD GROWN $MOS_2$ FILMS AT DIFFERENT PRECURSOR QUANTITY AND SULFURIZATION TIMES

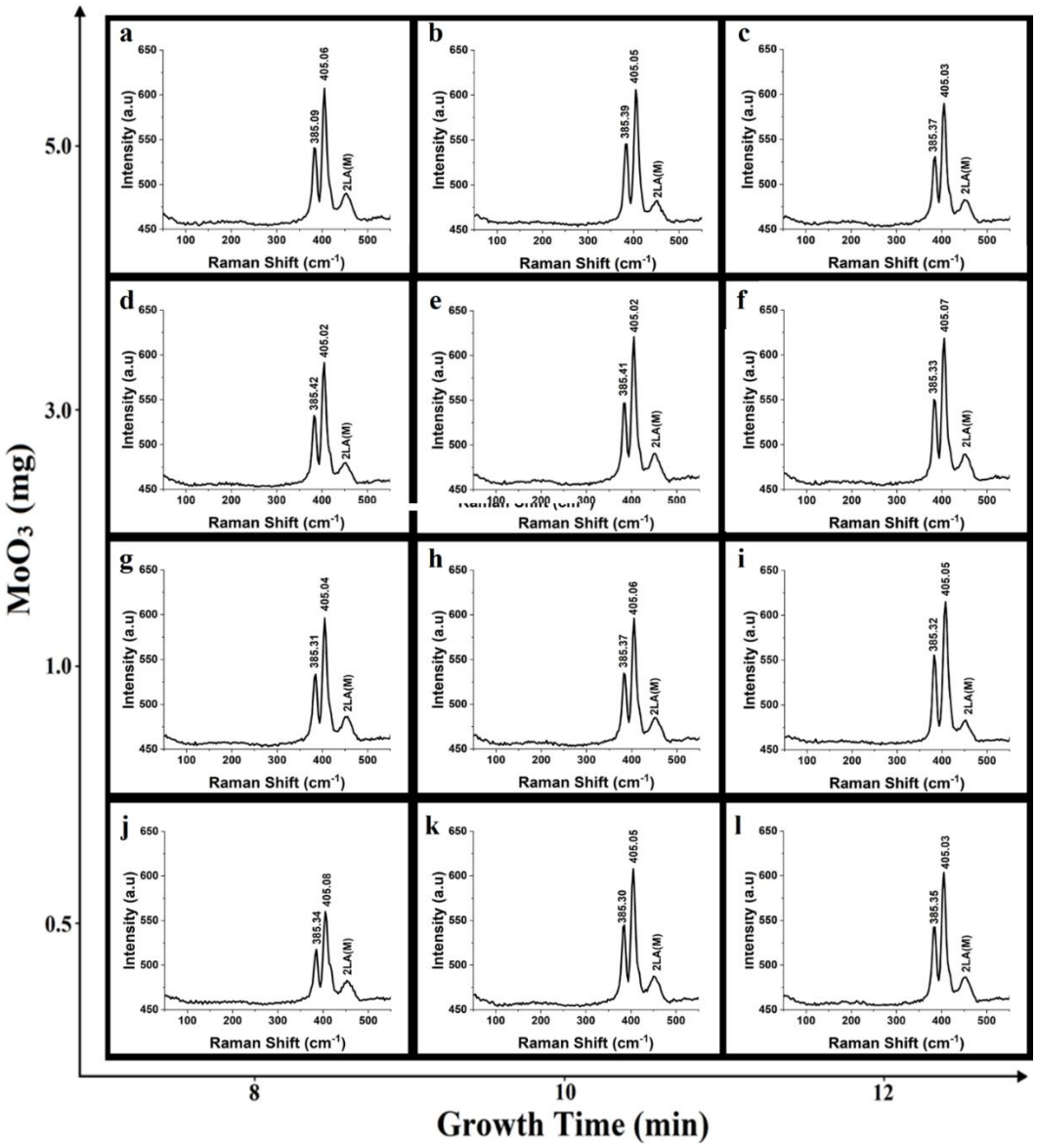


**Figure C.6:** Raman spectra for CVD synthesized $MoS_2$ on C-plane sapphire substrates. Results from varying the amount of $MoO_3$ powder precursor (y-axis) and sulfurization time (x-axis). Signature $A_{1g}$ and $E^1_{2g}$ Raman modes observed at ~385 and ~405 $cm^{-1}$ ($A_{1g}$ to $E^1_{2g}$ Raman peak separation of $\Delta = \sim 20\ cm^{-1}$). A typical second-order longitudinal acoustic phonon peak (2LA(M)) is detected at ~450 $cm^{-1}$.

# C.7 PHOTOLUMINESCENCE SPECTRA FOR CVD GROWN $MOS_2$ FILMS AT DIFFERENT PRECURSOR QUANTITY AND SULFURIZATION TIMES

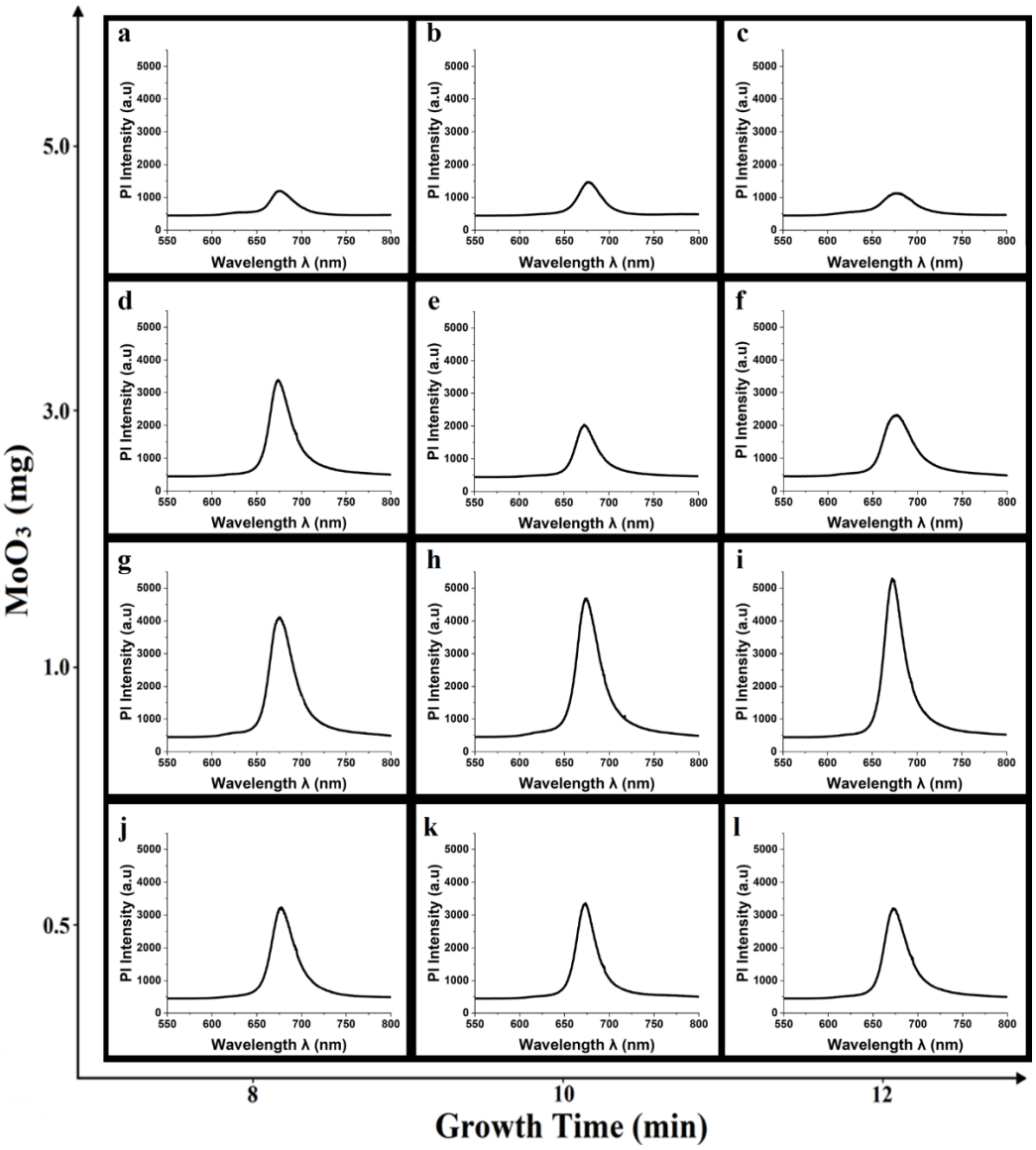


**Figure C.7:** Photoluminescence spectra for CVD synthesized $MoS_2$ on C-plane sapphire substrates. Results from varying the amount of $MoO_3$ powder precursor (y-axis) and sulfurization time (x-axis).

## C.8 STABILITY OF CVD GROWN $MOS_2$ FILMS

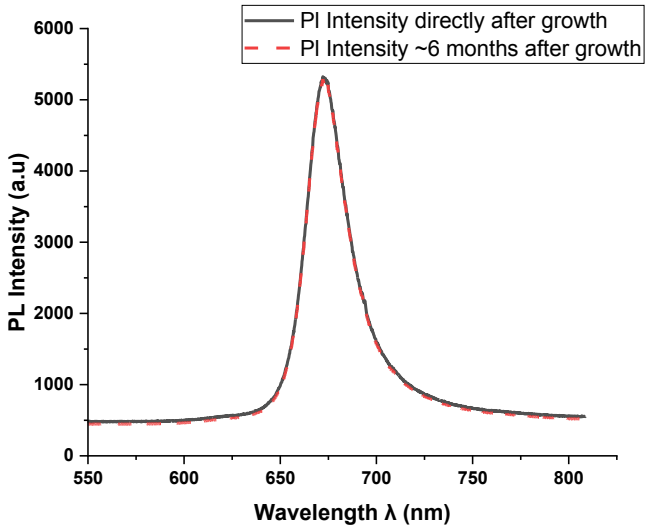


**Figure C.8:** Photoluminescence spectra, averaged over 9 locations on the sample, for CVD synthesized $MoS_2$ film on C-plane sapphire substrates, grown using 1 mg $MoO_3$ and 12 minutes of sulfurization time as seen in Figure 1i, is shown directly after synthesis and ~6 months after, showing no notable degradation

## C.9 FABRICATION STEPS FOR MONOLAYER AND STACKED MONOLAYER $MOS_2$ PHOTOTRANSISTORS ON TRANSPARENT CONDUCTIVE SUBSTRATES

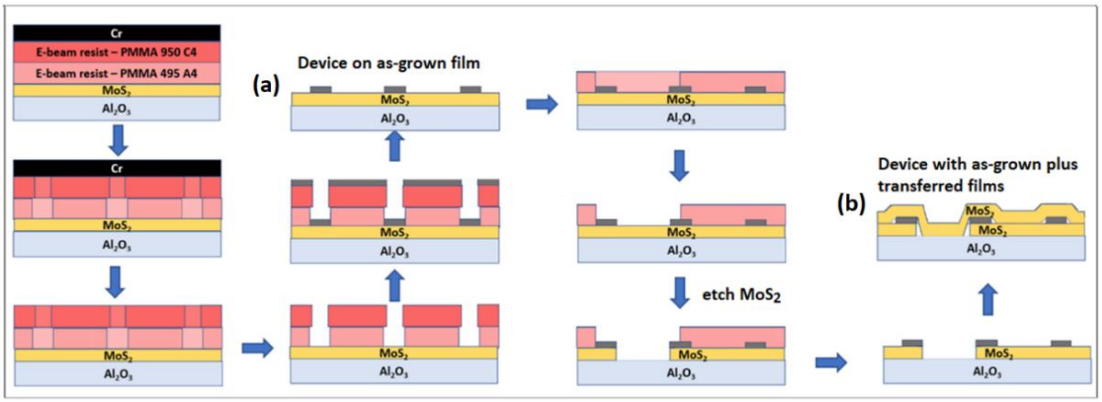


**Figure C.9:** Schematic showing fabrication steps for (a) phototransistors on as-grown $MoS_2$ film and (b) phototransistors with a second transferred monolayer stacked on top.

# APPENDIX D

# SUPPLEMENTARY INFORMATION FOR CHAPTER 4

## D.1 FABRICATION OF $MOS_2$ SOLAR CELL ON NEXOLVE'S CP1™ POLYIMIDE SUBSTRATE

To directly fabricate the two-dimensional (2D) photovoltaics (PV) on a 3 μm thick film of NeXolve's CP1™ Polyimide (PI), a polyvinyl alcohol (PVA) film was spin-coated at 500 rpm for 15 seconds, then 4000 rpm for 45 seconds onto an $SiO_2$/Si substrate from a 10% w/v PVA from Sigma-Aldrich in de-ionized water solution. The PVA was then baked on a hotplate at 180°C for 90 seconds. The PI substrate was placed on the coated PVA/$SiO_2$/Si and the wrinkles and air bubbles were smoothed out using the rubber tip of a stylus pen. The stack was then placed on a hotplate at 180°C for no more than 15 seconds to avoid over-curing the PVA, and again the rubber tip of a stylus pen was used to smooth out the film and remove gaps between the PI and PVA layers while on the hotplate. 10% w/v PVA film was then spin-coated again at 500 rpm for 15 seconds, then 4000 rpm for 45 seconds onto the PI/PVA/$SiO_2$/Si stack. The additional PVA layer serves as a protective layer for the PI from aggressive solvents during the resist coating and liftoff steps. 200 nm of 495 A4 PMMA resist, followed by 400 nm of 950 C4 PMMA resist, both from Kayaku Advanced Materials, were spin-coated on the PVA/PI/PVA/$SiO_2$/Si stack. The contacts were patterned using a RAITH VOYAGER 100 electron beam lithography (EBL) tool, and after development in 1:3 MIBK/IPA, an additional DI water development step at 30°C for 15 seconds was done to develop the exposed PVA. The 100 nm of contact metal (Pt) was deposited at a rate of 0.7 Å $s^{-1}$ for 5 minutes, then 1 Å $s^{-1}$ until 100 nm thickness was

achieved, using an Angstrom Engineering Nexdep electron beam evaporation tool. Liftoff was done using ethanol at 70°C. The from spin coating the resist to liftoff were repeated as before to pattern the second contact metal (Ti) except this time reducing the resist curing temperature to 130°C for 90 seconds to avoid over-curing the PVA. After the contacts are patterned, The PI film with the patterned contacts is released in DI water at 95°C and then scooped up while floating in the DI water by a PMMA coated substrate. The as-grown $MoS_2$ on sapphire substrate [126] is spin coated with a 1.6 µm thick PI film and transferred onto the contacts using a surface energy assisted transfer technique. [49] The stack was then placed on a hotplate at 120°C to bake off the DI water between the PI encapsulant and PI substrate layers and annealed for 1 hr. The PI film with encapsulated devices was then placed in DI water to release the stack from the substrate to have the free standing flexible 2D PV. The steps are shown schematically in **Figure D.1**.

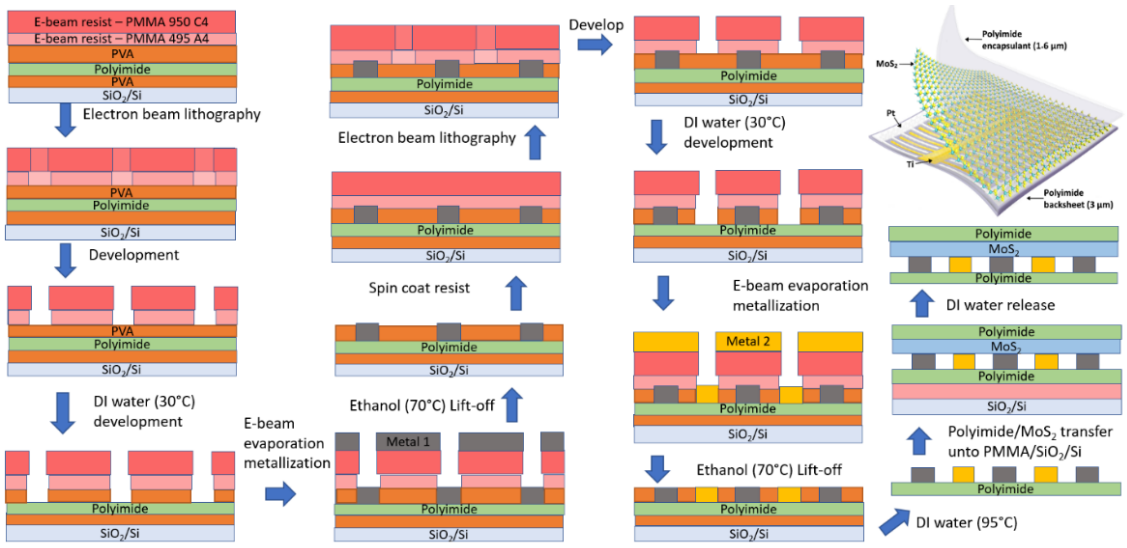


**Figure D.1:** Schematic showing fabrication steps for an ultra-thin and flexible encapsulated $MoS_2$ solar cell on NeXolve's CP1™ Polyimide substrate.

## D.2 ABSORPTION SPECTRA FOR MONOLAYER AND STACKED $MOS_2$ FILMS

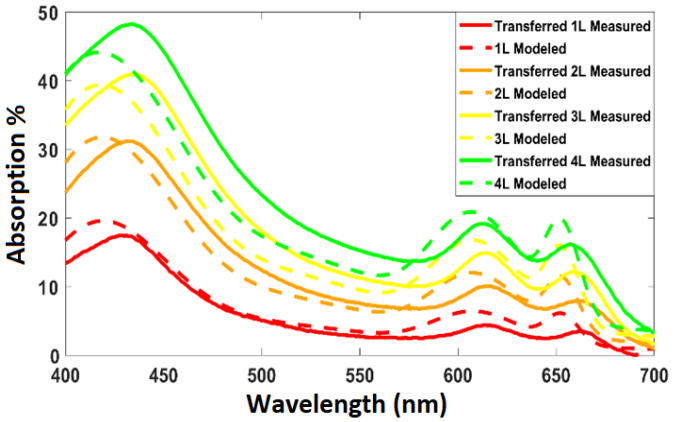


**Figure D.2:** Measured absorption spectra and computed absorption using the transfer matrix method for 1 to 4 stacked $MoS_2$ monolayers. Absorption is shown to increase additively as a result of layer-transfer-based stacking while maintaining the direct bandgap optical properties of $MoS_2$.

## D.3 TRANSFER MATRIX METHOD (TMM) SIMULATIONS

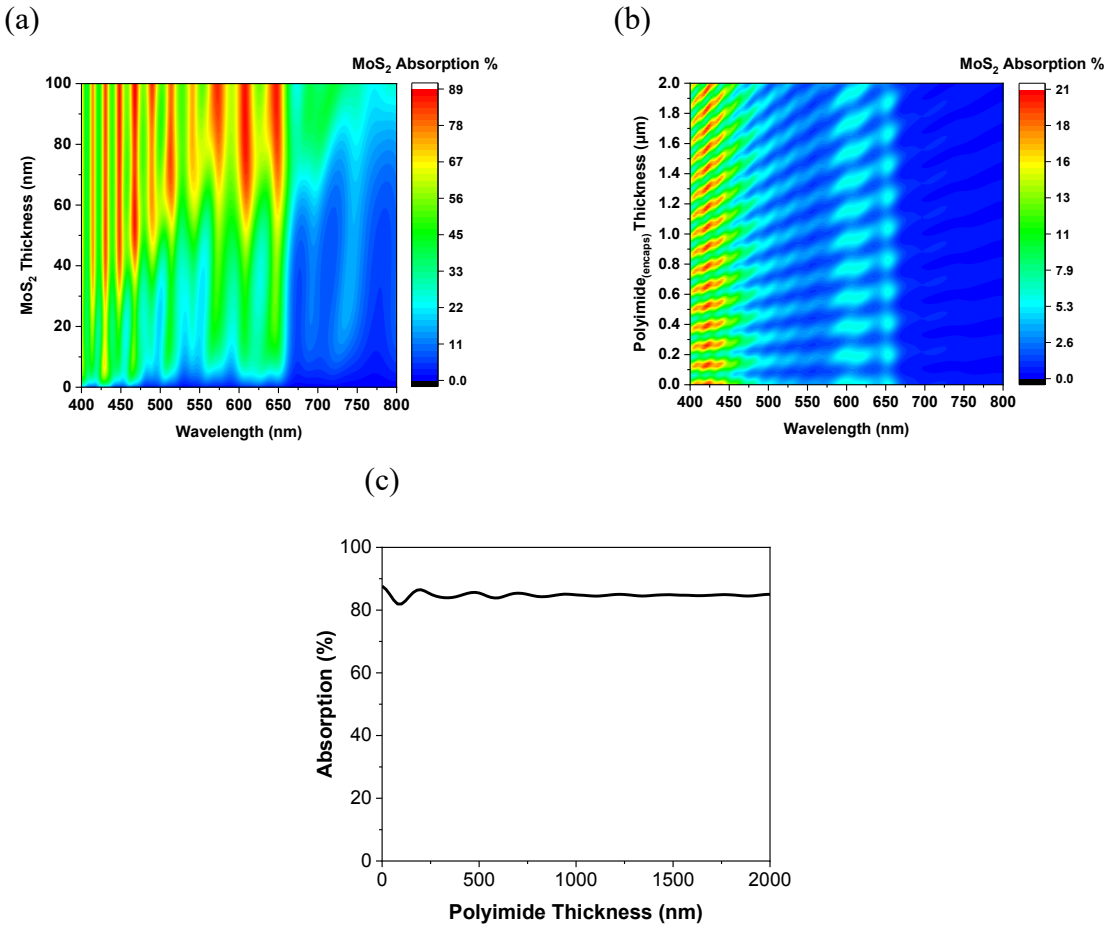


**Figure D.3:** a) Transfer matrix method (TMM) simulated absorption spectra for the $MoS_2$ layer at different $MoS_2$ thicknesses in the $PI_{encaps}/MoS_2/PI_{subs}$ stack. b) Simulated absorption spectra in the 0.65 nm thick $MoS_2$ layer vs polyimide encapsulant thickness, c) total absorption in the 100 nm thick $MoS_2$ absorber vs. polyimide encapsulant thickness.

## D.4 FLEXIBLE PV PERFORMANCE

PV devices were fabricated with three channel lengths: 1, 3, and 5 μm with 0.15 $mm^2$ active area. **Figure S4** shows the average $J_{SC}$, $V_{OC}$, fill factor, and efficiency vs channel length for a total of 9 devices of each channel length. A similar trend is observed where the device

performance is dependent on the spacing between each Ti and Pt finger. [62] Decreasing the channel size increases the current under the same illumination because of the short diffusion length of the carriers in the $MoS_2$. For the 1 μm channels, more of the generated carriers reach the contacts before recombination, leading to a larger $J_{SC}$. The average performance of the 1 μm channel devices before and after 10 bends at a 5 mm bend radius shown in Table 1, indicating the robustness and flexibility of these modules.

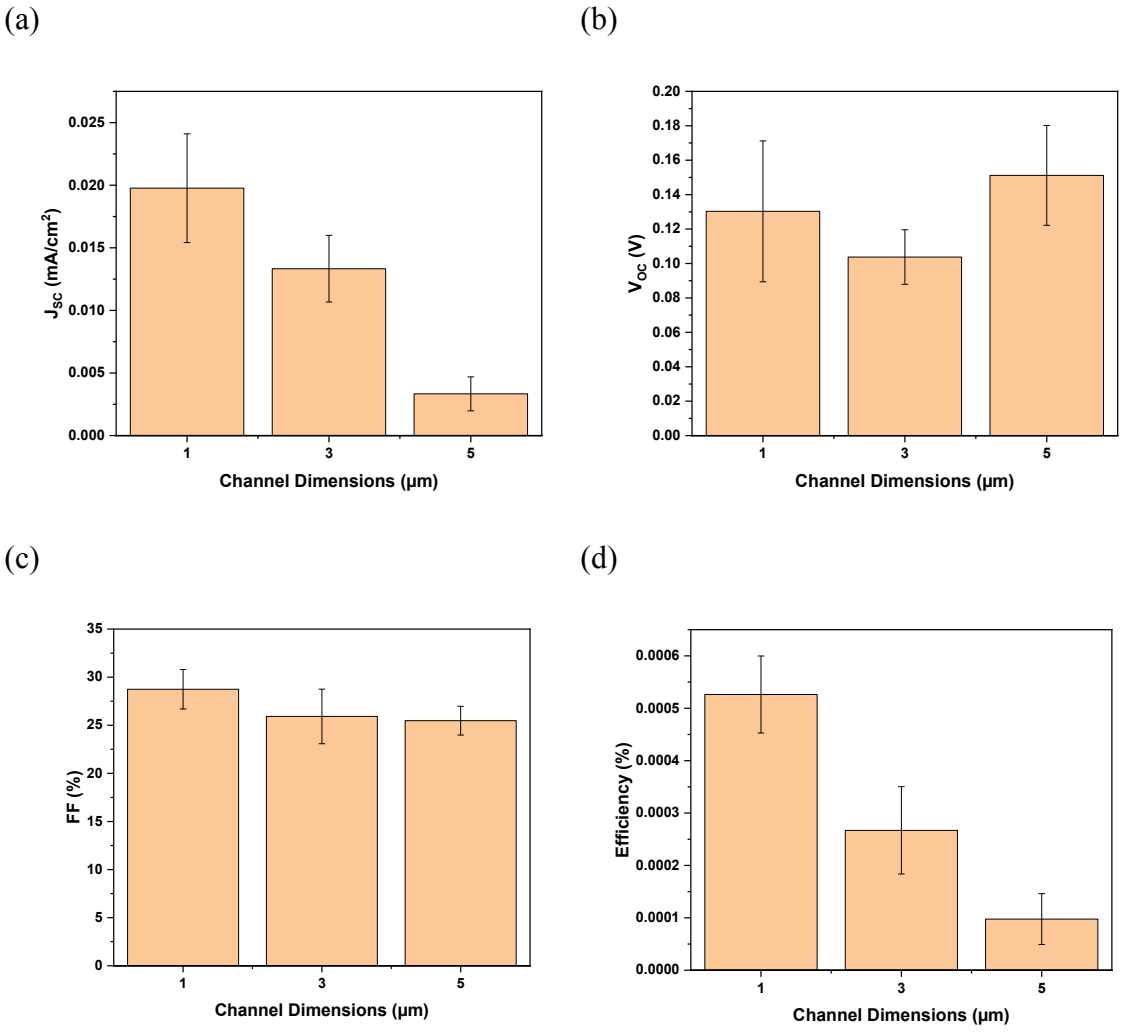


**Figure D.4:** a) $J_{SC}$, (b) $V_{OC}$, (c) fill factor and (d) efficiency vs channel length under 1 sun equivalent AM0 illumination.

# D.5 FLEXIBLE PV BENDING TEST

**Table D.5:** Average Performance of 1 μm channel devices before and after bending to a 5 mm bend radius.

| | Before bending | Average after 10 bends | Std |
|---|---|---|---|
| **$J_{SC}$ (mA/cm$^2$)** | 0.0208 | 0.02093 | 4.21769E-4 |
| **$V_{OC}$ (V)** | 0.1212 | 0.12171 | 0.00147 |
| **FF %** | 30.9 | 30.951 | 0.151 |
| **Efficiency %** | 5.77E-4 | 5.846E-4 | 2.12038E-5 |
| **Power Density (kW/kg)** | 0.0011 | 0.0011 | 4.07138E-5 |

# D.6 DEVICE CHARACTERISTICS AFTER BENDING TEST

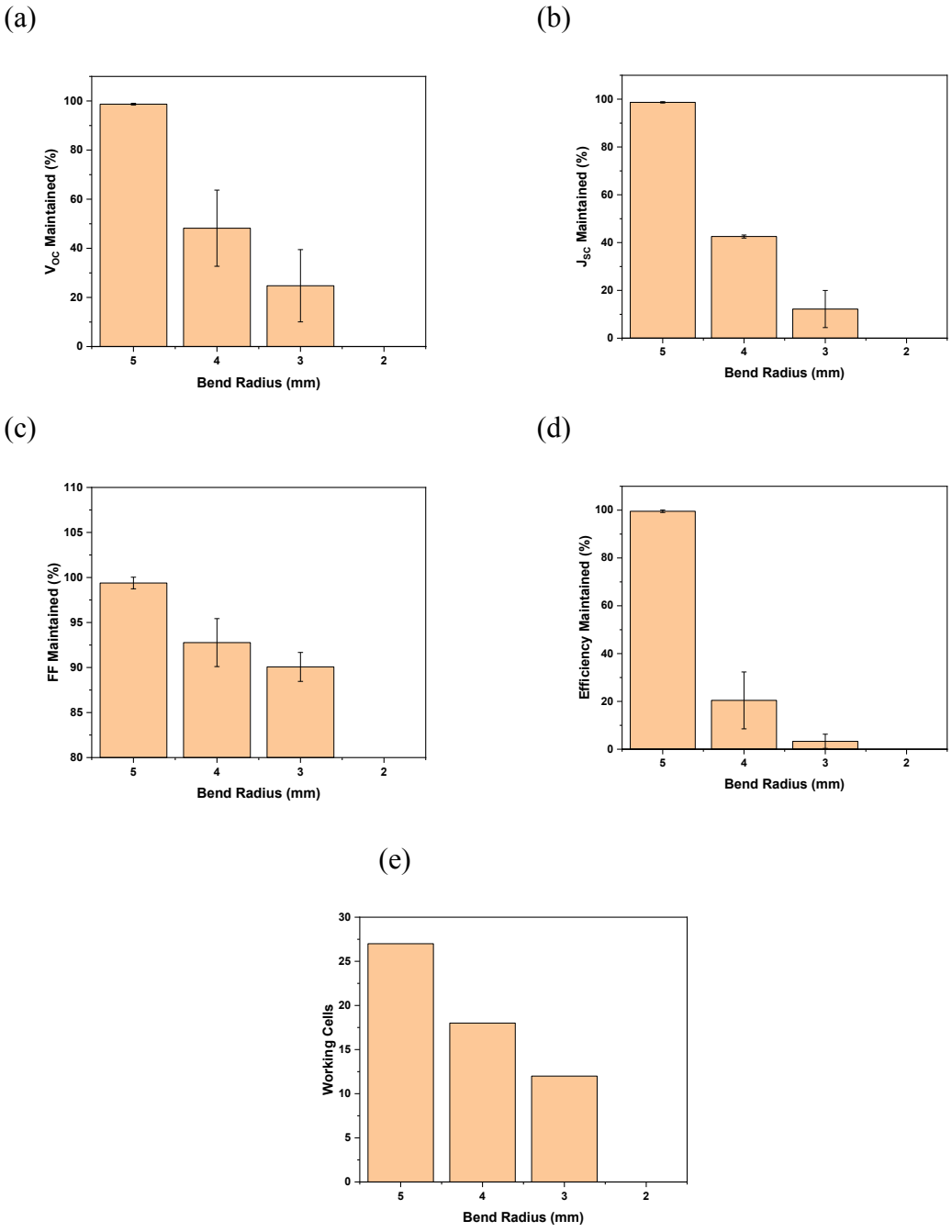


**Figure D.6:** a) $V_{OC}$ (b) $J_{SC}$, (c) fill factor, (d) efficiency maintained (relative to pre-bend performance) and number of working cells vs bending radius for 9 devices of each channel length under 1 sun equivalent AM0 illumination. 10 bends were applied at 5 mm bend radius, and 1 bend was applied at each of the subsequent smaller bend radii (performed in order of decreasing bend radius).

## D.7 OPTICAL IMAGE OF DEVICE AFTER BENDING TEST

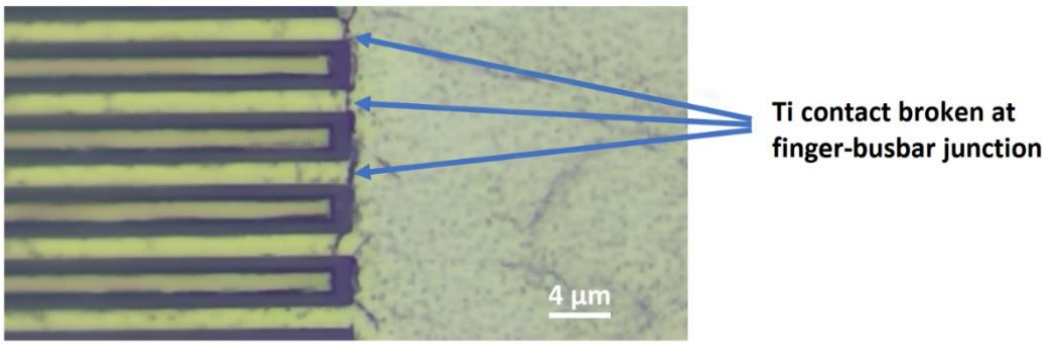


**Figure D.7:** Optical image of broken Ti contact fingers at the finger-busbar junction where stress concentration is expected during bending. This image shows a device with 1 µm channel length after a 2 mm bend

# D.8 DEVICE PERFORMANCE BEFORE AND AFTER RADIATION EXPOSURE

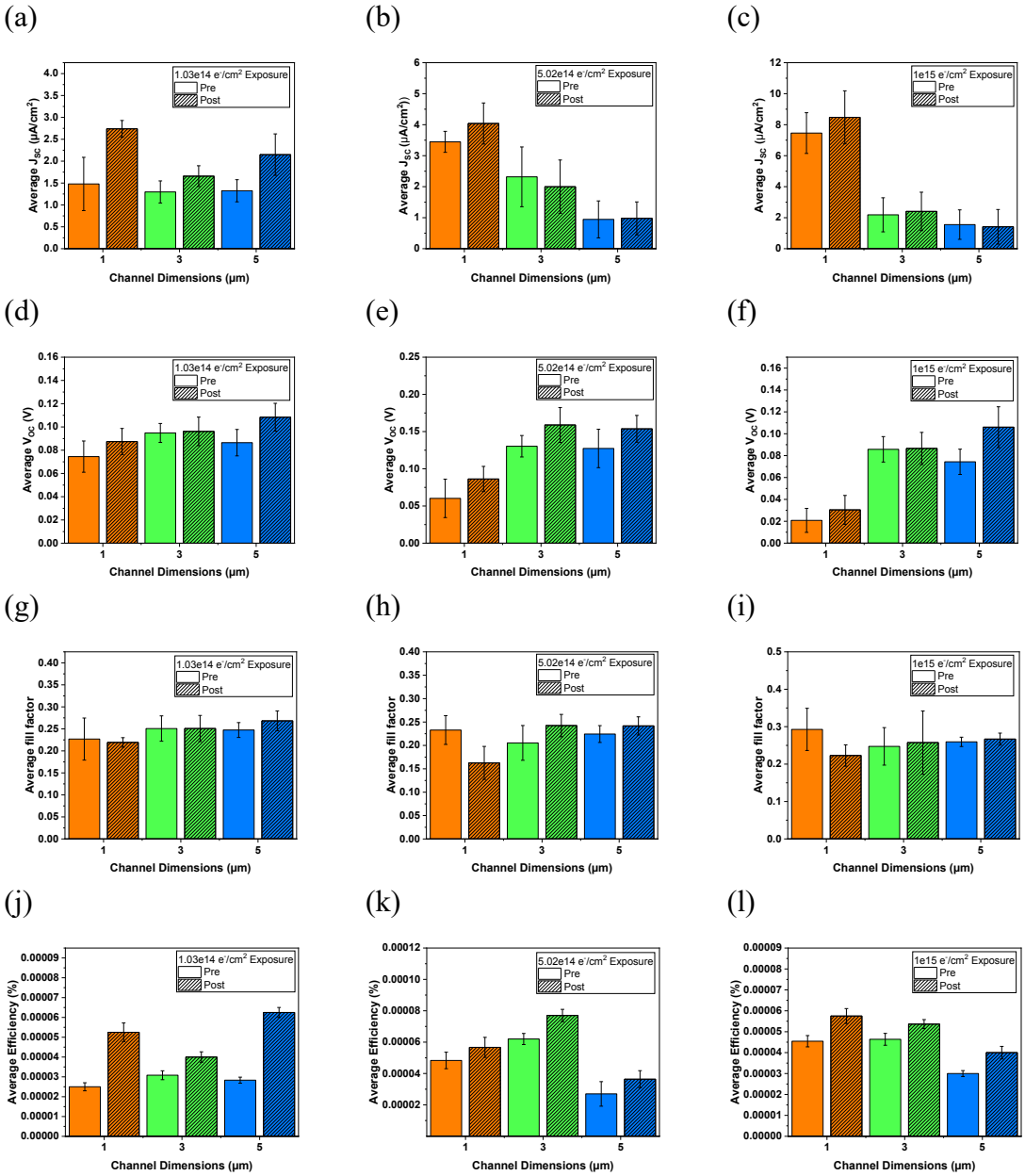


**Figure D.8:** (a-c) $J_{SC}$, (d-f) $V_{OC}$, (g-i) fill factor, and (j-l) efficiency for 6 devices of each channel length (average and standard deviation given) under 1 sun equivalent AM0 illumination both before and after 1.03e14, 5.02e14 and 1e15 $e^-/cm^2$ of 1 MeV electron radiation exposure.

## D.9 PHOTOLUMINESCENCE SPECTRA BEFORE AND AFTER RADIATION EXPOSURE

(a) (b)

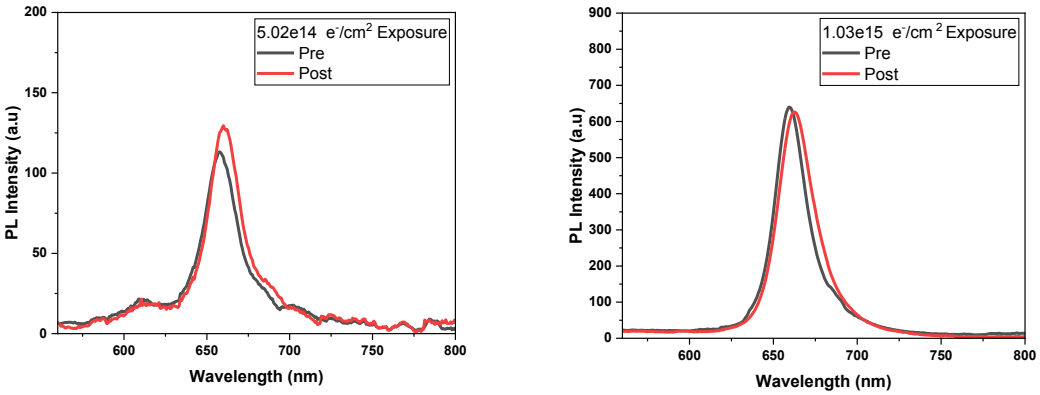


**Figure D.9:** Photoluminescence spectra of the as-grown monolayer $MoS_2$ film before and after a) 5.02e14 and b) 1e15 $e^-/cm^2$ of 1 MeV electron radiation exposure.

## D.10 RAMAN SPECTRA BEFORE AND AFTER RADIATION EXPOSURE

(a) (b)

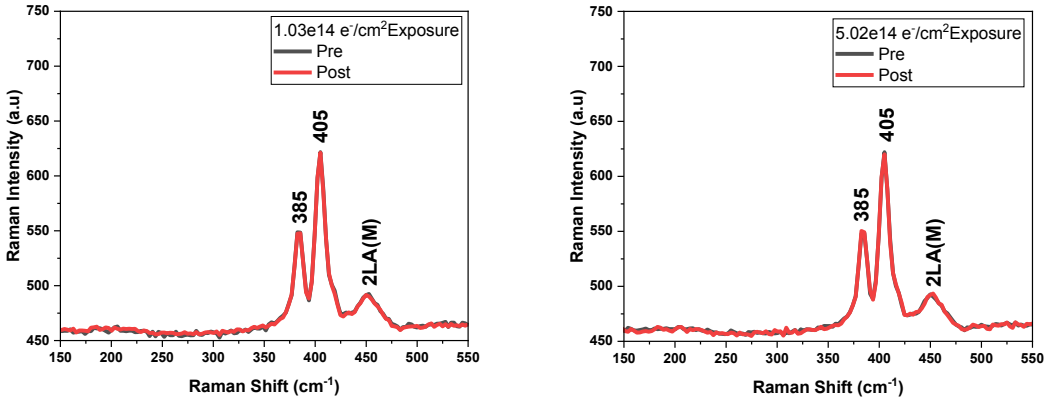


**Figure D.10:** Raman spectra of the monolayer $MoS_2$ film before and after a) 1.03e14 and b) 5.02e14 $e^-/cm^2$ of 1 MeV electron radiation exposure showing no difference in peak locations pre and post exposure.

# D.11 MASTER TECHNO-ECONOMIC ANALYSIS PARAMETERS

| **Table D.11:** Master Techno-Economic Analysis Parameters. | | |
|---|---|---|
| **Overall dimensions of each triangular array** | | |
| **Base** | 118.8 | cm |
| **Height** | 52.5 | cm |
| **Cell Parameters** | | |
| **Cell Length** | 3.2 | cm |
| **Cell Width** | 3.2 | cm |
| **Cell Thickness** | 0.078 | microns |
| **Cell Density** | 5.06 | g/cm^3 |
| **Cell Fill Factor** | 0.604 | |
| **Cell $V_{OC}$** | 0.7 | Volts |
| **Cell Jsc** | 16.614 | mA/cm^2 |
| **Cell Vmpp** | 0.544 | Volts |
| **Cell Jmpp** | 12.911 | mA/cm^2 |
| **Cell Count/String** | 51 | |
| **Parallel Strings per Array** | 6 | |
| **Array Parameters** | | |
| **Backsheet Thickness** | 3 | microns |
| **Backsheet Mass Density** | 1.54 | g/cm^3 |
| **Top Coating Thickness** | 1.6 | microns |
| **Top Coating Mass Density** | 1.54 | g/cm^3 |
| **Gold Wire density** | 19.3 | g/cm^3 |
| **Wire Length** | 700 | cm |
| **Wire Width** | 2 | mm |
| **Wire Thickness** | 3 | microns |
| **Array Cell Height** | 15 | cells |
| **Array Cell Width** | 36 | cells |
| **Cell Vertical Spacing** | 3 | mm |
| **Cell Horizontal Spacing** | 1 | mm |
| **System Parameters** | | |
| **Array Count** | 4 | |
| **Arrays in Series** | 0 | |
| **Arrays in Parallel** | 4 | |

# D.12 2D SOLAR CELL COMPUTATIONS

| **Table D.12:** Cell Computations. | | |
|---|---|---|
| **Area per Cell** | 10.24 | cm^2 |
| **Volume per Cell** | 7.99E-05 | cm^3 |
| **Total # of Cells** | 1224 | |
| **Cell Current** | 132.22 | mA |
| **Cell Voltage** | 0.544 | V |
| **Cell Power** | 0.072 | W |
| **Mass per cell** | 0.87 | mg |
| **Sulfur Precursor Mass** | 50 | mg |
| **MoO3 Precursor Mass** | 1 | mg |
| **Finger Volume** | 3.19E-05 | cm^3 |
| **Busbar Volume** | 4.02E-06 | cm^3 |
| **Platinum Density** | 21450 | mg/cm^3 |
| **Titanium Density** | 4506 | mg/cm^3 |
| **Platinum Mass** | 3.86E-01 | mg |
| **Titanium Mass** | 8.10E-02 | mg |

# D.13 2D PV ARRAY COMPUTATIONS

| **Table D.13:** Array Computations. | | |
|---|---|---|
| | | |
| **Base** | 118.8 | cm |
| **Height** | 52.5 | cm |
| **Area** | 3118.5 | $cm^2$ |
| **Side length** | 79.276 | cm |
| | | |
| **Backsheet** | | |
| **Area** | 3118.5 | cm^2 |
| **Volume** | 0.93555 | cm^3 |
| **Mass** | 1.4407 | g |
| | | |
| **Top Coating** | | |
| **Area** | 3118.5 | cm^2 |
| **Volume** | 0.49896 | cm^3 |
| **Mass** | 0.76840 | g |
| | | |
| **Electrical** | | |
| **Voltage** | 27.75 | V |
| **Current** | 0.7933 | A |
| **Power** | 22.01 | W |
| **Wire volume** | 0.042 | cm^3 |
| **Wire mass** | 0.8106 | grams |
| | | |
| **Total Array Mass** | 3.286 | grams |

# D.14 COMMERCIAL PERC PARAMETERS

**Table D.14:** Sunpower P-Series Commercial PERC.

| Part # | **SPR-P6-400-COM-XS** [120] | | |
|---|---|---|---|
| | | | |
| **Specification** | **Value** | **Metric** | **Comment** |
| | **Dimensions** | | |
| Weight | 21 | kg | |
| Length | 1.092 | m | |
| Width | 1.808 | m | |
| Area | 1.974336 | m^2 | |
| | | | |
| | **AM1.5** | | |
| Voc | 36 | V | |
| Isc | 14.36 | A | |
| Eff | 20.30% | | |
| Nom. Power | 400 | W | |
| Power cost (panel only) | $ 0.411 | $/W | NREL[163] |
| | | | |
| | **AM0** | | |
| Nom. Power | 546.44 | W | |
| Specific Power Density | 26.021 | W/kg | |
| Power cost (material only) | $ 0.30 | $/W | AM0 adjusted |
| Launch Cost | $ 2,720.00 | $/kg | Falcon 9 [151] |
| **Total Power Cost** | $ 104.83 | $/W | |
| | | | |
| Material Cost | $ 164.40 | $/module | |
| | | | |
| **Cost by area** | $ 21,238.94 | $/m^2 | |

# D.15 FLEXIBLE 2D PV BILL OF MATERIALS

**Table D.15:** 2D PV Bill of Materials.

| | Value | Metric | Total Cost | Unit |
|---|---|---|---|---|
| | | | | |
| **Total** | | | | /unit |
| | | | | |
| **Cell** | | | $ 0.7074 | $/cell |
| Molybdenum trioxide (MoO3) | 0.000875 | $/mg | | |
| Sulfur Powder | 0.00134 | $/mg | | |
| Platinum | 0.03 | $/mg | | |
| Titanium | 0.000138 | $/mg | | |
| | | | | |
| **Array** | | | $ 52.71 | $/array |
| CP1 Backsheet | 0.0165 | $/cm^2 | | |
| Top Coating | 1.412 | $/gram | | |
| Wiring | 0.206 | $/cm | | |
| | | | | |
| **Launch** | | | | |
| Falcon 9 [151] | $ 2,720.00 | kg | $ 8.94 | launch cost/array |
| | | | | |
| **Totals** | | | | |
| Array Cost to Orbit | $ 278.11 | $ | | |
| Array Power Cost | $ 12.64 | $/W | | |

# D.16 TEMPERATURE PROFILE DURING RADIATION TEST

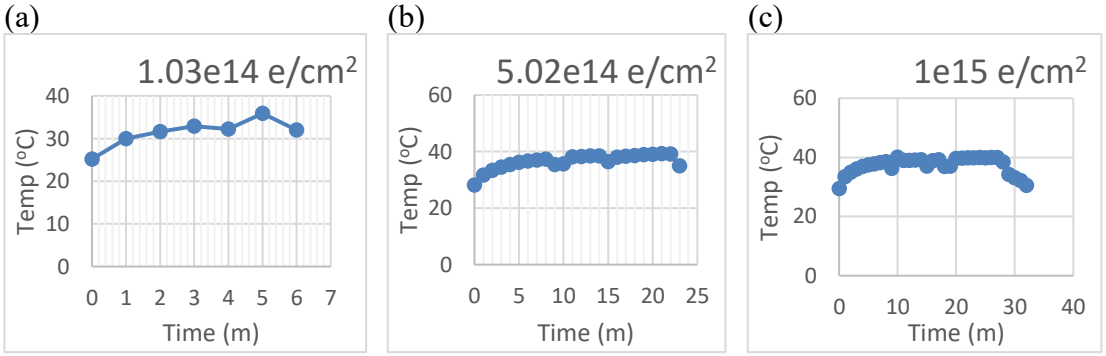


**Figure D.16:** Temperature profile of the testbed during radiation exposure for a) 1.03e14, b) 5.02e14 and c) 1e15 $e^-/cm^2$ of 1MeV electron radiation exposure.

# APPENDIX E

# SUPPLEMENTARY INFORMATION FOR CHAPTER 5

## E.1 CONTACTS BEFORE AND AFTER TRANSFER

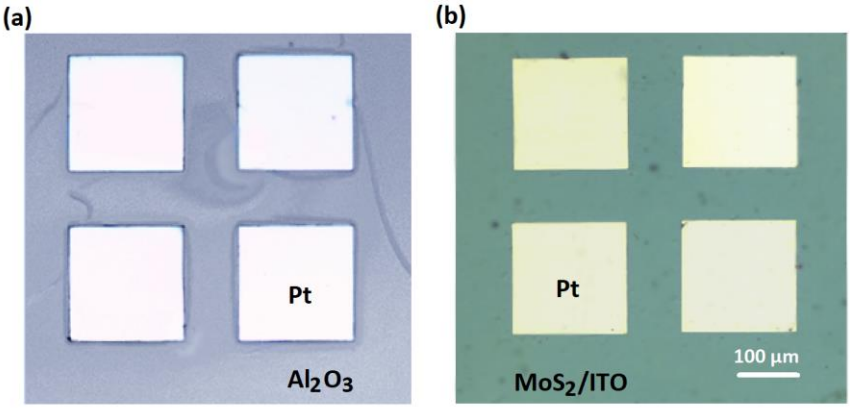


**Figure E.1:** Pt contacts on sapphire substrate (a) before transfer and (b) after transfer onto the $MoS_2$ film on the ITO contact.

## E.2 LIFETIME EXTRACTION FROM TRPL MEASUREMENTS

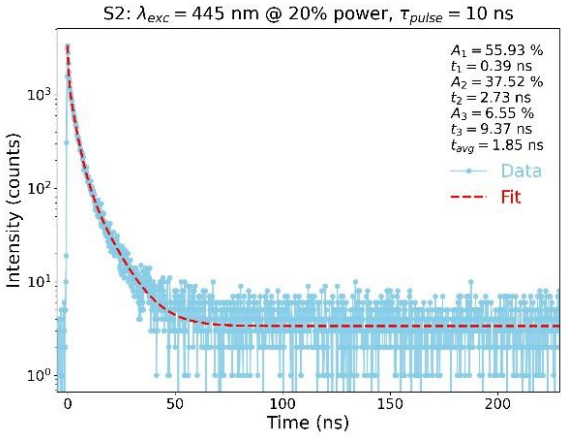


**Figure E.2:** Lifetime results from time resolved photoluminescence lifetime measurements of as-grown monolayer $MoS_2$ on $Al_2O_3$ substrate.

# E.3 COMPUTED BAND STRUCTURES

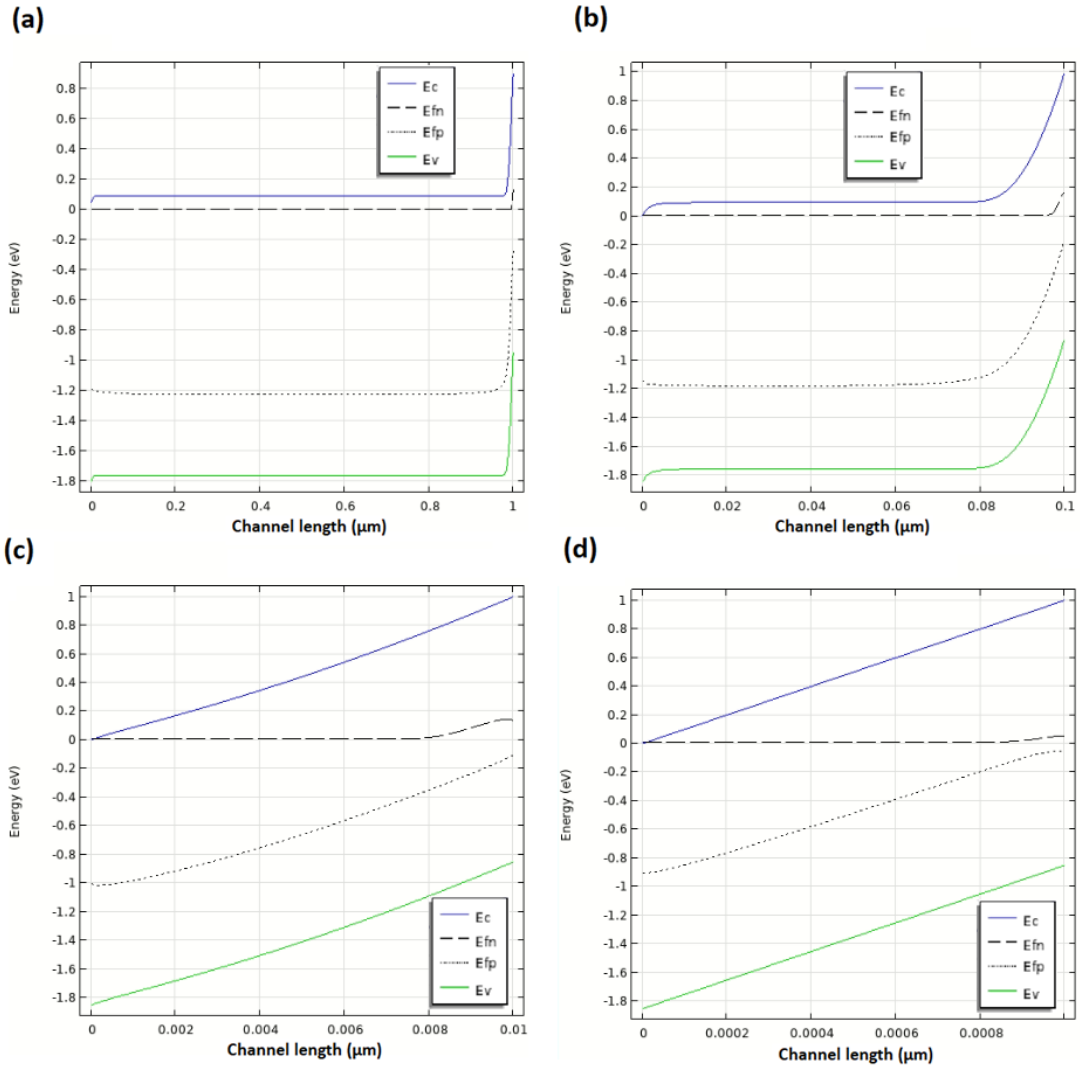


**Figure E.3:** Computed band structures for lateral ITO(left)/$MoS_2$/Pt(right) device based on monolayer $MoS_2$ films with 1, 0.1, 0.01 and 0.001 μm channels between metal contact fingers..

# E.4 GENERATION AND RECOMBINATION RATES IN LATERAL AND VERTICAL DEVICES

The generation and recombination profiles for 100 nm thick $MoS_2$ film vertical and lateral transport PV devices are shown in **Figure E.4a** and **b** respectively. The constant generation rate for the lateral device is calculated by integrating the thickness dependent generation profile to obtain the generation rate per area ($1/cm^2*s$) of the device, then dividing by the thickness of the device. This gives the generation rate in the film per unit volume ($1/cm^3*s$) at every point along the x-y plane between the ITO and Pt contacts.

(a) (b)

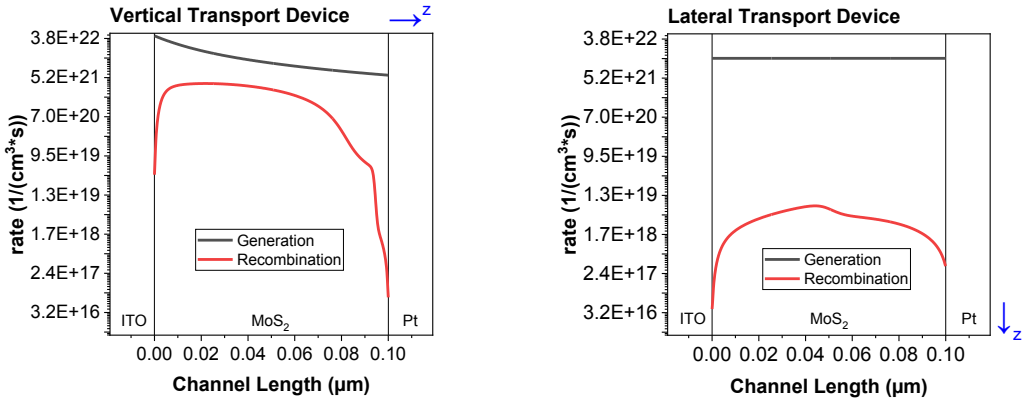


**Figure E.4:** Generation and recombination rates rates in (a) vertical and (b) lateral ITO/$MoS_2$/Pt PV devices with a 100 nm thick $MoS_2$ film.

## E.5 RECOMBINATION RATES VS CHANNEL LENGTH IN LATERAL DEVICES

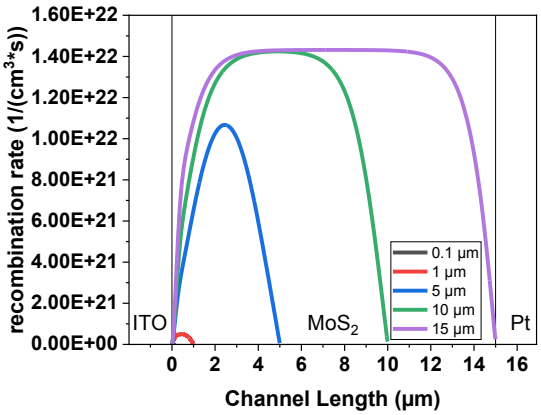


**Figure E.5:** Calculated recombination rate vs channel length in 0.1, 1, 5, 10 and 15 µm channel length lateral ITO/$MoS_2$/Pt PV devices.

## E.6 J-V CHARACTERISTICS FOR ITO/$MOS_2$/PT $MOS_2$ PV DEVICES

(a) (b)

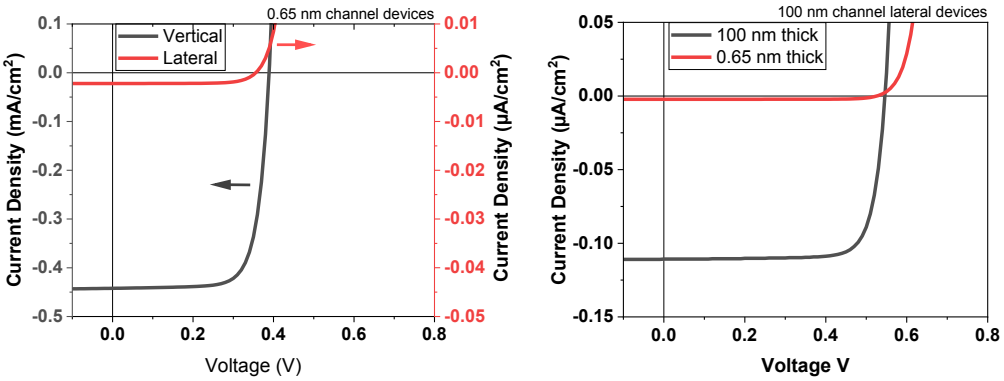


**Figure E.6:** Simulated J-V characteristics of (a) a 0.65 nm channel length lateral and vertical ITO/$MoS_2$/Pt PV device using a 0.65 nm thick $MoS_2$ (b) J-V characteristics for lateral ITO/$MoS_2$/Pt PV device of 100 nm channel length, with 100 and 0.65 nm thick $MoS_2$ films.

## E.7 J-V PLOTS VS CHANNEL LENGTH AND FILM THICKNESS FOR VERTICAL AND LATERAL ITO/$MOS_2$/PT PV DEVICES

(a)

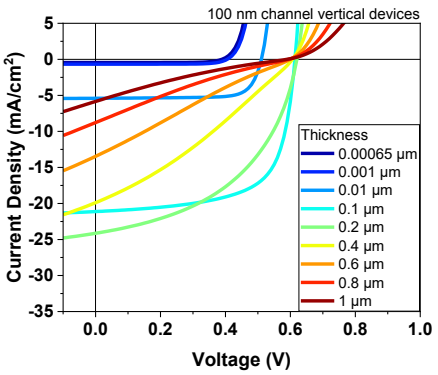


(b)

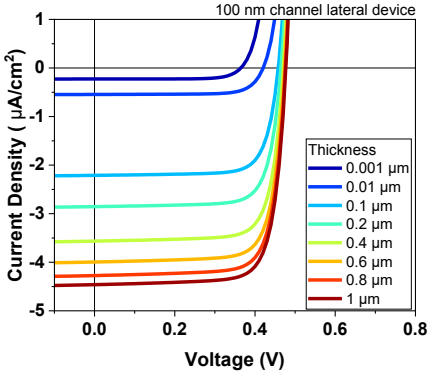


(c)

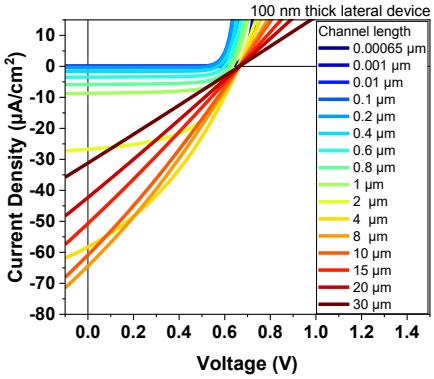


**Figure E.7:** Simulated J-V characteristics of (a) vertical ITO/$MoS_2$/Pt PV devices at different $MoS_2$ film thicknesses (b) lateral ITO/$MoS_2$/Pt PV devices at different $MoS_2$ film thicknesses (c) lateral ITO/$MoS_2$/Pt PV device at different channel lengths, with a 100 nm thick $MoS_2$ film.

# E.8 FABRICATION PROCESS FOR VERTICAL TRANSPORT ITO/$MOS_2$/PT PV DEVICES

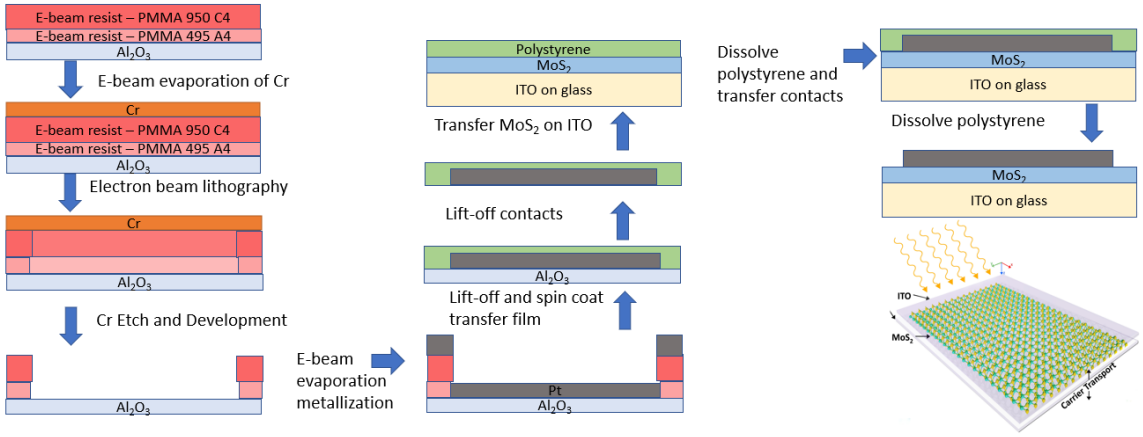


**Figure E.8:** Schematic showing fabrication steps to transfer metal contacts onto $MoS_2$ on an ITO/glass substrate for a vertical 2D $MoS_2$ based photovoltaic device.

# APPENDIX F

# FABRICATION DETAILS

## F.1 PHOTOTRANSISTOR ON PATTERNED AS-GROWN $MOS_2$ FILMS ON $AL_2O_3$ SUBSTRATE

1. ***Spin coat Resist on as-grown $MoS_2/Al_2O_3$ substrate.***

    a. **400 nm thick PMMA 950 C4:**
    1000 rpm for 15 seconds → 4000 rpm for 45 seconds, bake at 180 C for 90 seconds.

2. ***Deposit Cr layer on PMMA 950 C4/$MoS_2/Al_2O_3$ substrate.***

    a. **Electron Beam evaporation of 10 nm Cr conductive layer (Angstrom Engineering Nexdep):**
    Thermal evaporation via e-beam at 1A/s using sweeping pattern,
    Chamber Pressure < $3.6 \times 10^{-6}$ mbar,

3. ***Electron Beam Lithography Alignment Marks Patterning.***

    a. **EBL parameters (RAITH VOYAGER 100)**
        - Current mode: 50KV High current aperture 70
        - Beam Current ~ 26200 nA
        - Write field size 500 µm, Area Step Size 0.0095 µm, Area Line Spacing 0.0100 µm, Area Dwell time 0.000020 ms
        - Clearing Dose ~ 550 $\mu C/cm^2$

    b. **Focusing and Alignment**
        - At nano structures, 1.95 Field of View, do Beam Focus → Beam Stigmator → Beam Focus.
        - At nano structures, 1.95 Field of View, do Field Focus.
        - At checkered structures, 7.81Field of View, do Field Position Coarse (FOM < 140) → Field Position Fine (FOM < 50) → Field Position Final (FOM < 14).

    c. **Start write**

4. ***Development.***

    a. **Cr conductive layer etch**
    Shake lightly while submerged in Cr etchant for 10s → DI for 5s.

    b. **Exposed PMMA Removal:**
    Shake lightly while submerged in MIBK:IPA 1:3 for 40s → IPA for 5s.

5. ***Deposit Ti alignment marks on $MoS_2/Al_2O_3$ substrate.***

    a. **Electron Beam evaporation of 55 nm Ti layer (Angstrom Engineering Nexdep):**
    Thermal evaporation via e-beam at 1A/s using dot pattern, Chamber Pressure < $3.6 \times 10^{-6}$ mbar

6. ***Lift-off.***

    a. **Ti Alignment Mark:**
    Submerge stack in Acetone until all metal is lifted off → IPA for 5s → DI for 5s.

7. ***Spin coat Resist on as-grown $MoS_2/Al_2O_3$ substrate.***

    a. **200 nm thick PMMA 495 A4:**
    1000 rpm for 15 seconds → 4000 rpm for 45 seconds, bake at 180 C for 90 seconds.
    b. **400 nm thick PMMA 950 C4:**
    1000 rpm for 15 seconds → 4000 rpm for 45 seconds, bake at 180 C for 90 seconds.

8. ***Deposit Cr layer on PMMA 950 C4/PMMA495 A4/$MoS_2/Al_2O_3$ substrate.***

    a. **Electron Beam evaporation of 10 nm Cr conductive layer.**
    Thermal evaporation via e-beam at 1A/s using sweeping pattern, Chamber Pressure < $3.6 \times 10^{-6}$ mbar,

9. ***Electron Beam Lithography for $MoS_2$ film Patterning.***

    a. **Repeat step 3a and b**
    b. **3-point Alignment**
    Align to Ti alignment marks
    c. **Start write**

10. ***Development for $MoS_2$ film Patterning.***

    a. **Repeat step 4**

11. ***Etch $MoS_2$***

    a. **Cr etchant**
    Shake lightly while submerged in Cr etchant for 15s → DI for 5s. Repeat if exposed $MoS_2$ is not completely etched.

*12. **Resist removal.***

a. **Dissolve resist layers:**
   Submerge stack in Acetone until all resist is dissolved → IPA for 5s → DI for 5s.

*13. **Contact Patterning on $MoS_2/Al_2O_3$ substrate.***

a. **Repeat step 7 and 8**
b. **Repeat steps 3a and b**
c. **3-point Alignment**
   Align to Ti alignment marks
d. **Start write**

*14. **Deposit Contacts on $MoS_2/Al_2O_3$ substrate.***

a. **Electron Beam evaporation of 5/55 nm Au/Ti**
   Thermal evaporation via e-beam at 1A/s using sweeping pattern, Chamber Pressure < $3.6 \times 10^{-6}$ mbar

*15. **Lift-off.***

a. **Contacts:**
   Submerge stack in Acetone until all metal is lifted off → IPA for 5s → DI for 5s.

# F.2 BACK-GATED FIELD EFFECT TRANSISTOR ON TRANSFERRED $MOS_2$ FILMS ON $SIO_2$ SUBSTRATE

1. ***Transfer film on $SiO_2$/Si substrate.***

    **a. Transfer film:**
    Use surface energy assisted technique.
    Ensure carrier film is completely dissolved. Do multiple dissolving steps if needed.

2. ***Spin coat Resist on transferred $MoS_2$/$SiO_2$/Si substrate.***

    **a. 200 nm thick PMMA 495 A4:**
    1000 rpm for 15 seconds → 4000 rpm for 45 seconds, bake at 180 C for 90 seconds.
    **b. 400 nm thick PMMA 950 C4:**
    1000 rpm for 15 seconds → 4000 rpm for 45 seconds, bake at 180 C for 90 seconds.

3. ***Electron Beam Lithography Contact Patterning.***

    **a. EBL parameters (RAITH VOYAGER 100)**
    - Current mode: 50KV High current aperture 70
    - Beam Current ~ 26200 nA
    - Write field size 500 µm, Area Step Size 0.0095 µm, Area Line Spacing 0.0100 µm, Area Dwell time 0.000020 ms
    - Clearing Dose ~ 550 $\mu C/cm^2$

    **b. EBL parameters (RAITH VOYAGER 100)**
    - At nano structures, 1.95 Field of View, do Beam Focus → Beam Stigmator → Beam Focus.
    - At nano structures, 1.95 Field of View, do Field Focus.
    - At checkered structures, 7.81Field of View, do Field Position Coarse (FOM < 140) → Field Position Fine (FOM < 50) → Field Position Final (FOM < 14)

    **c. Start write**

4. ***Development***

    **a. Exposed PMMA Removal**
    Shake lightly while submerged in MIBK:IPA 1:3 for 40s → IPA for 5s

5. ***Gate Patterning***

   **a. Scratch through PMMA/$SiO_2$ layers with a diamond scribe**
   Be sure to get beneath the Si)2 layer to expose highly conductive Si layer.

6. ***Deposit Ti alignment marks on $MoS_2/Al_2O_3$ substrate.***

   **a. Electron Beam evaporation of 5/55 nm Au/Ti contacts**
   Thermal evaporation via e-beam at 1A/s using sweeping pattern, Chamber Pressure < $3.6 \times 10^{-6}$ mbar

7. ***Lift-off.***

   **a. Au/Ti Gate, Source and Drain Contacts:**
   Submerge stack in Acetone until all metal is lifted off → IPA for 5s → DI for 5s.

# F.3 2D $MOS_2$ PV DEVICE ON FLEXIBLE POLYIMIDE SUBSTRATE

1. ***Spin coat PVA film on $SiO_2$/Si substrate.***

   a. **Coat substrate with PVA from 10% polyvinyl alcohol in DI water solution:**

   500 rpm for 15 seconds → 1200 rpm for 45 seconds, bake at 180 C for 90 seconds.

2. ***Transfer polyimide (PI) film onto PVA on $SiO_2$/Si substrate.***

   a. **Cut the polyimide substrate on handler to desired size.**

   A pair of scissors works best.

   b. **Use a wide tweezer to transfer the polyimide film onto the substrate.**

   c. **Place on a hot plate at 120 C and use a soft object to smoothen out the film.**

   I found the soft tip of a stylus pen to work well. Always ensure to do a solvent clean of the stylus tip to ensure its clean.

3. ***Spin coat second PVA film on the stack.***

   b. **Use the same process in step 1.**

4. ***Spin coat Resist on transferred PVA/PI/PVA/$SiO_2$/Si substrate.***

   a. **200 nm thick PMMA 495 A4:**

   1000 rpm for 15 seconds → 4000 rpm for 45 seconds, bake at 180 C for 90 seconds.

   b. **400 nm thick PMMA 950 C4:**

   1000 rpm for 15 seconds → 4000 rpm for 45 seconds, bake at 180 C for 90 seconds.

5. ***Electron Beam Lithography Contact Patterning.***

   a. **EBL parameters (RAITH VOYAGER 100)**
      - Current mode: 50KV High current aperture 70
      - Beam Current ~ 26200 nA
      - Write field size 500 µm, Area Step Size 0.0095 µm, Area Line Spacing 0.0100 µm, Area Dwell time 0.000020 ms
      - Clearing Dose ~ 550 $\mu C/cm^2$

   b. **EBL parameters (RAITH VOYAGER 100)**
      - At nano structures, 1.95 Field of View, do Beam Focus → Beam Stigmator → Beam Focus.
      - At nano structures, 1.95 Field of View, do Field Focus.

- At checkered structures, 7.81Field of View, do Field Position Coarse (FOM < 140) → Field Position Fine (FOM < 50) → Field Position Final (FOM < 14)

**c. Start write.**

***6. Development***

**a. Exposed PMMA Removal**
Shake lightly while submerged in MIBK:IPA 1:3 for 40s → IPA for 5s

**b. Exposed PVA Removal**
Submerged in 30 C DI water for 10s. If contact pattern is affected, reduce temperature. The PVA curing is critical for this step so you may need to optimize this step for better results.

***7. Deposit Pt Contact on PI***

**a. Electron Beam evaporation of 100 nm Pt layer (Angstrom Engineering Nexdep):**
Thermal evaporation via e-beam at 0.7 Å/s for first 5 nm, then at 1 Å/s using sweeping pattern, Chamber Pressure < 3.6 x $10^{-6}$ mbar

***8. Lift-off***

**a. Pt Contacts:**
Submerge stack in Ethanol at 70 C until all metal is lifted off → IPA for 5s → DI for 5s.

**b. Sonication**
Sonication in IPA for 5 seconds might be needed for better liftoff. Do not use water in this step due to the hydrophobic nature of the PI film.

***16. Electron Beam Lithography for Ti contact Patterning.***

**a. Repeat step 4a and b**
**b. Repeat steps 5a and b**
**c. 3-point Alignment**
Align to Pt alignment marks
**d. Start write.**

***17. Development for Ti Patterning.***

**a. Repeat step 6**

*9. **Deposit Ti Contact on PI***

**a. Electron Beam evaporation of 100 nm Ti layer (Angstrom Engineering Nexdep):**

Thermal evaporation via e-beam at 0.7 Å/s for 5 nm, then 1 Å/s using a dot pattern, Chamber Pressure < 3.6 x $10^{-6}$ mbar

*10. **Lift-off***

**b. Ti Contacts:**

Submerge stack in Ethanol at 70 C until all metal is lifted off → IPA for 5s → DI for 5s.

**c. Sonication**

Sonication in IPA for 5 seconds might be needed for better liftoff. Do not use water in this step due to the hydrophobic nature of the PI film.

*11. **Release PI and Contacts from $SiO_2$/Si substrate.***

**a. Elevated temperature DI water release**

Release in 95 C DI water. If the PVA is over cured, higher temperature might be required to release.

**a. Transfer PI with contacts onto a separate $SiO_2$/Si substrate.**

Scoop up the floating stack with a substrate then bake off the DI water slowly at 80 C. Ensure that the stack is stretched out on the new substrate.

*12. **Transfer PI encapsulant/$MoS_2$ film onto contacts/PI/$SiO_2$/Si substrate.***

**a. Spin coat polyimide film on as-grown $MoS_2$ to desired encapsulant thickness.**

1.6 μm thick spin recipe is 1000 rpm 15 seconds →12000 rpm for 45 seconds.

**b. Transfer film:**

Use surface energy assisted technique.

*13. **Anneal the PV devices.***

**d. Initial bake at 80 C to remove trapped water encapsulated between the PI layers then anneal at 120 C for 30 minutes.**

*14. **Release.***

**b. Release Cells in DI water.**

.

# F.4 VERTICAL ARCHITECTURE 2D PV DEVICE WITH ITO CONTACT

2. ***Spin coat Resist on as-grown $MoS_2/Al_2O_3$ substrate.***

   **a. 200 nm thick PMMA 495 A4:**
   1000 rpm for 15 seconds → 4000 rpm for 45 seconds, bake at 180 C for 90 seconds.
   **b. 400 nm thick PMMA 950 C4:**
   1000 rpm for 15 seconds → 4000 rpm for 45 seconds, bake at 180 C for 90 seconds.

3. ***Deposit Cr layer on PMMA 950 C4/$MoS_2/Al_2O_3$ substrate.***

   **a. Electron Beam evaporation of 10 nm Cr conductive layer (Angstrom Engineering Nexdep):**
   Thermal evaporation via e-beam at 1A/s using sweeping pattern,
   Chamber Pressure < 3.6 x $10^{-6}$ mbar,

4. ***Electron Beam Lithography Alignment Marks Patterning.***

   **a. EBL parameters (RAITH VOYAGER 100)**
   - Current mode: 50KV High current aperture 70
   - Beam Current ~ 26200 nA
   - Write field size 500 µm, Area Step Size 0.0095 µm, Area Line Spacing 0.0100 µm, Area Dwell time 0.000020 ms
   - Clearing Dose ~ 550 µC/$cm^2$

   **b. Focusing and Alignment**
   - At nano structures, 1.95 Field of View, do Beam Focus → Beam Stigmator → Beam Focus.
   - At nano structures, 1.95 Field of View, do Field Focus.
   - At checkered structures, 7.81Field of View, do Field Position Coarse (FOM < 140) → Field Position Fine (FOM < 50) → Field Position Final (FOM < 14).

   **c. Start write**

5. ***Development.***

   **a. Cr conductive layer etch**
   Shake lightly while submerged in Cr etchant for 10s → DI for 5s.
   **b. Exposed PMMA Removal:**
   Shake lightly while submerged in MIBK:IPA 1:3 for 40s → IPA for 5s.

6. ***Deposit Pt contact on $Al_2O_3$ substrate.***

    a. **Electron Beam evaporation of 100 nm Pt conductive layer (Angstrom Engineering Nexdep):**
    Thermal evaporation via e-beam at 1A/s using sweeping pattern, Chamber Pressure < $3.6 \times 10^{-6}$ mbar

7. ***Lift-off.***

    a. **Pt Contacts:**
    Submerge stack in Acetone until all metal is lifted off → IPA for 5s → DI for 5s.

8. ***Transfer $MoS_2$ film on ITO/Glass substrate.***

    a. **Transfer $MoS_2$ film:**

Use surface energy assisted technique.
Ensure carrier film is completely dissolved. Do multiple dissolving steps if needed.

9. ***Transfer Pt Contacts on $MoS_2$/ITO/Glass.***

    a. **Transfer Pt contacts:**

Use surface energy assisted technique.
Ensure carrier film is completely dissolved. Do multiple dissolving steps if needed.

# BIBLIOGRAPHY


[1] S. Paul and R. Nath, “CO 2 emission from energy use in India : a decomposition analysis,” vol. 32, pp. 585–593, 2004.

[2] J. Baek, “Do nuclear and renewable energy improve the environment ? Empirical evidence from the United States,” *Ecol. Indic.*, vol. 66, pp. 352–356, 2016.

[3] L. Zhu, K. Emanuel, and S. M. Quiring, “Elevated risk of tropical cyclone precipitation and pluvial flood in Houston under global warming OPEN ACCESS Elevated risk of tropical cyclone precipitation and pluvial flood in Houston under global warming,” 2021.

[4] Y. Yang *et al.*, “Greenhouse warming intensifies north tropical Atlantic climate variability,” pp. 1–11, 2021.

[5] L. Zhu, S. M. Quiring, I. Guneralp, and W. G. Peacock, “Climate Risk Management Variations in tropical cyclone-related discharge in four watersheds near Houston , Texas,” *Clim. Risk Manag.*, vol. 7, pp. 1–10, 2015.

[6] R. Summary, “Photovoltaic materials: Present efficiencies and future challenges.”

[7] J. Li *et al.*, “A Brief Review of High Efficiency III-V Solar Cells for Space Application,” vol. 8, no. February, pp. 1–15, 2021.

[8] W. Shockley and H. J. Queisser, “Detailed Balance Limit of Efficiency of pn Junction Solar Cells,” vol. 510, 1961.

[9] P. Schygulla *et al.*, “Quadruple Junction Solar Cell with 47.6 % Conversion Efficiency under Concentration,” in *International Conference on Metal Organic Vapor Phase Epitaxy 2022*, 2022.

[10] J. F. Geisz *et al.*, “Six-junction III–V solar cells with 47.1% conversion efficiency under 143 Suns concentration,” *Nat. Energy*, vol. 5, no. 4, pp. 326–335, 2020.

[11] R. May and R. May, “On the Atomic Weight o f Graphite. JBy,” 1859.

[12] A. You, M. A. Y. Be, and I. In, “Patterning of highly oriented pyrolytic graphite by oxygen plasma etching,” vol. 193, pp. 10–13, 1999.

[13] K. S. Novoselov *et al.*, “Electric field effect in atomically thin carbon films.,” *Science*, vol. 306, no. 5696, pp. 666–669, Oct. 2004.

[14] N. Mounet *et al.*, “Two-dimensional materials from high-throughput computational exfoliation of experimentally known compounds,” *Nat. Nanotechnol.*, vol. 13, no. March, 2018.

[15] M. Naguib, V. N. Mochalin, M. W. Barsoum, and Y. Gogotsi, “25th anniversary article: MXenes: a new family of two-dimensional materials.,” *Adv. Mater.*, vol. 26, no. 7, pp. 992–1005, Feb. 2014.

[16] M. Ahmad *et al.*, “Transition Metal Carbo-Chalcogenide TMCC A New Family of 2D Materials,” *Adv. Matererials*, vol. 34, no. 26, 2022.

[17] B. Radisavljevic, A. Radenovic, J. Brivio, V. Giacometti, and A. Kis, “Single-layer MoS2 transistors.,” *Nat. Nanotechnol.*, vol. 6, no. 3, pp. 147–150, Mar. 2011.

[18] J. R. Schaibley *et al.*, “Valleytronics in 2D materials,” *Nat. Rev. Mater.*, vol. 1, no. 11, p. 16055, 2016.

[19] G. Scuri *et al.*, “Electrically Tunable Valley Dynamics in Twisted WSe 2 = WSe 2 Bilayers,” vol. 217403, pp. 1–8, 2020.

[20] C. Ataca and S. Ciraci, “Stable, Single-Layer MX2 Transition-Metal Oxides and Dichalcogenides in a Honeycomb-Like Structure,” 2012.

[21] H. Fang, S. Chuang, T. C. Chang, K. Takei, T. Takahashi, and A. Javey, “High-Performance Single Layered WSe 2 p-FETs with Chemically Doped Contacts,” 2012.

[22] W. Liu, J. Kang, D. Sarkar, Y. Khatami, D. Jena, and K. Banerjee, “Role of Metal Contacts in Designing High-Performance Monolayer n - Type WSe 2 Field E ff ect Transistors,” 2013.

[23] D. Braga, I. Gutie, H. Berger, and A. F. Morpurgo, “Quantitative Determination of the Band Gap of WS 2 with Ambipolar Ionic Liquid-Gated Transistors,” 2012.

[24] S. Jo, N. Ubrig, H. Berger, A. B. Kuzmenko, and A. F. Morpurgo, “Mono- and Bilayer WS 2 Light-Emitting Transistors,” 2019.

[25] Y. Xia *et al.*, “Tuning Electrical and Optical Properties of MoSe2 Transistors via Elemental Doping,” no. September, 2020.

[26] S. Aftab, M. F. Khan, P. Gautam, H. Noh, and J. Eom, “MoTe2 van der Waals homojunction p–n diode with low resistance metal contacts,” pp. 9518–9525, 2019.

[27] B. Sirota, N. Glavin, S. Krylyuk, A. V Davydov, and A. A. Voevodin, “Hexagonal MoTe 2 with Amorphous BN Passivation Layer for Improved Oxidation Resistance and Endurance of 2D Field Effect Transistors,” no. January, 2018.

[28] K. Khan *et al.*, *Recent developments in emerging two- dimensional materials and their applications Karim*. Royal Society of Chemistry, 2020.

[29] S. Z. Butler *et al.*, “Opportunities in Two-Dimensional Materials Beyond Graphene,” no. 4, pp. 2898–2926, 2013.

[30] G. R. Bhimanapati *et al.*, “Recent Advances in Two-Dimensional Materials beyond Graphene,” no. 12, pp. 11509–11539, 2015.

[31] S. Das, J. A. Robinson, M. Dubey, H. Terrones, and M. Terrones, “Beyond Graphene: Progress in Novel Two-Dimensional Materials and van der Waals Solids,” *Annu. Rev. Mater. Res.*, vol. 45, no. 1, pp. 1–27, Jul. 2015.

[32] J. A. Wilson and A. D. Yoffe, “The transition metal dichalcogenides discussion and

interpretation of the observed optical, electrical and structural properties," *Adv. Phys.*, vol. 18, no. 73, pp. 193–335, May 1969.

[33] A. V Kolobov and J. Tominaga, "Bulk TMDCs: Review of Structure and Properties BT - Two-Dimensional Transition-Metal Dichalcogenides," A. V Kolobov and J. Tominaga, Eds. Cham: Springer International Publishing, 2016, pp. 29–77.

[34] A. Gulans, A. V Krasheninnikov, and R. M. Nieminen, "van der Waals Bonding in Layered Compounds from Advanced Density-Functional First-Principles Calculations," vol. 235502, no. June, pp. 1–5, 2012.

[35] T. Li and G. Galli, "Electronic Properties of MoS 2 Nanoparticles," vol. 12, pp. 16192–16196, 2007.

[36] K. F. Mak, C. Lee, J. Hone, J. Shan, and T. F. Heinz, "Atomically Thin MoS 2 : A New Direct-Gap Semiconductor," vol. 136805, no. September, pp. 2–5, 2010.

[37] A. Phys, "Optical properties of monolayer transition metal dichalcogenides probed by spectroscopic ellipsometry," vol. 201905, no. November 2014, 2014.

[38] J. D. Kinnison, R. H. Maurer, and T. M. Jordan, "Estimation of the charged particle environment for earth orbits," *Johns Hopkins APL Tech. Dig. (Applied Phys. Lab.*, vol. 11, no. 3–4, pp. 300–310, 1990.

[39] T. Vogl *et al.*, "Radiation tolerance of two-dimensional material- based devices for space applications," *Nat. Commun.*, no. 2019.

[40] A. J. Arnold, T. Shi, I. Jovanovic, and S. Das, "Extraordinary Radiation Hardness of Atomically Thin MoS 2," *ACS Appl. Mater. Interfaces*, vol. 11, no. 8, pp. 8391–8399, 2019.

[41] J. L. Verble, T. J. Wietling, and P. R. Reed, "Rigid-layer lattice vibrations and van der waals bonding in hexagonal MoS2," *Solid State Commun.*, vol. 11, no. 8, pp. 941–944, 1972.

[42] S. H. Mir, V. K. Yadav, and J. K. Singh, "Recent Advances in the Carrier Mobility of Two-Dimensional Materials: A Theoretical Perspective," 2020.

[43] J. H. Gosling *et al.*, "Universal mobility characteristics of graphene originating from charge scattering by ionised impurities," *Commun. Phys.*, vol. 4, no. 1, 2021.

[44] J. H. Kim, T. H. Kim, H. Lee, Y. R. Park, W. Choi, and C. J. Lee, "Thickness-dependent electron mobility of single and few-layer MoS 2 thin-film transistors," vol. 065106, no. May, pp. 2–7, 2016.

[45] J. Robertson, X. Liu, C. Yue, M. Escarra, and J. Wei, "Wafer-scale synthesis of monolayer and few-layer MoS 2 via thermal vapor sulfurization Wafer-scale synthesis of monolayer and few-layer MoS 2 via thermal vapor sulfurization," 2017.

[46] M. Bernardi, M. Palummo, C. Grossman, and R. Scienti, "Extraordinary Sunlight Absorption and One Nanometer Thick Photovoltaics Using Two-Dimensional Monolayer Materials," 2013.

[47] N. Marzari *et al.*, “Large-Area Epitaxial Monolayer MoS 2,” no. 4, pp. 4611–4620, 2015.

[48] T. Li *et al.*, “Epitaxial growth of wafer-scale molybdenum disulfide semiconductor single crystals on sapphire,” *Nat. Nanotechnol.*, vol. 16, no. 11, pp. 1201–1207, 2021.

[49] A. Gurarslan *et al.*, “Surface-Energy-Assisted Perfect Transfer of Centimeter-Scale Films onto Arbitrary Substrates,” no. 11, pp. 11522–11528, 2014.

[50] X. Wang, H. Feng, Y. Wu, and L. Jiao, “Controlled Synthesis of Highly Crystalline MoS 2 Flakes by Chemical Vapor Deposition,” pp. 5–8, 2013.

[51] H. Li *et al.*, “From Bulk to Monolayer MoS 2 : Evolution of Raman Scattering,” no. 1 L, pp. 1385–1390, 2012.

[52] R. Alc, C. Fern, G. Oskam, and J. Idígoras, “Direct Estimation of the Electron Diffusion Length in Dye-Sensitized,” pp. 1045–1050, 2011.

[53] J. A. Anta and J. Bisquert, “Determination of the Electron Diffusion Length in Dye-Sensitized Solar Cells by Random Walk Simulation : Compensation Effects and Voltage Dependence,” pp. 8552–8558, 2010.

[54] J. Park *et al.*, “Diffusion Length in Nanoporous Photoelectrodes of Dye-Sensitized Solar Cells under Operating Conditions Measured by Photocurrent Microscopy,” 2012.

[55] K. M. Islam, R. Synowicki, T. Ismael, I. Oguntoye, N. Grinalds, and M. D. Escarra, “In-Plane and Out-of-Plane Optical Properties of Monolayer , Few-Layer , and Thin-Film MoS2 from 190 to 1700 nm and Their Application in Photonic Device Design,” vol. 2000180, 2021.

[56] X. Li *et al.*, “Role of hydrogen in the chemical vapor deposition growth of MoS2 atomic layers,” *Nanoscale*, vol. 7, no. 18, pp. 8398–8404, 2015.

[57] L. Kang *et al.*, “Epitaxial growth of highly-aligned MoS2 on c-plane sapphire,” *Surf. Sci.*, vol. 720, no. 9, p. 122046, 2022.

[58] M. Sharma, A. Singh, P. Aggarwal, and R. Singh, “Large-Area Transfer of 2D TMDCs Assisted by a Water-Soluble Layer for Potential Device Applications,” *ACS Omega*, vol. 7, no. 14, pp. 11731–11741, 2022.

[59] A. Krayev *et al.*, “Dry Transfer of van der Waals Crystals to Noble Metal Surfaces To Enable Characterization of Buried Interfaces,” *ACS Appl. Mater. Interfaces*, vol. 11, pp. 38218–38225, 2019.

[60] S. M. Shinde, T. Das, A. T. Hoang, B. K. Sharma, and X. Chen, “Surface-Functionalization-Mediated Direct Transfer of Molybdenum Disulfide for Large-Area Flexible Devices,” vol. 1706231, pp. 1–11, 2018.

[61] F. Yu, M. Hu, F. Kang, and R. Lv, “Flexible photodetector based on large-area few-layer MoS2,” *Prog. Nat. Sci. Mater. Int.*, vol. 28, no. 5, pp. 563–568, 2018.

[62] K. M. Islam, T. Ismael, C. Luthy, O. Kizilkaya, and M. D. Escarra, "Large-Area, High-Specific-Power Schottky-Junction Photovoltaics from CVD-Grown Monolayer MoS2," *ACS Appl. Mater. Interfaces*, vol. 14, no. 21, pp. 24281–24289, 2022.

[63] K. Liu *et al.*, "Evolution of interlayer coupling in twisted molybdenum disulfide bilayers," *Nat. Commun.*, vol. 5, pp. 1–6, 2014.

[64] M. Xia *et al.*, "Spectroscopic Signatures of AA' and AB Stacking of Chemical Vapor Deposited Bilayer MoS2," *ACS Nano*, vol. 9, no. 12, pp. 12246–12254, 2015.

[65] C. Yan, X. Dong, C. H. Li, and L. Li, "Charging effect at grain boundaries of MoS2," 2018.

[66] J. Ludwig *et al.*, "Effects of buried grain boundaries in multilayer MoS2," 2019.

[67] H. Xin, J. Zhang, C. Yang, and Y. Chen, "Direct Detection of Inhomogeneity in CVD-Grown 2D TMD Materials via K-Means Clustering Raman Analysis," *Nanomaterials*, vol. 12, no. 3, 2022.

[68] X. Zhang *et al.*, "Shape-Uniform, High-Quality Monolayered MoS 2 Crystals for Gate- Tunable Photoluminescence," 2017.

[69] M. Buscema, M. Barkelid, V. Zwiller, H. S. J. Van Der Zant, G. A. Steele, and A. Castellanos-Gomez, "Large and tunable photothermoelectric effect in single-layer MoS 2," *Nano Lett.*, vol. 13, no. 2, pp. 358–363, 2013.

[70] Y. Zhang *et al.*, "Photothermoelectric and photovoltaic effects both present in MoS2," *Sci. Rep.*, vol. 5, pp. 1–7, 2015.

[71] A. Steinhoff *et al.*, "Efficient Excitonic Photoluminescence in Direct and Indirect Band Gap Monolayer MoS2," *Nano Lett.*, vol. 15, no. 10, pp. 6841–6847, 2015.

[72] S. Sarkar *et al.*, "Direct Bandgap-like Strong Photoluminescence from Twisted Multilayer MoS2Grown on SrTiO3," *ACS Nano*, vol. 14, no. 12, pp. 16761–16769, 2020.

[73] A. Castellanos-Gomez, J. Quereda, H. P. Van Der Meulen, N. Agraït, and G. Rubio-Bollinger, "Spatially resolved optical absorption spectroscopy of single- and few-layer MoS2 by hyperspectral imaging," *Nanotechnology*, vol. 27, no. 11, 2016.

[74] A. Splendiani *et al.*, "Emerging photoluminescence in monolayer MoS2," *Nano Lett.*, vol. 10, no. 4, pp. 1271–1275, 2010.

[75] Q. Ji *et al.*, "Epitaxial monolayer MoS2 on mica with novel photoluminescence," *Nano Lett.*, vol. 13, no. 8, pp. 3870–3877, 2013.

[76] Q. Wang *et al.*, "Layer-by-layer epitaxy of multi-layer MoS2wafers," *Natl. Sci. Rev.*, vol. 9, no. 6, 2022.

[77] J. H. Hur, J. Park, and S. Jeon, "A theoretical modeling of photocurrent generation and decay in layered MoS2 thin-film transistor photosensors," *J. Phys. D. Appl. Phys.*, vol. 50, no. 6, 2017.

[78] H. S. Lee *et al.*, “MoS2 nanosheet phototransistors with thickness-modulated optical energy gap,” *Nano Lett.*, vol. 12, no. 7, pp. 3695–3700, 2012.

[79] J. Jeon *et al.*, “Layer-controlled CVD growth of large-area two-dimensional MoS2 films,” *Nanoscale*, vol. 7, no. 5, pp. 1688–1695, 2015.

[80] A. Singh, M. Sharma, and R. Singh, “NaCl-Assisted CVD Growth of Large-Area High-Quality Trilayer MoS2and the Role of the Concentration Boundary Layer,” *Cryst. Growth Des.*, vol. 21, no. 9, pp. 4940–4946, 2021.

[81] T. J. Dai *et al.*, “Layer-controlled synthesis of wafer-scale MoSe2 nanosheets for photodetector arrays,” *J. Mater. Sci.*, vol. 53, no. 11, pp. 8436–8444, 2018.

[82] N. Choudhary, J. Park, J. Y. Hwang, and W. Choi, “Growth of Large-Scale and Thickness-Modulated MoS 2 Nanosheets,” 2014.

[83] A. Singh, M. Moun, and R. Singh, “Effect of different precursors on CVD growth of molybdenum disulfide,” *J. Alloys Compd.*, vol. 782, pp. 772–779, 2019.

[84] Y. Zhang *et al.*, “Scaling law for strain dependence of Raman spectra in transition-metal dichalcogenides,” *J. Raman Spectrosc.*, vol. 51, no. 8, pp. 1353–1361, 2020.

[85] Y. Niu *et al.*, “Thickness-dependent differential reflectance spectra of monolayer and few-layer MoS2, MoSe2, WS2 and WSe2,” *Nanomaterials*, vol. 8, no. 9, 2018.

[86] R. Frisenda *et al.*, “Micro-reflectance and transmittance spectroscopy: A versatile and powerful tool to characterize 2D materials,” *J. Phys. D. Appl. Phys.*, vol. 50, no. 7, 2017.

[87] X. Wang and B. Chen, “Origin of Fresnel problem of two dimensional materials,” *Sci. Rep.*, vol. 9, no. 1, pp. 1–8, 2019.

[88] Y. Li *et al.*, “Measurement of the optical dielectric function of monolayer transition-metal dichalcogenides: MoS2, Mo S e2, WS2, and WS e2,” *Phys. Rev. B - Condens. Matter Mater. Phys.*, vol. 90, no. 20, pp. 1–6, 2014.

[89] A. K. Sharma, R. Kumar, P. K. Jha, M. Kumar, N. K. Chourasia, and R. K. Chourasia, “Bulk Parameters Effect and Comparative Performance Analysis of p-Si/n-CdS/ALD-ZnO Solar Cell,” *Silicon*, no. 0123456789, 2023.

[90] A. Richter, M. Hermle, and S. W. Glunz, “Reassessment of the limiting efficiency for crystalline silicon solar cells,” *IEEE J. Photovoltaics*, vol. 3, no. 4, pp. 1184–1191, 2013.

[91] W. Shockley and H. Queisser, “Detailed balance limit of efficiency of p-n junction solar cells,” *Renewable Energy: Four Volume Set*, vol. 2–4. pp. 35–54, 2018.

[92] P. A. Iles, “Future of photovoltaics for space applications,” *Prog. PHOTOVOLTAICS Res. Appl.*, vol. 8, no. 2000, pp. 39–51, 2000.

[93] M. Yamaguchi, S. J. Taylor, S. Matsuda, and O. Kawasaki, “Mechanism for the anomalous degradation of Si solar cells induced by high fluence 1 MeV electron irradiation,” *Appl. Phys. Lett.*, vol. 3143, no. July 2016, p. 3141, 1995.

[94] M. Yamaguchi, A. Khan, S. J. Taylor, M. Imaizumi, T. Hisamatsu, and S. Matsuda, “A detailed model to improve the radiation-resistance of si space solar cells,” *IEEE Trans. Electron Devices*, vol. 46, no. 10, pp. 2133–2138, 1999.

[95] I. Massiot, A. Cattoni, and S. Collin, “Progress and prospects for ultrathin solar cells,” *Nat. Energy*, vol. 5, no. 12, pp. 959–972, 2020.

[96] M. A. Green *et al.*, “Solar cell efficiency tables (Version 61),” *Prog. Photovoltaics Res. Appl.*, vol. 31, no. 1, pp. 3–16, 2023.

[97] M. Nakamura, K. Yamaguchi, Y. Kimoto, Y. Yasaki, T. Kato, and H. Sugimoto, “Cd-Free Cu(In,Ga)(Se,S)2 thin-film solar cell with record efficiency of 23.35%,” *IEEE J. Photovoltaics*, vol. 9, no. 6, pp. 1863–1867, 2019.

[98] C. Chen *et al.*, “Perovskite solar cells based on screen-printed thin films,” *Nature*, vol. 612, no. 7939, pp. 266–271, 2022.

[99] H. Min *et al.*, “Perovskite solar cells with atomically coherent interlayers on SnO2 electrodes,” *Nature*, vol. 598, no. 7881, pp. 444–450, 2021.

[100] X. Jiang, Z. Zang, Y. Zhou, H. Li, Q. Wei, and Z. Ning, “Tin Halide Perovskite Solar Cells: An Emerging Thin-Film Photovoltaic Technology,” *Accounts Mater. Res.*, vol. 2, no. 4, pp. 210–219, 2021.

[101] Y. Yang *et al.*, “A thermotropic liquid crystal enables efficient and stable perovskite solar modules,” *Nat. Energy*, vol. 9, no. 3, pp. 316–323, 2024.

[102] Z. Huan *et al.*, “Advancements in radiation resistance and reinforcement strategies of perovskite solar cells in space applications,” *J. Mater. Chem. A*, vol. 12, no. 4, pp. 1910–1922, 2024.

[103] S. Roy and P. Bermel, “Tungsten-Disulfide-Based Ultrathin Solar Cells for Space Applications,” *IEEE J. Photovoltaics*, vol. 12, no. 5, pp. 1184–1191, 2022.

[104] D. Jariwala, A. R. Davoyan, J. Wong, and H. A. Atwater, “Van der Waals Materials for Atomically-Thin Photovoltaics: Promise and Outlook,” *ACS Photonics*, vol. 4, no. 12, pp. 2962–2970, 2017.

[105] K. P. Dhakal *et al.*, “Confocal absorption spectral imaging of MoS2: Optical transitions depending on the atomic thickness of intrinsic and chemically doped MoS2,” *Nanoscale*, vol. 6, no. 21, pp. 13028–13035, 2014.

[106] L. Huang *et al.*, “Atomically Thin MoS2 Narrowband and Broadband Light Superabsorbers,” *ACS Nano*, vol. 10, no. 8, pp. 7493–7499, 2016.

[107] Z. Hu, D. Lin, J. Lynch, K. Xu, and D. Jariwala, “How good can 2D excitonic solar cells be?,” *Device*, vol. 1, no. 1, p. 100003, 2023.

[108] L. Wang *et al.*, “2D Photovoltaic Devices: Progress and Prospects,” *Small Methods*, vol. 2, no. 3, pp. 1–20, 2018.

[109] G. Casillas, U. Santiago, H. BarroÌn, D. Alducin, A. Ponce, and M. José-Yacamán, “Elasticity of MoS2 sheets by mechanical deformation observed by in situ electron

microscopy," *J. Phys. Chem. C*, vol. 119, no. 1, pp. 710–715, 2015.

[110] T. Vogl *et al.*, "Radiation tolerance of two-dimensional material-based devices for space applications," *Nat. Commun.*, vol. 10, no. 1, 2019.

[111] H. M. Li *et al.*, "Ultimate thin vertical p-n junction composed of two-dimensional layered molybdenum disulfide," *Nat. Commun.*, vol. 6, pp. 1–9, 2015.

[112] C. M. Went *et al.*, "A new metal transfer process for van der Waals contacts to vertical Schottky-junction transition metal dichalcogenide photovoltaics," *Sci. Adv.*, vol. 5, no. 12, 2019.

[113] E. McVay, A. Zubair, Y. Lin, A. Nourbakhsh, and T. Palacios, "Impact of Al2O3Passivation on the Photovoltaic Performance of Vertical WSe2Schottky Junction Solar Cells," *ACS Appl. Mater. Interfaces*, vol. 12, no. 52, pp. 57987–57995, 2020.

[114] S. A. Svatek *et al.*, "High open-circuit voltage in transition metal dichalcogenide solar cells," *Nano Energy*, vol. 79, 2021.

[115] A. Abnavi *et al.*, "Flexible High-Performance Photovoltaic Devices based on 2D MoS2 Diodes with Geometrically Asymmetric Contact Areas," *Adv. Funct. Mater.*, vol. 33, no. 7, pp. 1–13, 2023.

[116] T. Akama, W. Okita, R. Nagai, C. Li, T. Kaneko, and T. Kato, "Schottky solar cell using few-layered transition metal dichalcogenides toward large-scale fabrication of semitransparent and flexible power generator," *Sci. Rep.*, vol. 7, no. 1, pp. 1–10, 2017.

[117] K. Nassiri Nazif *et al.*, "High-specific-power flexible transition metal dichalcogenide solar cells," *Nat. Commun.*, vol. 12, no. 1, pp. 1–9, 2021.

[118] J. A. Carr *et al.*, "The Lightweight Integrated Solar Array and anTenna: 3rd Generation Advancements, and Beyond," 2017.

[119] H. Zhu *et al.*, "Design investigation on 100 μm-thickness thin silicon PERC solar cells with assistance of machine learning," *Materials Science in Semiconductor Processing*, vol. 137. 2022.

[120] Maxeon Solar Technologies, "Performance 6 solar panel SPR-P6-400-COM-XS," 2023. [Online]. Available: https://sunpower.maxeon.com/au/sites/default/files/2023-04/sp_mst_p6_com_xs_1092_1.8m_.6m_cable_ds_en_a4_evo2_548188.pdf.

[121] B. Peng, P. K. Ang, and K. P. Loh, "Two-dimensional dichalcogenides for light-harvesting applications," *Nano Today*, vol. 10, no. 2, pp. 128–137, 2015.

[122] K. Nassiri Nazif *et al.*, "High-Performance p-n Junction Transition Metal Dichalcogenide Photovoltaic Cells Enabled by MoOxDoping and Passivation," *Nano Lett.*, vol. 21, no. 8, pp. 3443–3450, 2021.

[123] A. T. Nguyen *et al.*, "High-Performance and Lithography-Free Au/WS2/Ag Vertical

Schottky Junction Solar Cells," *Adv. Mater. Interfaces*, vol. 10, no. 15, pp. 1–7, 2023.

[124] NeXolve, "CP1 ™ Polyimide Characteristics Typical Properties of CP1 ™ Polyimide," 2022.

[125] M. C. Troparevsky, A. S. Sabau, A. R. Lupini, and Z. Zhang, "Transfer-matrix formalism for the calculation of optical response in multilayer systems: from coherent to incoherent interference," *Opt. Express*, vol. 18, no. 24, p. 24715, 2010.

[126] T. Ismael, N. J. Grinalds, M. A. Abbas, N. Hill, C. E. Luthy, and M. D. Escarra, "Correlative Spatial Mapping of Optoelectronic Properties in Large Area 2D MoS2 Phototransistors," *Adv. Mater. Interfaces*, vol. 2300455, 2023.

[127] A. Chirilă *et al.*, "Potassium-induced surface modification of Cu(In,Ga)Se2 thin films for high-efficiency solar cells," *Nat. Mater.*, vol. 12, no. 12, pp. 1107–1111, 2013.

[128] J. Kim, J. Hwang, K. Song, N. Kim, J. C. Shin, and J. Lee, "Ultra-thin flexible GaAs photovoltaics in vertical forms printed on metal surfaces without interlayer adhesives," *Appl. Phys. Lett.*, vol. 108, no. 25, 2016.

[129] T. Söderström, F. J. Haug, V. Terrazzoni-Daudrix, and C. Ballif, "Optimization of amorphous silicon thin film solar cells for flexible photovoltaics," *J. Appl. Phys.*, vol. 103, no. 11, 2008.

[130] M. Kaltenbrunner *et al.*, "Ultrathin and lightweight organic solar cells with high flexibility," *Nat. Commun.*, vol. 3, 2012.

[131] Y. Liu *et al.*, "Approaching the Schottky–Mott limit in van der Waals metal–semiconductor junctions," *Nature*, vol. 557, no. 7707, pp. 696–700, 2018.

[132] Z. Yang *et al.*, "A Fermi-Level-Pinning-Free 1D Electrical Contact at the Intrinsic 2D MoS2–Metal Junction," *Adv. Mater.*, vol. 31, no. 25, pp. 1–9, 2019.

[133] L. Wang and J. B. Sambur, "Efficient Ultrathin Liquid Junction Photovoltaics Based on Transition Metal Dichalcogenides," *Nano Lett.*, vol. 19, no. 5, pp. 2960–2967, 2019.

[134] M. Shanmugam, C. A. Durcan, and B. Yu, "Layered semiconductor molybdenum disulfide nanomembrane based Schottky-barrier solar cells," *Nanoscale*, vol. 4, no. 23, pp. 7399–7405, 2012.

[135] J. Lewis, "Material challenge for flexible organic devices," *Mater. Today*, vol. 9, no. 4, pp. 38–45, 2006.

[136] S. R. Messenger, J. H. Warner, R. Uribe, and R. J. Walters, "Monte Carlo analyses of the NEO beam electron beam facility for space solar cell radiation qualification," *IEEE Trans. Nucl. Sci.*, vol. 57, no. 6 PART 1, pp. 3470–3476, 2010.

[137] R. M. Uribe, "A new electron accelerator facility for commercial and educational uses," vol. 775, no. September 2001, pp. 775–778, 2003.

[138] D. M. Sawyer and J. I. Vette, “AP-8 trapped proton environment for solar maximum and solar minimum,” *NASA STIRecon Tech. Rep. N*, vol. 77, pp. 18983-+, 1976.

[139] S. R. Messenger *et al.*, “Status of implementation of displacement damage dose method for space solar cell degradation analyses,” *Eur. Sp. Agency, (Special Publ. ESA SP*, no. 661 SP, 2008.

[140] E. Kulu, “Nanosatellite & CubeSat Database,” *Nanosatellite & CubeSat Database*, 2024. [Online]. Available: https://www.nanosats.eu/. [Accessed: 05-Apr-2024].

[141] E. Kulu, “Nanosatellite Launch Forecasts - Track Record and Latest Prediction,” *36th Annu. Small Satell. Conf.*, 2022.

[142] M. K. Chamberlain, S. H. Kiefer, and J. A. Banik, “Structural analysis methods for the roll-out solar array flight experiment,” *AIAA Scitech 2019 Forum*, pp. 1–15, 2019.

[143] A. J. Lee and J. M. Fernandez, “Mechanics of bistable two-shelled composite booms,” *AIAA Spacecr. Struct. Conf. 2018*, pp. 1–24, 2018.

[144] L. Johnson, R. Young, E. Montgomery, and D. Alhorn, “Status of solar sail technology within NASA,” *Adv. Sp. Res.*, vol. 48, no. 11, pp. 1687–1694, 2011.

[145] C. Ynchausti, C. Roubicek, J. Erickson, B. Sargent, S. P. Magleby, and L. L. Howell, “Hexagonal Twist Origami Pattern for Deployable Space Arrays,” *ASME Open J. Eng.*, vol. 1, pp. 1–10, 2022.

[146] D. Bolanos *et al.*, “Considering thickness-accommodation, nesting, grounding and deployment in design of Miura-ori based space arrays,” *Mech. Mach. Theory*, vol. 174, no. March, p. 104904, 2022.

[147] J. A. Carr *et al.*, “LISA-T part three: The design and space environments testing of a thin-film power generation and communication array,” *Acta Astronaut.*, vol. 205, no. February, pp. 267–280, 2023.

[148] D. J. Moorhouse, “Detailed Definitions and Guidance for Application of Technology Readiness Levels,” *J. Aircr.*, vol. 39, pp. 190–192, 2002.

[149] D. M. Bacal *et al.*, “Solution-processed antireflective coating for back-contact perovskite solar cells,” *Opt. Express*, vol. 28, no. 9, p. 12650, 2020.

[150] K. M. Islam, T. Ismael, C. Luthy, O. Kizilkaya, and M. D. Escarra, “Large-Area, High-Specific Power Schottky-Junction Photovoltaics from CVD-Grown Monolayer MoS2,” no. Cvd, 2022.

[151] H. W. Jones, “The Recent Large Reduction in Space Launch Cost,” *48th Int. Conf. Environ. Syst.*, no. July 2018, p. 81, 2018.

[152] M. Woodhouse *et al.*, “Research and Development Priorities to Advance Solar Photovoltaic Lifecycle Costs and Performance,” *Natl. Renew. Energy Lab.*, vol. 1, no. 10, pp. 1–52, 2021.

[153] A. Klein *et al.*, “Transparent conducting oxides for photovoltaics: Manipulation of

fermi level,work function and energy band alignment," *Materials (Basel).*, vol. 3, no. 11, pp. 4892–4914, 2010.

[154] M. K. Kavitha and M. Jaiswal, "Graphene: A review of optical properties and photonic applications," *Asian J. Phys.*, vol. 25, no. 7, pp. 809–831, 2016.

[155] J. Wong *et al.*, "High Photovoltaic Quantum Efficiency in Ultrathin van der Waals Heterostructures," *ACS Nano*, vol. 11, no. 7, pp. 7230–7240, 2017.

[156] J. Zhang *et al.*, "Deep UV transparent conductive oxide thin films realized through degenerately doped wide-bandgap gallium oxide," *Cell Reports Phys. Sci.*, vol. 3, no. 3, p. 100801, 2022.

[157] R. Dagan, Y. Vaknin, A. Henning, J. Y. Shang, L. J. Lauhon, and Y. Rosenwaks, "Two-dimensional charge carrier distribution in MoS2 monolayer and multilayers," *Appl. Phys. Lett.*, vol. 114, no. 10, 2019.

[158] A. Kumar and P. K. Ahluwalia, "Tunable dielectric response of transition metals dichalcogenides MX 2 (M=Mo, W; X=S, Se, Te): Effect of quantum confinement," *Phys. B Condens. Matter*, vol. 407, no. 24, pp. 4627–4634, 2012.

[159] E. S. Kadantsev and P. Hawrylak, "Electronic structure of a single MoS 2 monolayer," *Solid State Commun.*, vol. 152, no. 10, pp. 909–913, 2012.

[160] Z. Chu *et al.*, "Unveiling defect-mediated carrier dynamics in monolayer semiconductors by spatiotemporal microwave imaging," *Proc. Natl. Acad. Sci. U. S. A.*, vol. 117, no. 25, pp. 13908–13913, 2020.

[161] N. Huo, Y. Yang, Y.-N. Wu, X.-G. Zhang, S. T. Pantelides, and G. Konstantatos, "High carrier mobility in monolayer CVD-grown MoS2 through phonon suppression," *Nanoscale*, vol. 10, no. 31, pp. 15071–15077, 2018.

[162] S. Srivastava and Y. N. Mohapatra, "Determination of interlayer electron mobility in multilayer MoS2flake using impedance spectroscopy," *J. Phys. D. Appl. Phys.*, vol. 54, no. 29, 2021.

[163] V. Ramasamy, D. Feldman, J. Desai, and R. Margolis, "U.S. Solar Photovoltaic System and Energy Storage Cost Benchmark: Q1 2021," *Natl. Renew. Energy Lab.*, no. September, pp. 1–120, 2021.

# BIOGRAPHY

Timothy Ismael received his AA in Electrical Engineering Technology from the Dominica State College in 2007, then received his certificate of Aeronautical Information Service in 2007 and certificate in Air Traffic Control in 2009 from the Barbados Civil Aviation Training Center. He obtained research experience in Physics and received his BSc in Mathematics & Physics and Engineering Technology at Grambling State University in 2016. He then attended Louisiana Tech University where he received his MSc in Applied Physics. He joined the Department of Physics and Engineering Physics at Tulane University in 2018 where he joined the Escarra Research Group and worked on synthesis of two-dimensional materials and development devices 2D material-based devices for various applications with Dr. Matthew D. Escarra as his mentor. In his spare time, he plays the guitar and enjoys drawing and painting.